Aus dem Pharmakologischen Institut
Direktor: Prof. Dr. Thomas Worzfeld
des Fachbereichs Medizin der Philipps-Universität Marburg

α-Actinin regulates nuclear actin bundling and nuclear size in early G1

Inaugural-Dissertation
zur Erlangung des Doktorgrades der Naturwissenschaften (Dr. rer. nat.)

dem Fachbereich Medizin der Philipps-Universität Marburg
vorgelegt von

Sylvia Krippner
aus Kyritz

Marburg, 2020

Angenommen am Fachbereich Medizin der Philipps-Universität Marburg
am: 31.03.2020

Gedruckt mit Genehmigung des Fachbereichs.

Dekan: Herr Prof. Dr. Helmut Schäfer
Referent: Herr Prof. Dr. Robert Grosse
Korreferent: Herr Prof. Dr. Sven Bogdan

Meiner Familie.

Table of Contents

List of Figures

List of Tables

Abbreviations

ABBREVIATION	EXPLANATION
aa	Amino acid
ABD	Actin-binding domain
ACTN1 / ACTN4	Alpha actinin / α-actinin; non-muscle isoform 1 / 4
ADP	Adenosine diphosphate
AF555 / AF 647	AlexaFluor, fluorophore that is coupled to proteins (excitation at 555 nm / 647 nm)
Arp	Actin-related protein
ATP	Adenosine triphosphate
ATPase	ATP hydrolase
ca	Constitutively active
CaM	Calmodulin-like domain
C_C	Critical concentration
CDK1	Cyclin-dependent kinase 1
CH domain	Calponin homology domain
cMTP	Congenital macrothrombocytopenia
COBL	Protein cordon-bleu
CRM-1	Chromosomal maintenance 1 = Exportin 1
CSK	Cytoskeleton buffer
dn	Dominant negative
DNA	Deoxyribonucleic acid

ABBREVIATION	EXPLANATION
DSB	Double strand break
dSTORM	Direct stochastic optical reconstruction microscopy
EF	EF-hand,
EGF	Epithelial growth factor
ER	Estrogen receptor
ERM	Ezrin, Radixin, Moesin (membrane proteins)
FA	Formaldehyde
F-actin	Filamentous, fibrous actin
FSGS	Focal segmental glomerulosclerosis
G1	Gap phase 1, growth phase
G-actin	Globular actin
GFP	Green-fluorescent protein
GR	Glucocorticoid receptor
HDAC	Histone deacetylase
INF2	Inverted formin 2
JMY	Junction-mediating and -regulatory protein
LPA	Lysophosphatidic acid
mCh	Fluorescent protein mCherry (red, excitation at 555 nm)
mDia2	Protein diaphanous homolog 2
mRNA	Messenger ribonucleic acid
nAC	Nuclear actin chromobody
NEBD	Nuclear envelope breakdown

ABBREVIATION	EXPLANATION
NES	Nuclear export signal
NLS	Nuclear localization signal
NPC	Nuclear pore complex
o/n	Overnight
p53	Cellular tumor antigen p53
RNAi	RNS interference
ROS	Reactive oxygen species
RT	Room temperature
SD	Standard deviation
SEM	Standard error of mean
siR	Resistance towards siRNA treatment
siRNA	Small interfering RNA
SMLM	Single-Molecule Localization Microscopy
SR	Spectrin repeat
SRF	Serum response factor
TNF	Tumor necrosis factor

1. Introduction

1.1 DNA and cell cycle

1.1.1 Genome organization during the cell cycle

Human cells contain vast amounts of DNA; approximately 3.2 x 10^9 nucleotides distributed over 24 chromosomes (including sex chromosomes) [5]. This is equivalent to a continuous DNA-strand of about 2 m length in a single cell, requiring efficient packaging and organization within the nuclear compartment.

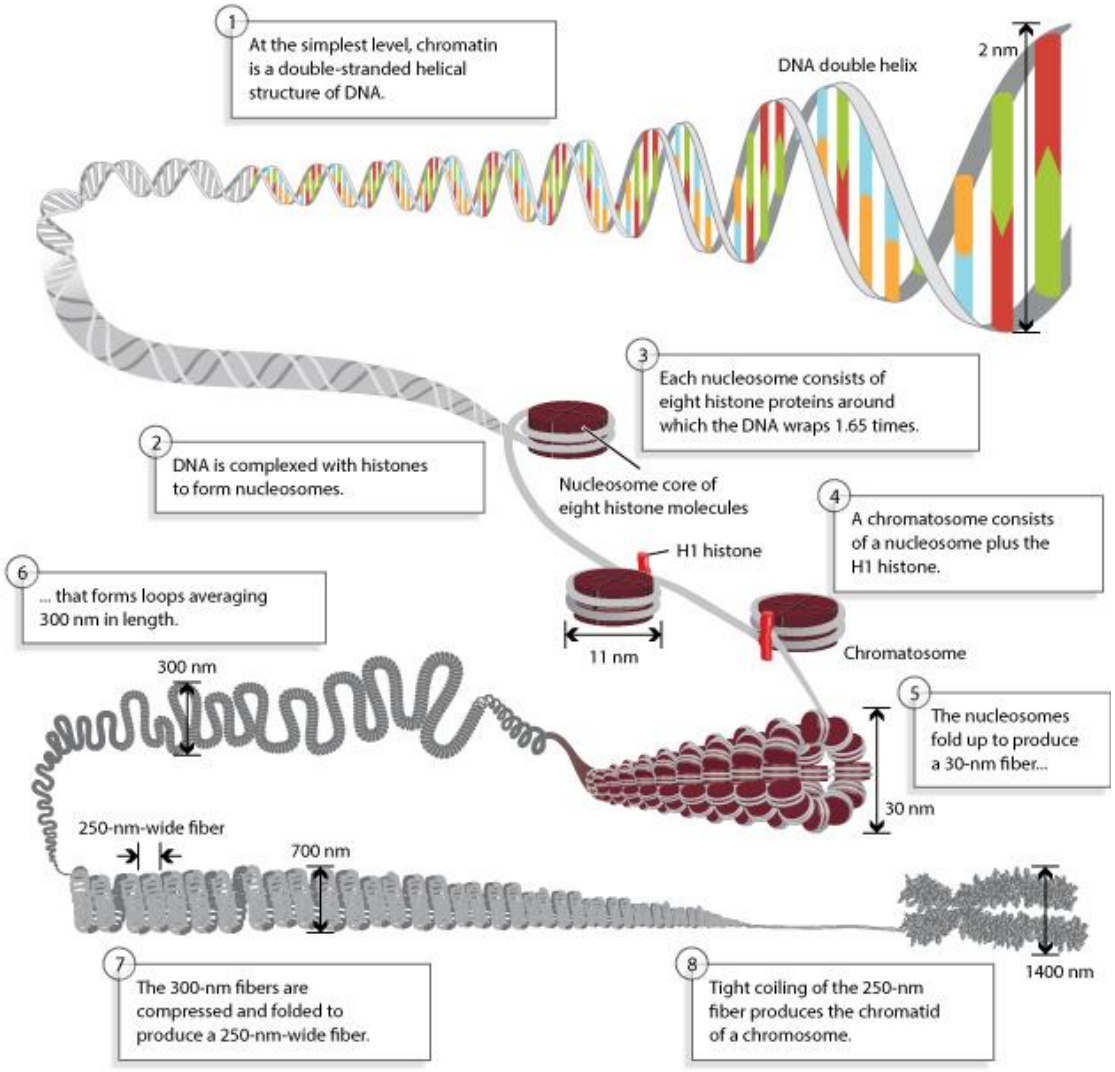

Figure 1. Packaging of DNA into higher order structures.

Single steps are indicated in the picture and in the text. Adapted from [135] © 2013 Nature Education.

The double-stranded DNA helix holds a negative net charge due to the phosphate groups in its backbone. Therefore, DNA tightly binds the positively charged core histones H2A, H2B, H3, H4 (Fig 1.1-4) [199]. The complex of DNA around core histones is called a nucleosome, whereas the more general association of DNA and interacting proteins refers to as chromatin (Fig 1.5) [5]. Chromatin can be present in two different major conformations: Heterochromatin displaying a condensed and euchromatin a decondensed state [171]. Further, chromatin forms loop structures and individual chromosomes compress to hypercondensed states during cell division referred to as chromatid (Fig 1.6-7).

1.1.2 Cell cycle and mitosis

The cell cycle and especially the M-phase are complex and highly dynamic processes which depend on a series of cytoskeletal changes and rearrangements (Fig 2).

Throughout all stages of the cell cycle, cyclin-dependent kinases (CDKs) and their allosteric regulation by cyclins play important roles for initiation of individual phases (Fig 2) or for control mechanisms such as cell cycle checkpoints. They form regulatory complexes with cyclins and other proteins such as tumor suppressor p53 [154]. In G1, postmitotic cells enter a growth phase until starting DNA replication in consecutive S phase. In case of incomplete replication or damaged DNA, a major checkpoint arrests cells in G2 phase, initiates repair mechanisms or prohibits cell cycle progression to maintain genomic integrity [39, 165]. However, intact cells enter mitosis starting at prophase when both centrosomes move along the nucleus to the spindle poles. Nuclear envelope breakdown (NEBD) occurs in prometaphase, before the mitotic spindle captures chromosomes at kinetochores upon progression to metaphase [4]. Phosphorylation of histone H3 and subsequent deacetylation of histone H4 enable surface interactions of neighboring nucleosomes and are therefore involved in chromatin hypercondensation [193]. After aligning at the metaphase plate, sister chromatids start to segregate and move towards the spindle poles in anaphase [4]. Additionally, a contractile actomyosin ring assembles upon RhoA and formin activation in an equatorial plane to enable contraction and abscission [119, 163]. Actin cross-linking proteins stabilize the ring and cleavage furrow; e.g. ACTN and fimbrin were found to cooperate with myosin II in fission yeast [109].

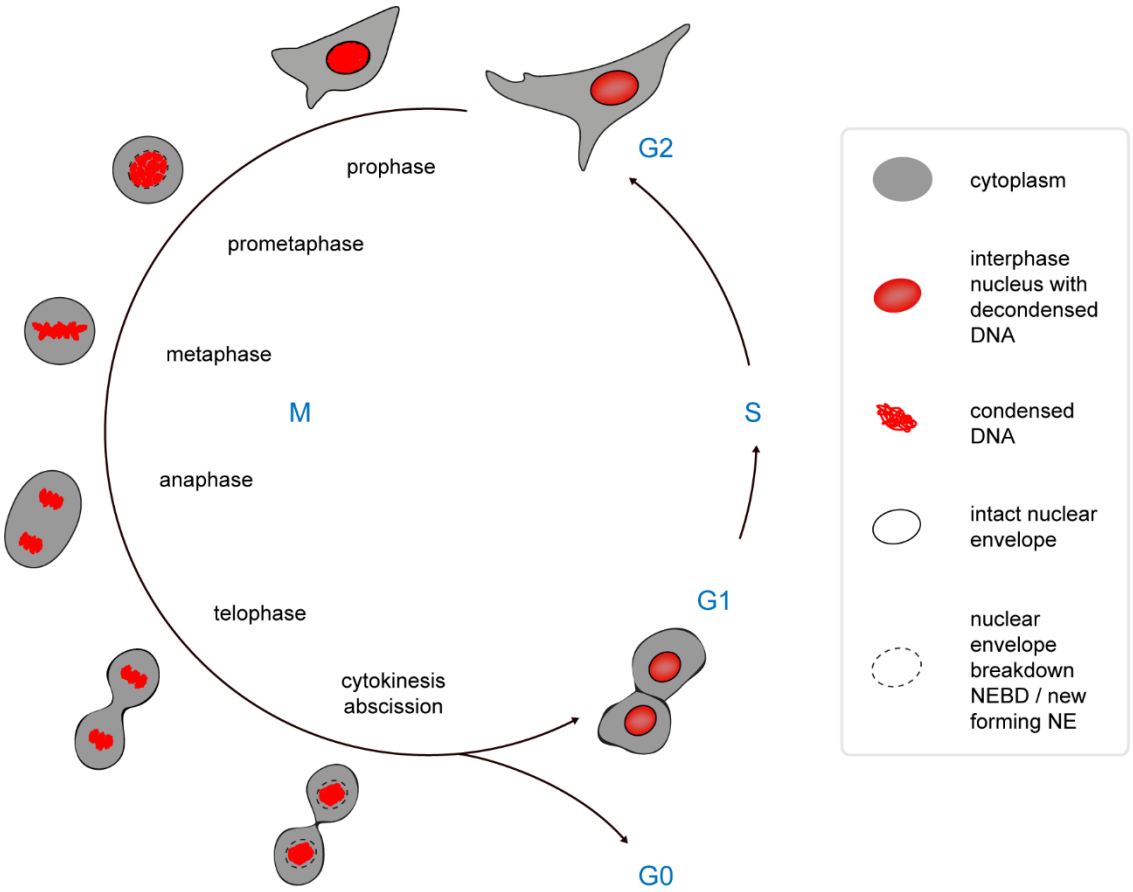

Figure 2. Cell cycle in mammalian cells.

The cell cycle consists of different stages: G0 = quiescence, G1 = gap 1, S = synthesis phase, G2 = gap 2, M = Mitosis with prophase, prometaphase, metaphase, anaphase, telophase, cytokinesis and abscission. Single steps are described in the text.

Telophase encompasses the formation of new nuclear envelopes around the separated sister chromatids [4]. Nuclear pore complexes (NPCs) are integrated [157] and chromatin condensation is driven by inactivation of mitotic kinases and further involvement of RuvBL1 and RuvBL2 [168].

The final abscission generates two identical daughter cells which can either enter the quiescent G0 phase or start a new cell cycle (G1) [173]. Rearrangement of nuclear structure within the newly formed nuclear envelopes also includes nuclear volume expansion in early G1 [130], which was recently proposed to be dependent on postmitotic actin filament formation [12]. Different factors influence the size of the nuclear compartment, e.g. DNA content, nuclear import or the nucleocytoplasmic scaling

mechanism, ensuring concomitant size regulation between nucleus and overall cell size [104].

Alterations in nuclear size and shape can indicate ageing as well as premature ageing syndromes or can be found upon viral infections and cancer [108, 154, 190].

1.2 The actin cytoskeleton

1.2.1 Distinct structures of actin and their regulation

Back in the early 1940's, actin was first characterized and found to form the basic element for muscle contraction together with myosin [8, 86, 87, 167]. The two cytoplasmic isoforms β- and γ-actin co-exist ubiquitously in every eukaryotic cell – except in nematode sperm – and form dynamic microfilaments or regulate other cellular functions [33, 71, 146].

Actin is present in two conformations: The monomeric globular G-actin – which measures 5 nm in diameter – consists of 375 amino acids, resulting in a 42 kDa protein [77, 90]. G-actin monomers form stable complexes (nuclei) in the initial nucleation phase (Fig 3 A). Subunits are added to either side of the nucleus and the filament elongates given that the G-actin concentration in solution exceeds the critical concentration C_c (Fig 3 B) [113].

In filamentous F-actin, every subunit is adjacent to four others inside the filament, forming a double stranded right-handed helix with 5-7 nm diameter and 166° rotation [65, 77, 90]. Actin filaments are polar structures [18] characterized by different critical concentrations C_c, thus different association and dissociation rates for the (+) barbed end (lower C_c, faster growth) contrary to the (-) pointed end (higher C_c, slower growth) [140]. Given that G-actin concentrations are intermediate between both critical concentrations, equal amounts of monomers are added to the (+) and subtracted from the (-) end, resulting in a steady state condition, so called actin treadmilling (Fig 3 C) [113].

Actin treadmilling is a special property of actin to suppress spontaneous polymerization: Under steady state conditions, subunits fluctuate along the filaments comparable to moving on a treadmill [99].

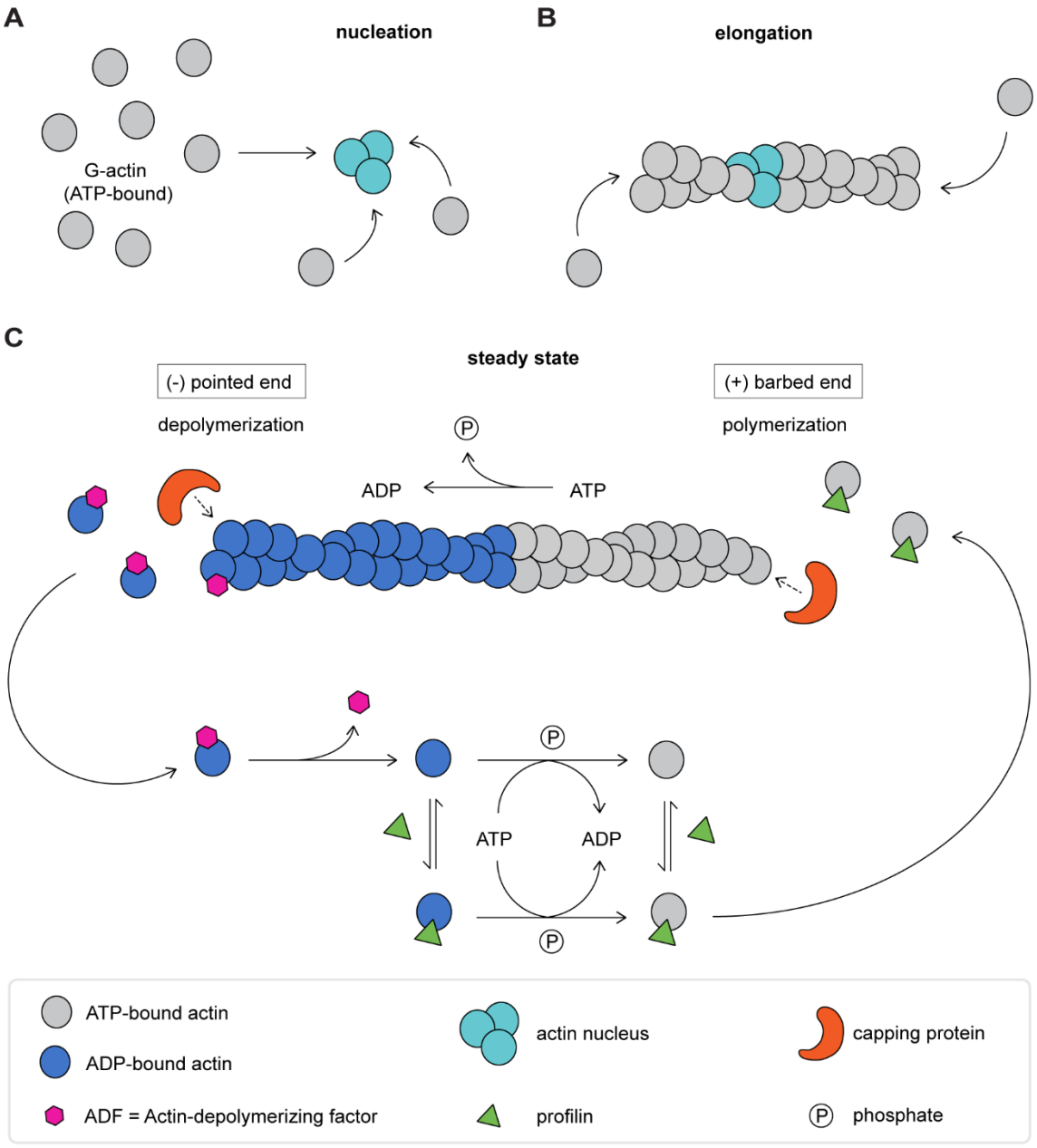

Figure 3. Nucleation, elongation and treadmilling of actin filaments.

(A) Actin nucleus is formed of G-actin. (B) Actin monomers are added to both sides of the nucleus to form and elongate the filament. (C) Actin treadmilling under steady state conditions; steps are indicated in the main text.

Assembly and disassembly of actin filaments are influenced by redox reaction mechanisms based on the reduction-oxidation-enzyme Mical [1, 85], but mainly rely on ATP hydrolysis in a G-actin cleft [64]. Hydrolysis of ATP at the pointed end is dependent on bound divalent cations such as Mg^{2+} or Ca^{2+} [24] and leads to conformational changes in monomers and structural integrity of filaments [99].

Profilin promotes actin assembly, while thymosin β_4 is an inhibiting factor. Actin-depolymerizing factors (severing proteins) such as cofilin or gelsolin control the length of a filament and sever it into shorter fragments in order to enable dynamic turnover (Fig 4) [61, 101, 113]. In sarcomeres and other structures that do not require rapid turnover, actin filaments are stabilized by proteins such as CapZ which caps the (+) end or tropomodulin which caps the (-) end (Fig 3) [113]. Importantly, actin filaments can be bundled and crosslinked providing mechanical stability (cf 1.3.3, Fig 4) [141].

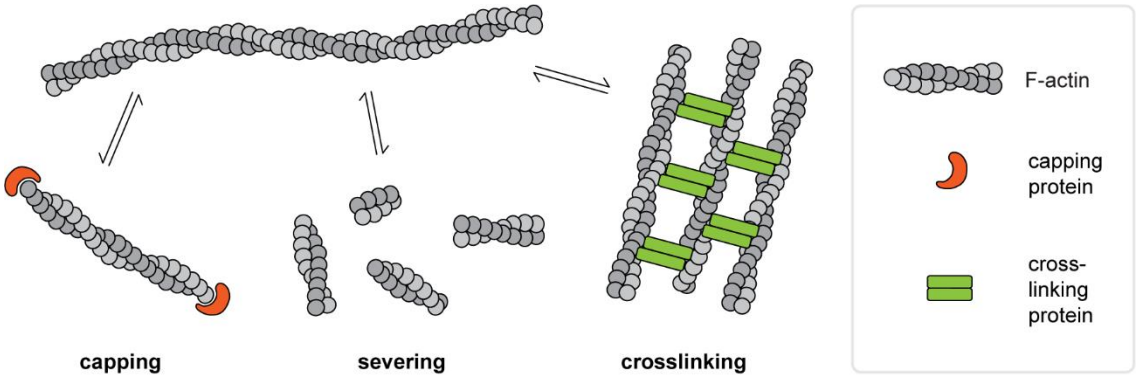

Figure 4. Modifications of actin filaments: capping, severing & crosslinking.
Actin filaments are modified by several classes of actin-binding proteins. Capping proteins can cover the (+) and (-) ends of the filament; severing proteins disassemble F-actin; actin crosslinking proteins connect and bundle filaments to obtain different functions. Modified after [141].

1.2.2 Functions of actin

The scaffolding function of actin structures in the cytoplasm is known for decades [69], but beyond that, actin is involved in various cellular processes: morphogenesis & shape, adhesion, motility, transport, cytokinesis and signaling.

Polymerized actin provides cell and tissue morphogenesis and shape [66]. Furthermore, it was found in membrane protrusions such as lamellipodia, ruffles, filopodia and microvilli [36, 110], thus plays key roles in various cellular processes [35, 66, 67], signaling and communication [42]. Contractile stress fibers are generated by actin assembly and bundling mechanisms [80, 175]. They are mechanosensitive in response to mechanical tension, but can also generate forces by themselves [30]. Actin assembly by formins or Arp2/3 as well as actin severing by cofilin are involved in cell motility and migration [23, 28, 55, 150, 191].

Moreover, actin dynamics play a role in mitochondrial motility, fission mechanisms and calcium uptake [25, 34]. Actin is also required for vesicle and organelle movement and is involved in intracellular transport [95] and endocytosis processes [141]. Finally, cytokinetic ring assembly is dependent on actin and myosin [70, 141, 188], and actin is crucial for SRF signaling [68, 121].

1.2.3 Actin dynamics impact on a broad range of diseases

Cancer cell invasion and metastasis are probably the most prominent disease-related functions of actin dynamics [126, 152], i.e. entosis – a non-apoptotic form of cell death – depends on actomyosin dynamics [75].

Furthermore, actin rods were shown to associate with neurodegenerative disorders such as Alzheimer's disease [16, 120] and actin was found to regulate ROS production and cell death [2]. Nuclear actin allows virus capsid transport and viral mRNA export from the nucleus and could therefore influence the spread of viral infections, e. g. herpes [37, 47]. Dysfunctional actin dynamics are moreover responsible for myopathies or cardiomyopathies [116, 127, 185] and result in deafness and neutrophil dysfunctions [84].

1.2.4 Actin in the nucleus

Several years ago, researchers gained first evidence for the existence of nuclear actin. One of the first discoveries showed a nuclear actin "gel" in nuclei extracted from frogs (*Xenopus laevis*) oocytes [38, 63]. In 2006, nuclear localization of actin and its dynamics was assessed using FRAP imaging [117] and Belin et al. could first visualize nuclear actin filaments in fixed cells following phalloidin staining [19].

Notably, live visualization was facilitated recently by using a fluorophore-tagged anti-actin nanobody – the actin chromobody [11, 118, 148]. Furthermore, nucleocytoplasmic shuttling dynamics were revealed to be dependent on exportin 6 and importin 9 and by additional coupling to cofilin or profilin [43, 69, 169]. Moreover, SUMOylation at K284 leads to lower export rates of actin via CRM-1. [76]

Nuclear F-actin assembly is mediated by certain stimuli [136, 137] including mitotic exit [12, 137] or cell spreading and is also involved in integrin signaling [139]. Of note, serum stimulation further mediates F-actin assembly based on serum component

lysophosphatidic acid (LPA) which activates specific GPCRs for subsequent calcium release that in turn activates formins for F-actin assembly [10, 11]. Diaphanous mDia2 is involved in this process, while INF2 also regulates assembly of a perinuclear rim [161] as well as dynamic nuclear actin filament polymerization from the inner nuclear membrane upon calcium elevations [187]. Moreover, networks of nuclear F-actin can be formed upon DNA damage [20] and viral infections, as mentioned earlier (cf 1.2.3).

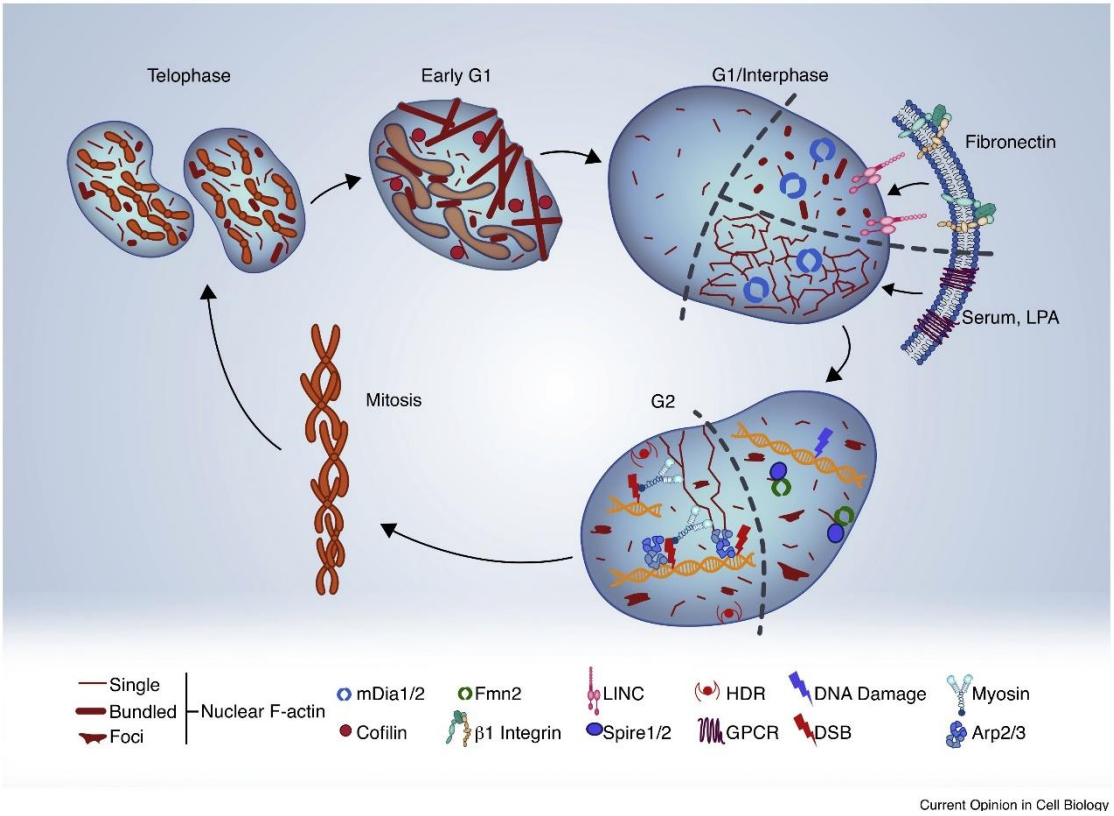

Figure 5. Nuclear F-actin assembly upon different stimuli.

In interphase nuclei, nuclear actin filament formation can be triggered by fibronectin and serum / LPA stimulation and upon DNA damage. In G2, double strand break (DSB) repair requires nuclear F-actin. After completing mitosis, early G1 nuclei exhibit nuclear actin filaments driving chromatin decondensation and nuclear volume expansion. Adapted from [137].

Besides scaffolding to help organizing nuclear contents and transcription complexes [19, 49, 69, 184], nuclear actin is also involved in NPC formation and other processes [100]. Arp5, Arp8 and histones are integrated into INO80 and other chromatin remodeling complexes, together with monomeric actin [9, 21, 93, 159] that can also bind to HDAC 1 and 2 and thus regulates histone charge which influences DNA compaction [160].

A contractile F-actin network is responsible for correct capture of chromosomes in meiosis in large nuclei, such as those in starfish oocytes [29, 111]. Actin is part of the nuclear envelope and the perinuclear rim, thus facilitating nuclear envelope breakdown, chromatin binding and chromosome congression [111, 122, 128, 138]. Together with formins, actin dynamics control DNA replication and they are involved in gene expression and transcription processes [13, 21, 134, 155, 179].

Polymerized actin and its regulators were found to be involved in DNA double strand break repair and heterochromatin repair mechanisms [32]..

1.3 Actin-binding proteins

1.3.1 Actin assembly and disassembly

The most common actin nucleators are formins, spire and the Arp2/3 complex [31]. Formins elongate linear filaments, they further act as capping proteins and impact on polarization of the filaments [10, 143, 149]. In contrast, Arp2/3 nucleates actin filaments in 70° angle on the surface of existing filaments [124]. creating Y-branched networks of F-actin that can be found in ruffles and lammellipodia [62, 151]. A third group of nucleators includes the tandem-monomer-binding nucleators Spire, JMY and COBL [31, 186, 200].

Profilin binds to G-actin(ATP), whereas the filament-depolymerizing cofilin interacts with G-actin(ADP) (Fig 3) [101] and leads to higher disassembly rates towards the pointed end [15, 28]. Additionally, tropomodulin and thymosin (cf 1.2.1) have important functions for assembly, disassembly and stability of filaments, while tropomyosin regulates myosin-binding to actin filaments and is crucial in muscle contraction [26, 59, 60, 189]. However, myosin was the first identified interaction partner of actin. Besides generating contractile force, both are also required for intracellular transport [174].

The ERM proteins ezrin, radixin and moesin are important for direct membrane interactions as well as integrity and have proposed nuclear functions [75, 103, 182].

1.3.2 Bundling proteins, crosslinking and spectrin repeats

The smallest actin-bundling protein fascin as well as villin are required for filopodia assembly in epithelial cells. Fascin which is located at cell-cell-contacts, bundles actin filaments, while villin additionally serves as nucleator and capping protein in microvilli [97]. Fimbrin – also known as plastin – has the most basic structure of an actin crosslinking protein consisting of two actin-binding domains (ABDs) and two EF-hands forming a calcium binding domain (Fig 6). The three known isoforms show distinct expression as one isoform can be found in neurons and the brain, one is restricted to intestine and kidney, while the third is expressed in hematopoetic and cancer cells [162] and to regulate immunological functions [123]. Dynacortin and coronin are further actin-bundling proteins that concentrate in highly dynamic cortical actin structures [147].

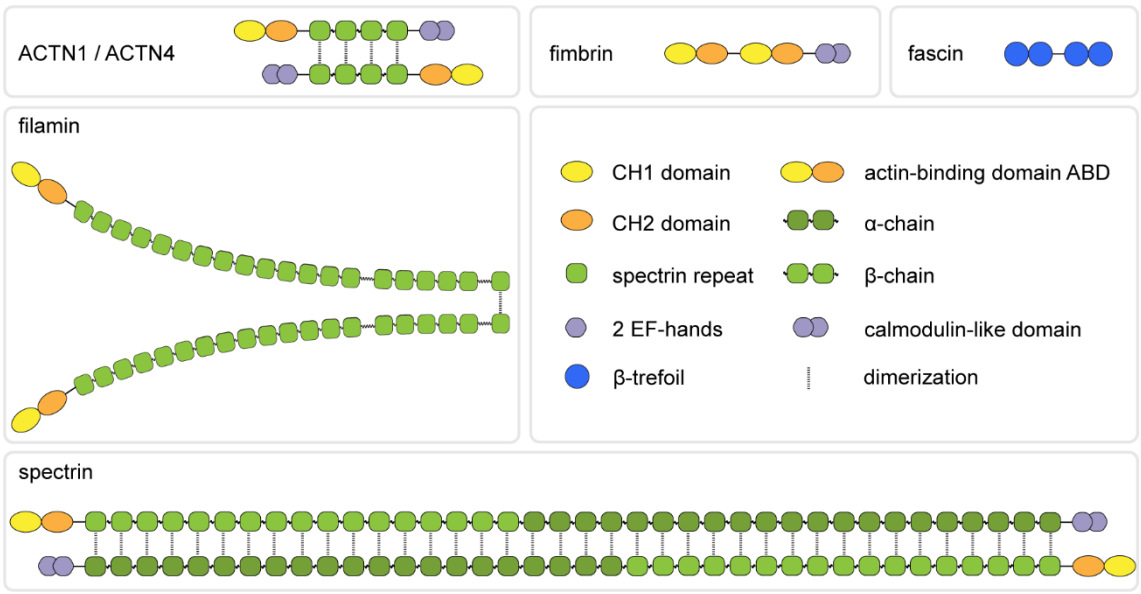

Figure 6. Structures of common crosslinking proteins.

The small actin-bundling proteins include fascin consisting of 4 β-trefoil motifs and fimbrin which exhibits a CaM and 2 ABDs. ACTNs, filamin and spectrin are members of the spectrin repeat superfamily, they dimerize via spectrin repeats (SR) and bundle actin filaments via an ABD on each monomer. CaM domain is responsible for calcium sensitivity.

A special class of actin-bundling proteins was found to consist of common structural domains, so called spectrin repeats. Spectrin repeats are large modular repeat elements first identified in the name-giving erythrocyte spectrin. In all proteins of this class, the spectrin repeats separate the N-terminal actin-binding domain from the distinct C-terminal domain that can be responsible for membrane or microfilament binding and calcium regulation [196].

Spectrin was first characterized as a cytoplasmic scaffolding protein associated with the plasma membrane where it is also involved in signal transduction. Additional investigations revealed that the isoform α-spectrin which is localized to the nuclear envelope and inside nuclei mediates DNA repair as well as scaffolding functions. β-spectrin can associate with Smad in the cytoplasm and this complex translocates to the nucleus [114, 196]. The unique hinged structure of filamin has scaffolding functions close to membranes of the cells [166]. It further facilitates cell adhesion and migration, and it suppresses tumor growth by interfering with transcription factors [195]. The striated muscle protein dystrophin and its homologue utrophin are composed of spectrin repeats and are incorporated in a complex that stabilizes the actin cortex at the plasma membrane [58]. ACTNs (also referred to as alpha actinins) are the latest members of the spectrin repeat superfamily, whose isoforms ACTN2 and ACTN3 are found in skeletal muscle, while ACTN1 and ACTN4 are ubiquitously expressed in non-muscle cells [125].

All spectrin repeat proteins can commonly be observed in the nuclear compartment or envelope [196]. Notably, structural or expression alterations in all bundlers impact on tumorigenesis and could be used as cancer prognosis markers [166].

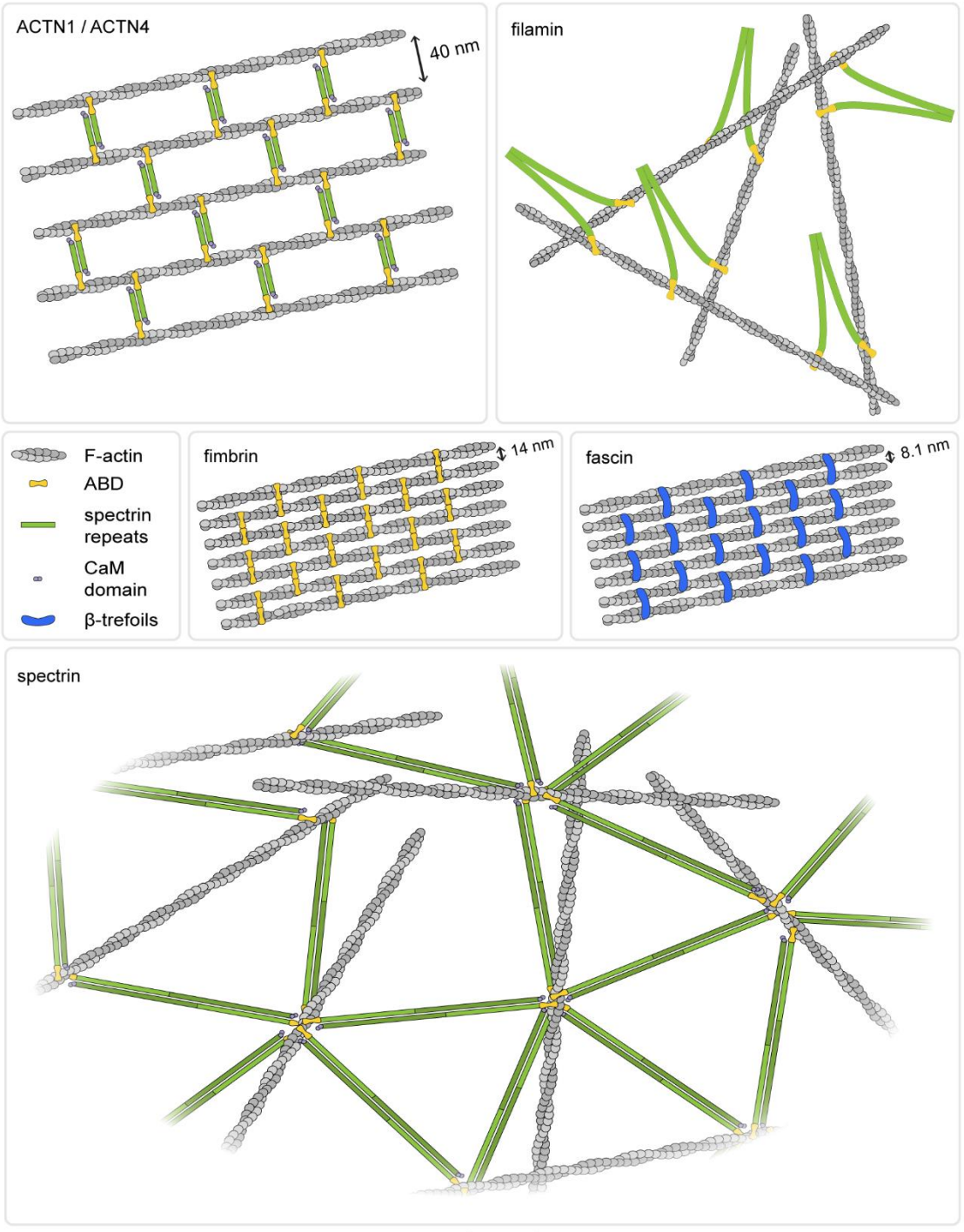

Figure 7. Different crosslinkers show distinct actin-bundling patterns.

ACTN's, fimbrin und fascin bundle parallel actin bundles with indicated spacing between the single filaments. Filamin forms flexible structures and bundling by spectrin leads to stable networks.

1.4 ACTNs

1.4.1 Structure and regulation of ACTN1 and ACTN4

Non-muscle isoforms ACTN1 (892 amino acids, 103 kDa) and ACTN4 (911 amino acids, 105 kDa) share structural similarities (Fig 8 A, B) as well as similar localization patterns in F-actin-rich compartments, such as stress fibers and adhesion and junction proteins, including lamellipodia and filopodia [42, 45, 94, 131]. Notably, nucleocytoplasmic shuttling of ACTN4 – despite lacking a conventional NLS – was observed in a CRM-1 dependent manner [105] and upon inhibition of phosphatidylinositol 3 kinase or actin depolymerization [78]. Stimulation with tumor necrosis factor (TNF) or epithelial growth factor (EGF) also led to translocation of ACTN4 into the nucleus, while ACTN1 did not respond to any of these stimuli [14].

The rod-shaped structures of both ACTN isoforms reveal four spectrin repeats (SR) facilitating dimerization of two ACTN molecules – preferentially heterodimers of ACTN1 and ACTN4 (Fig 8 C) [51, 53]. N-terminal calponin homology domains 1 and 2 form an actin binding domain [57] that – by opening up – enables crosslinking of two actin filaments by a single ACTN dimer, thus forming parallel or antiparallel F-actin bundles [57, 72, 112, 172]. Unipolar actin filament bundles – with their barbed end facing focal adhesion sites – are severed, capped and form contractile bundles with myosin [30, 40]. However, in order to incorporate myosin and to generate force, antiparallel actin filaments are required [30]. The C-terminal Calmodulin-like domain (CaM) of the calcium sensitive non-muscle isoforms consists of four EF hand motifs that bind calcium and regulate actin-binding properties of the adjacent ABD via conformational changes [164]. At high Ca^{2+} concentrations, actin binding is reduced or abolished, while low Ca^{2+} levels enable binding to actin filaments (Fig 8 C) [164]. ACTNs are further regulated by phosphoinositide binding, phosphorylation at tyrosine residues or proteolytic cleavage by proteases, e.g. calpain [131].

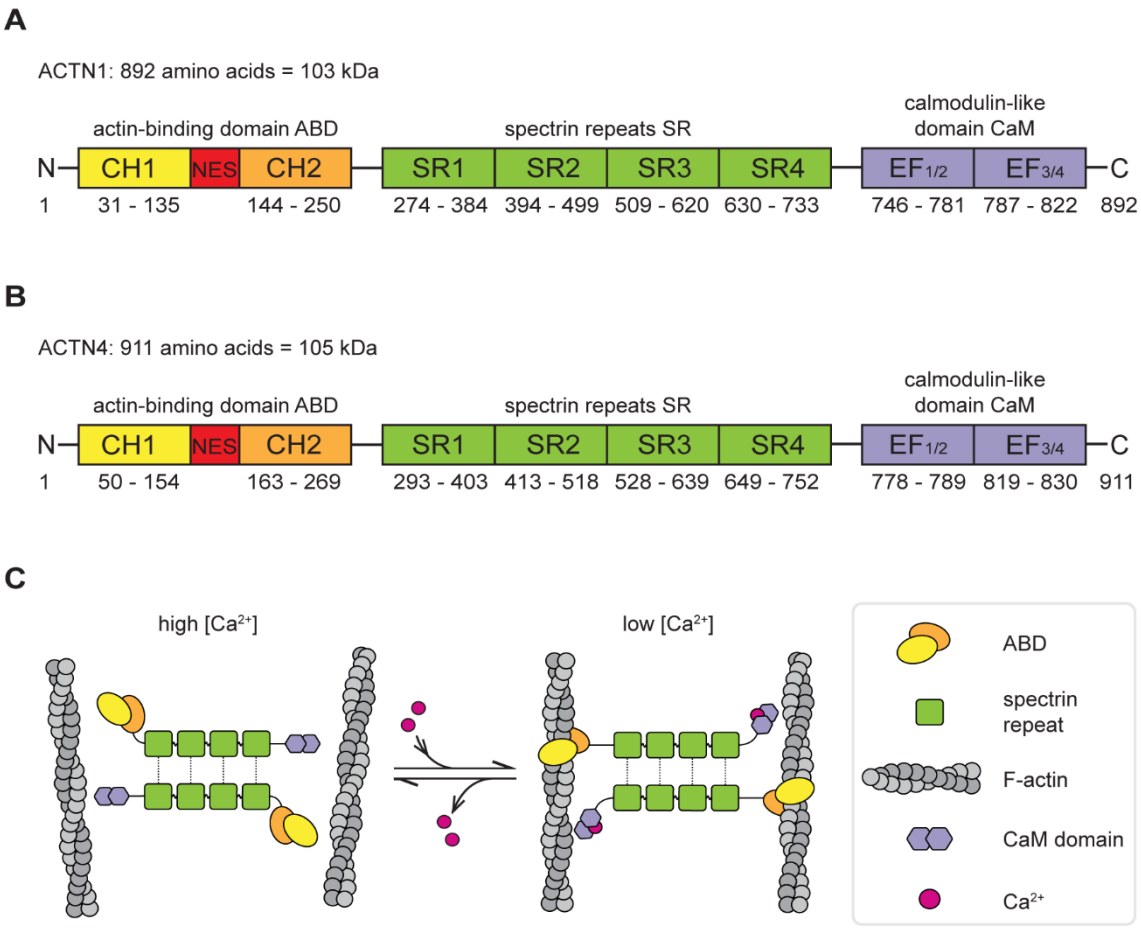

Figure 8. Structure and regulation of ACTN.

(A) *Structure of ACTN1.* ***(B)*** *Structure of ACTN4.* ***(C)*** *Regulation of non-muscle ACTNs: Ca^{2+} binding via the CaM domain und conformational changes diminish actin-binding by the ABD.*

1.4.2 Functions of ACTN1 and ACTN4

ACTNs play important roles in various cytoplasmic processes and interact with a wide range of adhesion and motility associated proteins including vinculin, paxillin, zyxin, α-catenin, focal adhesion kinase (FAK), palladins, talin and PDLIM proteins as well as the transmembrane proteins ICAM's and integrins [131, 164]. Furthermore, these crosslinkers are crucial for cleavage furrow formation and correct cytokinesis, as ACTN knockdown leads to reduced F-actin levels at the furrow resulting in slower ingression rates [53]. In addition, ACTN1 and ACTN4 are involved in stress fiber formation and suppression [48, 94].

Besides the well-described cytoplasmic functions of ACTNs, more and more potential nuclear functions of ACTN4 became apparent. Studies of the past few years showed

interactions of ACTN4 with the INO80 chromatin remodeling complex and with HDAC7 [53]. Moreover, ACTN4 potentiates myocyte enhancer factor 2 (MEF2) transcription factor activity and regulates gene expression by interacting with the glucocorticoid (GR) and estrogen receptor α (ERα) [96, 198]. It was further found to be involved in NF-κB signaling [3].

1.4.3 Dysfunctions of ACTN1 and ACTN4 result in severe cases of disease

Congenital macrothrombocytopenia (cMTP) is characterized by reduced blood platelet formation and abnormal cytoskeletal organization in affected blood cells. Mutations in ACTN1 were found in patients suffering from cMTP resulting in mild to severe bleeding tendency. Cell culture models revealed an altered actin cytoskeleton structure caused by the observed missense mutations that are thought to reduce actin binding [106].

ACTN4 gain-of-function mutations found in podocytes of dominant inherited focal segmental glomerulosclerosis (FSGS) displayed a strong binding to F-actin bundles and altered localization patterns [17, 192]. Furthermore, podocytes wrap around glomerular capillaries in the Bowman's capsule and are exposed to enormous mechanical stress induced by expansion and retraction of these vessels. Mutated ACTN4 with increased actin-binding leads to stiff podocyte foot processes; podocytes fail to recover from the stretch and detach subsequently resulting in chronic kidney disease [41]. In some reported cases, kidney function declined until renal failure required peritoneal dialysis or transplantation. Notably, proteinuria recurred upon transplantation in some patients [192].

In addition to the organ-specific effects, both non-muscle ACTN's were also observed to be involved in cancer cell proliferation and invasion [166]. Especially overexpressed or mutant ACTN4 is implicated in invasiveness and poor prognosis in various tumors, including melanoma, breast, ovarian and prostate cancer, lung and squamous carcinoma [73, 79, 81, 194, 197]. Already back in the 1990's, Honda et al. found that ACTN4 localizes to the leading edge of migrating cells and that its infiltrative phenotype in breast cancer correlates with a poorer prognosis [78]. Furthermore, they suggest an importance of ACTN4 translocation into the nuclear compartment for this process. All in all, studies reveal a strong correlation between expression of ACTN4 and invasiveness of a tumor [53].

2. Aim of this study

Cytoplasmic actin-bundling functions of ACTNs were reasonably well studied in the past decades with disease significance in cancer, cMTP or FSGS.

Moreover, ACTNs were implicated in chromatin remodeling, in transcription processes and showed interactions with nuclear receptors and thus imply critical nuclear functions of ACTNs in tumorigenesis and metastasis [81]. Our group recently identified ACTN4 as a potential interaction partner of postmitotic nuclear actin filaments [12], but exact functions of ACTNs in nuclear actin dynamics and regulation still remained unclear.

The aim of this study was to characterize the impact of ACTN1 and ACTN4 on nuclear F-actin bundling, structure and organization in early G1 and its downstream effect on nuclear volume expansion and chromatin rearrangement.

We provide evidence for non-muscle ACTNs playing critical roles in postmitotic nuclear reconstruction and chromatin reorganization.

3. Materials and methods

3.1 Materials

Table 1. Reagents

NAME	SUPPLIER
Acetic Acid	Roth
ATP = Adenosine-5´-Triphosphate	Sigma-Aldrich
Agarose	Roth
Ampicillin (Amp)	Roth
APS = Ammonium persulfate	Merck
BES = N, N-Bis(2-hydroxyethyl)-2-aminoethane sulfonic acid	Merck
Biotin-XX Phalloidin	Thermo Fisher Scientific
Bromophenol blue	Roth
BSA = Bovine serum albumin	Roth
$CaCl_2$ = Calcium chloride	Roth
Catalase 40.000-60.000 units/mg protein	Sigma-Aldrich
Chloroform	Roth
Corning® Matrigel® phenol red-free	VWR
DAKO Fluorescent mounting medium	Agilent
DMEM High glucose	Capricorn Scientific
DMSO = Dimethylsufloxide	Thermo Fisher Scientific
DNA ladder 1kb plus	Thermo Fisher Scientific

NAME	SUPPLIER
DNA loading dye 6x	Thermo Fisher Scientific
dNTP Mix = Desoxyribonucleoside Triphosphates	Promega
Doxycyclin	Sigma-Aldrich
DTT = 1,4-Dithio-DL-threitole	BioChemika
EDTA = Ethylenediamintetraacetic acid	Roth
EGTA = Ethylenglycol-bis(2-aminoethylesther)-tetraacetic acid	Sigma-Aldrich
Ethidium bromide	Roth
EtOH = Ethanol 99,8% p.a.	Roth
FCS = Fetal calf serum	Thermo Fisher Scientific
FLAG M2 affinity gel (conjugated agarose beads)	Sigma-Aldrich
FluoSphere infrared fluorescent Carboxylate-Modified Microspheres (“IR beads”)	Thermo Fisher Scientific
Formaldehyde solution 37% in H_2O	Roth
Gateway™ LR Clonase™ (with proteinase K)	Invitrogen
GeneRuler 1kb plus DNA ladder	Thermo Fisher Scientific
Glucose oxidase	Sigma-Aldrich
Glutaraldehyde solution 25% in H_2O	Sigma-Aldrich
Glycerol 86% in H_2O	Roth
H_2O nuclease-free	Thermo Fisher Scientific
H_2O_2 = Hydrogen peroxide 30% in H_2O	Sigma-Aldrich
HEPES = 2-(4-(2-Hydroxyethyl)-1-piperazinyl)-ethanesulfonic acid	Roth
Image-iT™ FX signal enhancer	Invitrogen

NAME	SUPPLIER
iQ SYBR-Green® Supermix	Bio-Rad
Isopropanol = 2-Propanol 99,95% p.a.	Roth
Kanamycin (Kan)	Roth
KCl = Potassium chloride	Roth
Lipofectamine 2000	Thermo Fisher Scientific
Lipofectamine RNAiMAX	Thermo Fisher Scientific
L-lysine	Sigma-Aldrich
Luminol	Sigma Aldrich
MEA-HCl = 2-Mercaptoethylamine = Cysteamine-HCl	Sigma-Aldrich
MeOH = Methanol 99,9% p.a.	Roth
MES = 2-(N-Morpholino)ethanesulfonic acid	Sigma-Aldrich
$MgCl_2$ = Magnesium chloride	Roth
Milk powder (fat free)	Roth
$Na_2H_2PO_4$ = Sodium dihydrogenphosphate	Roth
$NaBH_4$ = Sodium borohydride	Sigma-Aldrich
NaCl = Sodium chloride	Roth
NaDOC = Sodium deoxycholate	Sigma-Aldrich
NaN_3 = Sodium azide	Sigma-Aldrich
NaOH = Sodium hydroxide	Sigma-Aldrich
NP-40 = TERGITOL™	Sigma-Aldrich
OptiMEM	Life Technologies
PageRuler Prestained Protein Ladder	Thermo Fisher Scientific

NAME	SUPPLIER
PBS = Phosphate-buffered saline	Capricorn
p-Coumaric acid	Sigma Aldrich
PCR primer	Sigma-Aldrich
Phosphatase inhibitor 3	Sigma-Aldrich
Phusion Hot Start II High-Fidelity DNA Polymerase, GC buffer	Thermo Fisher Scientific
Potassium chloride (KCl)	Roth
Propidium iodide solution	BioChemika
Protease inhibitor cocktail (cOmplete)	Roche
Random Hexamer Primer	Thermo Fisher Scientific
Restriction enzymes	Thermo Fisher Scientific
RevertAid Reverse Transcriptase	Thermo Fisher Scientific
RiboLock RNase Inhibitor	Thermo Fisher Scientific
RNAse A	Sigma-Aldrich
RO3306	Merck
RotiPhoreseR Gel 30 (Acrylamide-Bisacrylamide solution)	Roth
SDS = Sodium dodecyl sulphate	Roth
siRNA FlexiTube	QIAGEN
Streptavidin-coupled (magnetic) Dynabeads	Thermo Fisher Scientific
T4 DNA ligase, T4 ligase buffer	Thermo Fisher Scientific
TCEP = Tris(2-Carboxyethyl)phospine	Roth
TEMED = Tetramethylethylenediamine	Applichem

NAME	SUPPLIER
Topo 10 cells	Invitrogen
TRIS = Tris(hydroxymethyl)-aminomethan	Roth
Triton X-100	Sigma-Aldrich
TRIzol	Invitrogen
Trypsin-EDTA 0.05%	Capricorn Scientific
Tryptone	Roth
Tween-20	Roth
WST Cell Proliferation Reagent	Roche
Yeast extract	Roth
α-D-Glucose monohydrate	Roth
β-Mercaptoethanol	Sigma-Aldrich

Table 2. Antibodies and fluorescent dyes

ANTIBODY	SUPPLIER	DILUTION
Alexa Fluor conjugated sondary antibodies	Thermo Fisher Scientific	IF 1:400 (in 5% BSA in PBS)
anti-ACTN1 D6F6	Cell Signaling	IF 1:200 (in 5% BSA in PBS) WB 1:1000 (in 5% BSA in TBST)
anti-ACTN4 polyclonal	Enzo	IF 1:200 (in 5% BSA in PBS) WB 1:1000 (in 5% BSA in TBST
anti-FLAG, HRP conjugated	Sigma-Aldrich	WB 1:5000 (in 5% milk in TBST)
anti-Histone H3 (D1H2)	Cell Signaling	WB 1:1000 (in 5% BSA in TBST)
anti-Mouse IgG, HRP conjugated	Amersham	WB 1:5000 (in 5% milk in TBST)
anti-Rabbit IgG, HRP conjugated	Bio-Rad	WB 1:5000 (in 5% milk in TBST)
anti-α-Tubulin Rabbit (2125S)	Cell Signaling	WB 1:1000 (in 5% milk in TBST)
anti-β-Actin Mouse (2228)	Sigma-Aldrich	WB 1:1000 (in 5% milk in TBST)
Anti-pan-Actin Mouse (ACTN05, C4)	Novus Biologicals	WB 1:5000 (in 5% milk in TBST)
DAPI = 4´,6-Diamidin-2-phenylindole	Sigma Aldrich	IF 10 ng/ml (in 5% BSA in PBS)
Phalloidin, conjugated to Alexa Fluor 488 / 647	Thermo Fisher Scientific	IF 1:400 (in 5% BSA in PBS) STORM 1:50 (in PBS)
SiR actin	Spirochrome	IF 1:1000 (in growth medium)
SNAP-Cell 647 SiR 488 Oregon Green	New England BioLabs	IF 1:500 – 1:4000 (in growth medium)

Table 3. Special equipment, devices and working materials

NAME	SUPPLIER
AE200 analytical balance	Mettler
Biometra PCR-Thermocycler, Biometra TRIO	Analytik Jena AG
Cell culture – 0.45 µm filter	Merck
Cell culture – Cell scraper	Sarstedt
Cell culture – Eppendorf tubes 1.5 and 2 ml	Sarstedt
Cell culture – Flasks, dishes and plates in any format	Sarstedt
Cell culture – ibiTreat µ-slide 8 well classic / grid-500	ibidi
Cell culture – Syringes, needles	B. Braun
Centrifuge 5415R	Eppendorf
DH5α competent bacterial cells	Self-made from Topo 10 cells
Falcon tubes 15 and 50 ml	Sarstedt
Forma Series II 3110 Water-Jacketed CO_2 Incubators	Thermo Fisher Scientific
GeneAmp® PCR System 9700	Applied Biosystems
Guava easyCyte™ Flow Cytometer	Millipore
Heraeus Biofuge Stratos	Thermo Fisher Scientific
Heraeus incubator Function Line	Thermo Fisher Scientific
Heraeus laboratory shaker MaxQ 4000	Thermo Fisher Scientific
Horizontal Electrophoresis System (DNA)	Bio-Rad
iMark™ Microplate Reader	Bio-Rad
INFINITY gel documentation	Peqlab

NAME	SUPPLIER
Inverted Ti-Eclipse microscope with custom build setup (more information listed in 3.4.3)	Nikon
LSM 700 confocal microscope, 63x, 1.4 NA oil objective	Zeiss
LSM 800 confocal microscope, 63x, 1.4 NA oil objective	Zeiss
Luminoskan™ Ascent Microplate Luminometer	Thermo Fisher Scientific
Magnetic stand	Thermo Fisher Scientific
Mini-Trans-Blot System, Electrophoresis equipment	Bio-Rad
NanoDrop 1000	Peqlab
PIPETBOY	Integra
Pipette tips, serological pipettes	Greiner
PowerPac 300	Bio-Rad
Precision Scale 572	Kern & Sohn
Protran Nitrocellulose Transfer Membrane 0.45 µm	Whatman
qPCR CFX Connect Real-Time System	Bio-Rad
SONOPLUS GM70 sonicator	BANDELIN
SORVALL RC 5B Plus	Thermo Fisher Scientific
Super RX-N Full Medical X-Ray Film	FUJI Film
Thermomixer compact	Eppendorf
X-Ray Processor	Medical Index GmbH

Table 4. Biochemical kits

NAME	SUPPLIER
Dual-Luciferase® Reporter Assay System	Promega
NucleoSpin® gel and PCR clean-up	Macherey-Nagel
NucleoSpin® Plasmid	Macherey-Nagel
NucleoBond® Xtra Midi	Macherey-Nagel
DC™ Protein Assay	Bio-Rad

Table 5. Software

NAME	SUPPLIER
Ascent™	Thermo Fisher Scientific
FIJI (ImageJ)	Open Source (National institute of Health) [156]
guavaSoft 2.7	guava
Illustrator CC 2017	Adobe
Imaris 8.3.1	Bitplane
MS Office 2016	Microsoft
Photoshop CC 2017	Adobe
Prism 7	Graph Pad Software
Serial Cloner 2.6.1	Serial Basics
SnapGene Viewer 4.1.7	GSL Biotech LLC
Zen black	Zeiss
Zen blue 2.6	Zeiss

Table 6. Standard solutions, buffers and growth media

SOLUTION	COMPOSITION
Actin Stabilization Buffer (ASB)	PIPES 50mM pH 6,9 NaCl 50 mM $MgCl_2$ 5mM EGTA 5 mM ATP 2 mM Triton X-100 0.1 % Tween-20 0.1 % NP-40 0.1 % β-mercaptoethanol 0.1 % Protease inhibitor (20X) Phosphatase inhibitor (100X)
BES-buffered saline (2X BBS)	BES 50 mM NaCl 280 mM Na_2HPO_4 1.5 mM pH 6.94-6.98
Blocking buffer for immunoblotting	Milk powder 5 % (w/v) in TBST
Blocking buffer for immunofluorescence	BSA 5 % (w/v) NaN_3 0.01 % (optionally) In PBS
Cytoskeleton buffer	MES 10 mM NaCl 150 mM EGTA 5 mM Glucose 5 mM $MgCl_2$ 5 mM pH 6.1
Cell freezing medium	DMSO 5 % FCS 20 % in DMEM

SOLUTION	COMPOSITION
ECL – Solution S1	90 ml H_2O 10 ml Tris pH 8.4 1 ml Luminol 450 µl p-Coumaric acid
ECL – Solution S2	90 ml H_2O 10 ml Tris pH 8.4 100 µl H_2O_2
Laemmli buffer 4x	Glycerol 28 % (v/v) EDTA 10 mM SDS 5.7 % (v/v) β-mercaptoethanol 4.7 mg/ml Bromophenol blue 3.5 mg/ml Tris-HCl 286 mM pH 6.8
LB agar	NaCl 1 % (w/v) Yeast extract 0.5 % (w/v) Tryptone 1 % (w/v) Agar 1.5 % (w/v)
LB medium	NaCl 1 % (w/v) Yeast extract 0.5% (w/v) Tryptone 1 % (w/v)
Phosphate-buffered Saline = PBS	Na_2HPO_4 8 mM KH_2PO_4 1.5 mM NaCl 137 mM KCl 2.7 mM pH 7.4

SOLUTION	COMPOSITION
RIPA buffer (low stringent)	Tris-HCl 25 mM NaCl 50 mM EDTA 1 mM Triton X-100 0.5% SDS 0.1 % (w/v) NaDOC 0.25% (w/v) $MgCl_2$ 5 mM Protease inhibitor cOmplete (20X)
SDS-PAGE – Running buffer 1X	Glycine 192 mM SDS 0.1 % (w/v) Tris-HCl 25 mM pH 8.3
SDS-PAGE – Separating gel	RotiPhorese® Gel 30 8–15% (v/v) TEMED 9.5 µM SDS 0.1 % (w/v) Tris-HCl 0.36 M APS 0.1 % (w/v) pH 8.8
SDS-PAGE – Stacking gel	RotiPhorese® Gel 30 19% (v/v) TEMED 14.5 µM SDS 0.1 % (w/v) Tris-HCl 0.12 M APS 0.15 % (w/v) pH 6.8

SOLUTION	COMPOSITION
STORM – Enzyme stock	Catalase 100 µl TCEP 1 M 200 µl Glycerol 25 ml dH_2O 22.5 ml KCl 1 M 1.25 ml Tris-HCl 1 ml Glucose oxidase 50 mg
STORM – Glucose stock	Glucose 5 g dH_2O 45 ml glycerol 5 ml
STORM – MEA stock	MEA-HCl 1.136 g dH_2O 10 ml
STORM – Switching buffer	PBS 450 µl Glucose stock 400 µl MEA stock 100 µl Enzyme stock 50 µl
Subcellular fractionation – Cell lysis buffer P1	HEPES 10 mM KCl 10 mM EGTA 0.1 mM DTT 1 mM Protease inhibitor cOmplete (20X) Phosphatase inhibitor 3 (100X) pH 7.9
Subcellular fractionation – Nuclear extraction buffer P2	HEPES 20 mM NaCl 500 mM Glycerol 15% EGTA 1 mM Triton X-100 0.5 % pH 7.9

SOLUTION	COMPOSITION
Tris-buffered Saline with Tween20 = TBST	NaCl 500 mM Tris-HCl 20 mM Tween-20 1 % (v/v) pH 7.5
Transfer buffer for immunoblotting	Glycine 192 mM Tris-HCl 25 mM Methanol 20 % (v/v) pH 8.5
Tris-Acetate-EDTA = TAE	EDTA 2 mM Tris-HCl 40 mM Acetic acid 20 mM pH 8.0

3.2 Cell culture, transfection and transduction

3.2.1 General cell culture

HEK293T, NIH3T3 and RPE-1 were maintained in DMEM (HPSTA – high glucose, stable glutamine and sodium pyruvate) supplemented with 10% fetal calf serum (FCS) under standard conditions at 37°C in a 5% CO_2 environment.

Table 7. Cell lines

NAME	TYPE
HEK293T	Human embryonic kidney cells
NIH3T3	Mouse embryonic fibroblast cells
RPE-1	Human retinal pigmented epithelial cells

3.2.2 Transfection of DNA

HEK293T cells were transfected using the calcium phosphate method. Briefly, cells were seeded in cell culture dishes 24 h before transfection. For a 3.5 cm dish, DNA was diluted and mixed in 112.5 µl ultrapure bidest. H_2O. 12.5 µl of a 2.5M $CaCl_2$ solution was added and mixed, followed by 125 µl 2X BBS. After mixing and blowing air bubbles, the transfection mixture was incubated for 15-30 min at RT before adding it dropwise to the subconfluent cells. 4 h after transfection, the medium was replaced with fresh 10% FCS in DMEM and cells were incubated overnight (o/n) at 37 °C in a 5 % CO_2 environment before further application.

NIH3T3 and RPE-1 cells were transfected using Lipofectamine 2000.. Briefly, the plasmids were mixed in 250 µl OptiMEM and 5 µl Lipofectamine 2000 was added. The transfection mixture was vortexed vigorously for 10 s, incubated at RT for 10-30 min and added to subconfluent cells in a 3.5 cm cell culture dish. Before carrying out further experiments, cells were incubated o/n (37°C, 5% CO_2).

3.2.3 Transfection of siRNA

siRNAs (FlexiTube, Qiagen) were transfected using Lipofectamine RNAiMAX. For siRNA transfection of cells seeded in a 3.5 cm cell culture dish, 2 µl siRNA of a 20 µM siRNA solution was added to 250 µl OptiMEM yielding a final concentration of 10 nM. 5 µl Lipofectamine RNAiMAX was added to this mix and – after vortexing for 10 s – incubated at RT for 20 min. Afterwards, the transfection mix was added to the medium of subconfluent cells and incubated for 72 h at 37 °C and 5 % CO_2.

Table 8. siRNA targeting sequences

NAME	SEQUENCE 5' TO 3'	COMMENTS
AllStars Negative Control siRNA	AATTCTCCGAACGTGTCACGT	negative control for knockdown exp.
Mm_ACTN1_2	CCGAGTTGATTGACTATGGAA	used for knockdown
Mm_ACTN4_5	CAGGGATGGGCTCAAACTTAT	used for knockdown
Hs_ACTN1_9	GACCATTATGATTCTCAGCAA	used for knockdown
Hs_ACTN4_5	ACGCAGCATCGTGGACTACAA	used for knockdown
Hs_ACTN1_7	AAGGATGATCCACTCACAAAT	template for cloning
Hs_ACTN4_7	CAGGACATGTTCATCGTCCAT	template for cloning

3.2.4 Lentiviral transductions

HEK293T cells were seeded in a 10 cm cell culture dish and transfected the day after using calcium phosphate method. 4-6 µg plasmid DNA and 8 µg of each pMD2.G and psPAX2 were diluted in 450 µl ultrapure bidest H_2O. 50 µl of a 2.5M $CaCl_2$ solution was added and mixed, followed by 500 µl 2X BBS. Subconfluent cells were transfected as described in 3.2.2.

After 48 h, growth medium containing lentivirus was harvested, filtered and added to target cells that have been seeded into 3.5 cm cell culture dishes right before transduction. 24 h after transduction, medium was replaced by 10 % FCS in DMEM. Cells were kept under BSL2 conditions until virus titer was under detection limit. If necessary, cells were subjected to FACS by Dr. Hartmann Raifer, group of Prof. Lohoff at BMFZ in Marburg.

3.3 Molecular biological methods

3.3.1 Molecular cloning

DNA fragments were obtained and amplified by polymerase chain reaction (PCR) using Phusion Hot Start II High-Fidelity DNA Polymerase in 5X GC buffer (according to manufacturer´s protocol). Existing plasmids were used as templates for PCR reactions (Table 10).

The PCR reaction was composed of additional 10 ng DNA template, 100 nM of each primer (forward and reverse, table 11), 3 µl DMSO and it was filled with ddH_2O to a total volume of 50 µl. PCR reactions were performed on a Biometra Thermocycler with the following settings:

Table 9. PCR program for molecular cloning

STEP	TEMPERATURE	TIME	COMMENTS
Denaturation	98 °C	30 s	
Denaturation	98 °C	10 s	
Annealing	X °C	30 s	X: 64°C – 72°C 30–35 cycles total
Extension	72 °C	X s	X: 30 s – 3 min
Final extension	72 °C	5 min	
Storage	4 °C	∞	

The PCR products were separated on 1 % agarose gels containing 0.01 % ethidium bromide, were visualized under UV light and extracted from the gels. These fragments and the vectors were digested using appropriate DNA restriction endonucleases following manufacturer´s instructions. After 2 h, the digestion mix was separated using agarose gels, followed by extraction of correct fragments of insert and vector. Both were ligated using T4 ligase in accordance to the manufacturer's protocol. 6 µl of the ligation reaction was transformed into DH5α competent bacterial cells. Cells were plated on LB agar (containing ampicillin or kanamycin, depending on the vector´s resistance cassette) and incubated at 37°C over night (o/n). Bacterial colonies were picked and incubated o/n

in 4 ml liquid LB medium containing respective antibiotics. Plasmids were extracted from bacterial cells by using the NucleoSpin® Plasmid Miniprep Kit.

All extracted plasmids were sent for DNA sequencing, conducted by Microsynth SeqLab.

Table 10. Expression vectors and existing constructs

NAME	COMMENTS / SOURCE
Actin-Chromobody-mCherry-NLS	cloned by Michael Melak, Robert Grosse Lab, Freiburg, Germany (Source: ChromoTek) [148]
F-Tractin mApple	gift from Johanna Ivaska, Turku, Finland
pEFi Flag-GFP	cloned by Dominique Brandt, Robert Grosse Lab, Freiburg, Germany
pEGFP-N1	Clontech
pEGFP-N1 ACTN1	Addgene
pEntr11	Invitrogen
pInducer20 Puro	G418 selection cassette was replaced by Puro resistence, gift from Thorsten Stiewe, Marburg, Germany
pLenti6.3 Flag ACTN4	gift from Bodo B. Beck, Humangenetics, Cologne, Germany
pMD2.G	Addgene
pSNAP-Flag-N1	cloned by Dominique Brandt, Robert Grosse Lab, Freiburg, Germany
psPAX2	Addgene
pWPXL H2B mCherry	cloned by Jameel Khaan, Robert Grosse Lab, Freiburg, Germany

Table 11. Protocols, materials and primers for molecular cloning

Table 11.1 Common constructs

ACTN1 FLAG-SNAP-N1			
TEMPLATE	**VECTOR**	**OLIGO NAME**	**SEQUENCE 5' TO 3'**
pEFi Flag-GFP	pEGFP-N1 ACTN1	Flag fw Sal1	ATATATGTCGACGATGGATTACAAGGACGATGAC
		SNAP rev Not1	ATATATGCGGCCGCTTAACCCAGCCCAGGCTTGCCCAG

ACTN1 SNAP-FLAG-N1			
TEMPLATE	**VECTOR**	**OLIGO NAME**	**SEQUENCE 5' TO 3'**
pEGFP-N1 ACTN1	pSNAP-Flag-N1	ACTN1 fw Xho1	ATATATCTCGAGATGGACCATTATGATTCTCAGCAAACCAAC
		ACTN1 rev EcoRI	GAATTCGGAGGTCACTCTCGCCGTACAGC

ACTN4 SNAP FLAG-N1			
TEMPLATE	**VECTOR**	**OLIGO NAME**	**SEQUENCE 5' TO 3'**
pLenti6.3 Flag ACTN4	pSNAP-Flag-N1	ACTN4 fw Xho1	ATATATCTCGAGATGGTGGACTACCACGCGGCGAACC
		ACTN4 rev EcoRI	ATATATGAATTCGCAGGTCGCTCTCGCCATACAAGGCCGTG

ACTN1 FLAG-N1			
TEMPLATE	**VECTOR**	**OLIGO NAME**	**SEQUENCE 5’ TO 3’**
ACTN1 Flag-SNAP-N1	pEGFP-N1	ACTN1 fw Xho1	ATATATCTCGAGATGGACCATTATGATTCTCAGCAAACCAAC
		Flag rev Not1	ATATATGCGGCCGCCTACTTGTCGTCATCGTCCTTGTAATC

ACTN4 FLAG-N1			
TEMPLATE	**VECTOR**	**OLIGO NAME**	**SEQUENCE 5’ TO 3’**
pLenti6.3 Flag ACTN4	pEGFP-N1	ACTN4 fw Xho1	ATATATCTCGAGATGGTGGACTACCACGCGGCGAACCAGTC
		ACTN4 rev Flag Not1	ATATATGCGGCCGCTCACTTGTCGTCATCGTCCTTGTAATCTCCCAGGTCGCTCTCGCCATACAAGGC

Table 11.2 Deletion mutants and point mutations

Deletion mutants and point mutations were created using conversion extension method [88]. Constructs were generated by overlap PCR with DNA fragments resulting from the first PCR reactions.

Figure 9. Deletion mutants and point mutations of ACTN4.

ACTN4 mutants with either deleted regions or point mutations were cloned using restriction enzymes. The exact procedures are explained in the corresponding paragraphs. Color scheme as indicated.

ACTN4 ΔCH1 SNAP-FLAG-N1			
TEMPLATE	**VECTOR**	**OLIGO NAME**	**SEQUENCE 5’ TO 3’**
ACTN4 Flag-N1	pSNAP-Flag-N1	P1 fw	GAGGTCTATATAAGCAGAGCTGGTTTAG
		P3 mut Nhe1 fw	CGTCAGATCCGATACCGCTACCGGACTC
		P2 rev Not1	GCCATGGCCTTGTCGTCATCGTCCTTG
		P4 ACTN4 CH1 rev	CTTCCACGAGATGTCCTGGATGGCCTTCTCCCAGGCCGGGTCCAGC

ACTN4 ΔCH2 SNAP-FLAG-N1			
TEMPLATE	**VECTOR**	**OLIGO NAME**	**SEQUENCE 5’ TO 3’**
ACTN4 Flag-N1	pSNAP-Flag-N1	P1 fw	GAGGTCTATATAAGCAGAGCTGTTTAG
		P3 mut Nhe1 fw	CGTCAGATCCGATACCGCTACCGGACTC
		P2 rev Not1	GCCATGGCCTTGTCGTCATCGTCCTTG
		P4 ACTN4 CH2 rev	CAGTTTCAGCCTTCTGCGCTCCCTCTTCCACGGAGATGTCCTG

ACTN4 ΔSR2 SNAP-FLAG-N1			
TEMPLATE	**VECTOR**	**OLIGO NAME**	**SEQUENCE 5’ TO 3’**
ACTN4 Flag-N1	pSNAP-Flag-N1	P1 fw	GAGGTCTATATAAGCAGAGCTGGTTTAG
		P3 mut Nhe1 fw	CGTCAGATCCGATACCGCTACGGACTC
		P2 rev Not1	GCCATGGCCTTGTCGTCATCGTCCTTG
		P4 ACTN4 SR2 rev	CCCACTTGGAGTTGATGATTTGGTCGAGCCGCTCCAGCCTGC

ACTN4 ΔSR23 SNAP-FLAG-N1			
TEMPLATE	**VECTOR**	**OLIGO NAME**	**SEQUENCE 5’ TO 3’**
ACTN4 Flag-N1	pSNAP-Flag-N1	P1 fw	GAGGTCTATATAAGCAGAGCTGGTTTAG
		P3 mut Nhe1 fw	CGTCAGATCCGATACCGCTACGGACTC
		P2 rev Not1	GCCATGGCCTTGTCGTCATCGTCCTTG
		P4 ACTN4 SR23 rev	CGTTGGACTGCTGCTTGCTCTGGTCGAGCCGCTCCAGCCTGCGG

ACTN4 K255E SNAP-FLAG-N1			
TEMPLATE	**VECTOR**	**OLIGO NAME**	**SEQUENCE 5’ TO 3’**
ACTN4 Flag-N1	pSNAP-Flag-N1	P1 fw	GAGGTCTATATAAGCAGAGCTGGTTTAG
		P3 mut Nhe1 fw	CGTCAGATCCGATACCGCTACCGGACTC
		P2 rev Not1	GCCATGGCCTTGTCGTCATCGTCCTTG
		P4 rev ACTN4 K255E	GGACACGTAAGTCATGATGGCCTCCTCATCTGGCCTCAG

ACTN4 T259I SNAP-FLAG-N1			
TEMPLATE	**VECTOR**	**OLIGO NAME**	**SEQUENCE 5’ TO 3’**
ACTN4 Flag-N1	pSNAP-Flag-N1	P1 fw	GAGGTCTATATAAGCAGAGCTGTTTAG
		P3 mut Nhe1 fw	CGTCAGATCCGATACCGCTACCGGACTC
		P2 rev Not1	GCCATGGCCTTGTCGTCATCGTCCTTG
		P4 rev ACTN4 T259I	GGACACGTAAATCATGATGGCCTTCTCATCTGGCCTCAG

ACTN4 K255E T259I SNAP-FLAG-N1			
TEMPLATE	**VECTOR**	**OLIGO NAME**	**SEQUENCE 5’ TO 3’**
ACTN4 Flag-N1	pSNAP-Flag-N1	P1 fw	GAGGTCTATATAAGCAGAGCTGTTTAG
		P3 mut Nhe1 fw	CGTCAGATCCGATACCGCTACCGGACTC
		P2 rev Not1	GCCATGGCCTTGTCGTCATCGTCCTTG
		P4 rev ACTN4 K255E T259I	GGACACGTAAATCATGATGGCCTCCTCATCTGGCCTCAG

Table 11.3 NES mutants

To allow for nuclear export, the NES sequence of HIV-Rev (LPPLERLTL) was inserted at the C-terminus of ACTN4. Constructs were ligated into pSNAP-Flag-N1 vector.

ACTN1 NES SNAP-FLAG-N1			
TEMPLATE	**VECTOR**	**OLIGO NAME**	**SEQUENCE 5' TO 3'**
ACTN1 SNAP-Flag-N1	pSNAP-Flag-N1	ACTN1 fw Xho1	ATATATCTCGAGATGGACCATTATGATTCTCAGCAAACCAAC
		ACTN1 NES rev EcoRI	TATATAGAATTCGTCCTCCTCCCAGCGTCAGCCTCTCCAGCGGCGGCAATCCTCCTCCGAGGTCACTCTCGCCGTACAGC

ACTN4 NES SNAP-FLAG-N1			
TEMPLATE	**VECTOR**	**OLIGO NAME**	**SEQUENCE 5' TO 3'**
ACTN4 SNAP-Flag-N1	pSNAP-Flag-N1	ACTN4 fw Xho1	ATATATCTCGAGATGGTGGACTACCACGCGGCGAACCAGTC
		ACTN4 NES rev EcoRI	TATATAGAATTCGTCCTCCTCCCAGCGTCAGCCTCTCCAGCGGCGGCAATCCTCCTCCCAGGTCGCTCTCGCCATACAAG

Table 11.4 Inducible constructs for lentiviral transduction

To create inducible lentiviral constructs, mutants were first subcloned into pEntr11. The constructs were recombined into pInducer20 Puro using the LR Clonase™, following manufacturer's instructions. Briefly, 1 µl of pInducer20 (100 ng/µl) was incubated with 5 µl pEntr11 construct (50 ng/µl), 2 µl LR Clonase™, 2 µl TE for 2–4 h at RT. 1 µl proteinase K was added, followed by transformation into competent cells.

pENTR11 ACTN4 SNAP-FLAG			
TEMPLATE	**VECTOR**	**OLIGO NAME**	**SEQUENCE 5' TO 3'**
ACTN4 SNAP-Flag-N1	pEntr11	ACTN4 fw Kpn1	ATATATGGTACCGCATGGTGGACTACCACGCGGCGAACC
		Flag rev Not1	ATATATCGGCCGCTACTTGTCGTCATCGTCCTTGTAATC

pENTR11 ACTN4 ΔCH1 SNAP-FLAG NLS			
TEMPLATE	**VECTOR**	**OLIGO NAME**	**SEQUENCE 5' TO 3'**
ACTN4 ΔCH1 SNAP-Flag-N1	pEntr11	ACTN4 fw Kpn1	ATATATGGTACCGCATGGTGGACTACCACGCGGCGAACC
		Flag rev Not1	ATATATCGGCCGCTACTTGTCGTCATCGTCCTTGTAATC
		NLS Flag SNAP rev Not 1 P1	ATATATGCGGCCGCTCAGCCCACCTTCCGCTTTTTCTTAGGCGGTCC
		NLS Flag SNAP rev P2	CTTCCGCTTTTTCTTAGGCGGTCCCTTATCGTCGTCATCCTTGTAATC
		NLS Flag SNAP rev P3	CGTCGTCATCCTTGTAATCAGACCCACCCAGCCCAGGCTTGCCCAGTCTGTG

By adding the SV40 large T antigen nuclear localization signal (NLS) PPKKKKRKV to the ACTN4 ΔCH1 mutant – following a published procedure – exclusive nuclear localization of this mutant was obtained [139].

Table 11.5 siRNA-resistant NES mutants

siRNA resistance was obtained by mutating 6 bases (the 3rd of each triplet; silent mutations) in the siRNA recognition site of the RNA. Hs siRNAs 1_7 and 4_7 were used as templates. Resulting codons were still coding for the same amino acids considering codon usage in humans. Constructs have been verified by sequencing (SeqLab) and functionality was proved by expression and simultaneous RNAi (Western Blot and staining).

Following constructs are also resistant to Mm siRNA 1_2 and 4_5 and Hs siRNA sequences 1_9 and 4_5.

pENTR11 ACTN1 WT SNAP-FLAG (SIRNA-RES)			
TEMPLATE	**VECTOR**	**OLIGO NAME**	**SEQUENCE 5' TO 3'**
ACTN4 SNAP-Flag-N1	pEntr11	ACTN1 fw Kpn1	ATATATGGTACCGCATGGACCATTATGATTCTCAGCAAACC
		ACTN1 si1.7 mut fw	CTACGGGAAGCTGCGGAAAGACGACCCTCTGACTAACCTGAATACGGCTTTTG
		ACTN1 si1.7 mut rev	CAAAAGCCGTATTCAGGTTAGTCAGAGGGTCGTCTTTCCGCAGCTTCCCGTAG
		Flag rev Not1	ATATATCGGCCGCTACTTGTCGTCATCGTCCTTGTAATC

pENTR11 ACTN4 NES SNAP-FLAG (SIRNA-RES)			
TEMPLATE	**VECTOR**	**OLIGO NAME**	**SEQUENCE 5’ TO 3’**
ACTN4 SNAP-Flag-N1	pEntr11	ACTN4 fw Kpn1	ATATATGGTACCGCATGGTGGACTACCACGCGGCGAACC
		ACTN4 si4.7 mut fw	GCCATGGAGGACCTCCAAGATATGTTTATTGTGCACACCATCGAGGAGATTG
		ACTN4 si4.7 mut rev	CAATCTCCTCGATGGTGTGCACAATAAACATATCTTGGAGGTCCTCCATGGC
		Flag rev Not1	ATATATCGGCCGCTACTTGTCGTCATCGTCCTTGTAATC

3.3.2 Agarose gel electrophoresis

DNA samples (PCR fragments, digested vectors, etc.) were mixed with 6X DNA loading dye and separated with agarose gels (1 % agarose in 1X TAE buffer containing 10 µg/µl ethidium bromide) under constant voltage using a DNA electrophoresis chamber. The separated DNA fragments were visualized using an INFINITY gel documentation system (peqLab). Seperated DNA bands were cut and extracted with NucleoSpin® gel and PCR clean-up kit.

3.3.3 RNA isolation from cells and qPCR

Cells were grown in a 3.5 cm cell culture dish to approximately 90 % confluency and lysed by addition of 1 ml TRIzol reagent. After 10 min of lysis at room temperature (RT), cells were scraped and transferred to 1,5 ml tubes. 200 µl chloroform was added to the cell lysate, followed by 15 s of rigorous vortexing and incubation on ice for 15 min. To separate the different phases, samples were centrifuged at 12,000 g for 15 min at 4 °C. The upper aqueous phase containing RNA, was carefully transferred to fresh tubes and mixed with 500 µl ice cold 100 % isopropanol to precipitate the RNA. After incubating on ice for 30 min, samples were centrifuged at 12,000 g for 20 min at 4 °C. The supernatant was removed carefully, and the RNA pellet was washed gently with 1 ml ice cold 75 %

ethanol and centrifuged at 7,500 g for 5 min at 4 °C. Ethanol was removed and after a further short centrifugation step, the remaining alcohol was carefully removed. The pellet was air-dried for 2–3 min at 50 °C and dissolved in 25 µl nuclease-free H_2O. Samples were heated to 55 °C for 5 min and frozen at -80 °C for at least 10 min.

For reverse transcription, RNA samples were diluted to 1 µg RNA per 10 µl. 1 µl Random hexamer primer was added. The mix was incubated for 5 min at 65 °C. A master mix containing 4 µl buffer RT, 2 µl dNTP, 1 µl ddH_2O (double deionized), 1 µl RevertAid reverse transcriptase and 1 µl RiboLock RNAse inhibitor. PCR reaction was performed using the manufacturer's protocol.

Table 12. PCR program generating cDNA from RNA

STEP	TEMPERATURE	TIME
1	25 °C	10 min
2	42 °C	60 min
3	70 °C	10 min
4	4 °C	∞

Obtained cDNA was quantified in qPCR using iQ™ SYBR® Green super mix consisting of 12.5 µl SYBR® Green, 9 µl dH_2O, 2.5 µl cDNA and 1 µl primer mix.

Table 13. qPCR program

STEP	TEMPERATURE	TIME	COMMENTS
Denaturation	95 °C	3 min	
Denaturation	95 °C	10 s	
Annealing	60 °C	30 s	40 cycles
Extension	72 °C	30 s	
Final extension	95 °C	2 min	
Melting curve	55–95 °C	10 s	

Table 14. qPCR primers

OLIGO NAME	SEQUENCE 5' TO 3'
GAPDH fw	CCCTTCATTGACCTCAACTA
GAPDH rev	CCAAAGTTGTCATGGATGAC
ACTN1 mm fw	GACCATTATGATTCCCAGCAGAC
ACTN1 mm rev	CGGAAGTCCTCTTCGATGTTCTC
ACTN4 mm fw	ATGGTGGACTACCACGCAG
ACTN4 mm rev	CAGCCTTCCGAAGATGAGAGT
ACTN1 hs fw1	CAGCGACATCGGTCATCTACATCGG
ACTN1 hs rev1	GTTACACATGGAGGCAGCTCAGGTG
ACTN4 hs fw1	CTGCTGCACTGTGGCTGCTGGAATC
ACTN4 hs rev1	GGCAACCGAGTGGTTCCAGTGGGC

Relative mRNA levels were calculated using the comparative ΔΔCT model [145] normalized to GAPDH cDNA, serving as house-keeping gene.

3.4 Immunofluorescence and microscopy

3.4.1 Fluorescence microscopy in fixed cells

Cells were grown on glass coverslips and fixed with 4 % formaldehyde in PBS for 10 min at room temperature (RT). After fixation, coverslips were washed 3x with PBS (5 min), followed by permeabilization with 0.3 % Triton X-100 in PBS for 10 min at RT. Permeabilized cells were blocked in 5 % FCS in PBS for 60 min at RT and subsequently incubated with respective antibodies (see Table 2). Primary antibody incubations were performed in 5 % FCS in PBS at 4 °C o/n. After 3 washing steps with PBS, cells were incubated with Alexa Fluor-labeled secondary antibodies in 5 % FCS in PBS for 60 min at RT: Optionally, DAPI and phalloidin-AF were diluted in 5 % FCS (concentrations indicated in table 2) and incubated for 10 min at RT. Coverslips were washed 3 times in PBS (5 min) and mounted on glass slides with fluorescent mounting medium (DAKO). Imaging was performed 2 h after mounting. Coverslips only incubated with the secondary antibody served as background control.

Images were generated at LSM700 or LSM800, respectively, confocal microscopes (Zeiss), each equipped with a 63X, 1.4 NA oil objective and the ZEN black (for LSM700) or Zen blue (for LSM800) software (Zeiss).

3.4.2 Analysis of immunofluorescence imaging

Images were processed with ZEN blue software and ImageJ/Fiji.

Brightness and contrast were optimized, and maximum intensity projections were generated from Z stack images, where indicated.

3.4.3 dSTORM sample preparation, staining and imaging

Cells were cultured in a grid-500 8 well ibidi at low density (1). With the 63X objective of a Zeiss LSM 700, cells in metaphase or anaphase of the cell cycle were imaged (snap shot, 2) and their positions were marked on a printed grid (3).

20–40 min later (4) (cells reached early G1), cells were prefixed with 1 % glutaraldehyde and 0,05 % Triton X-100 in cytoskeleton buffer (CSK) for 1 min at room temperature (RT). Prefixation solution was aspirated and cells were fixed with 3 % glutaraldehyde in CSK for 10 min at RT. After washing with CSK 3x for 5 min, $NaBH_4$ 10 mg/ml in H_2O was

incubated for 10 min (quenching). The slide was washed with CSK 5x for 5 min until all $NaBH_4$ was gone (5). Finally, CSK was aspirated, and cells were blocked with 100 µM L-lysine in ImageiT™ FX Signal Enhancer for 1 h at RT. After blocking, cells were incubated with a 1:50 dilution of phalloidin-AF647 for 96 h at 4 °C (6).

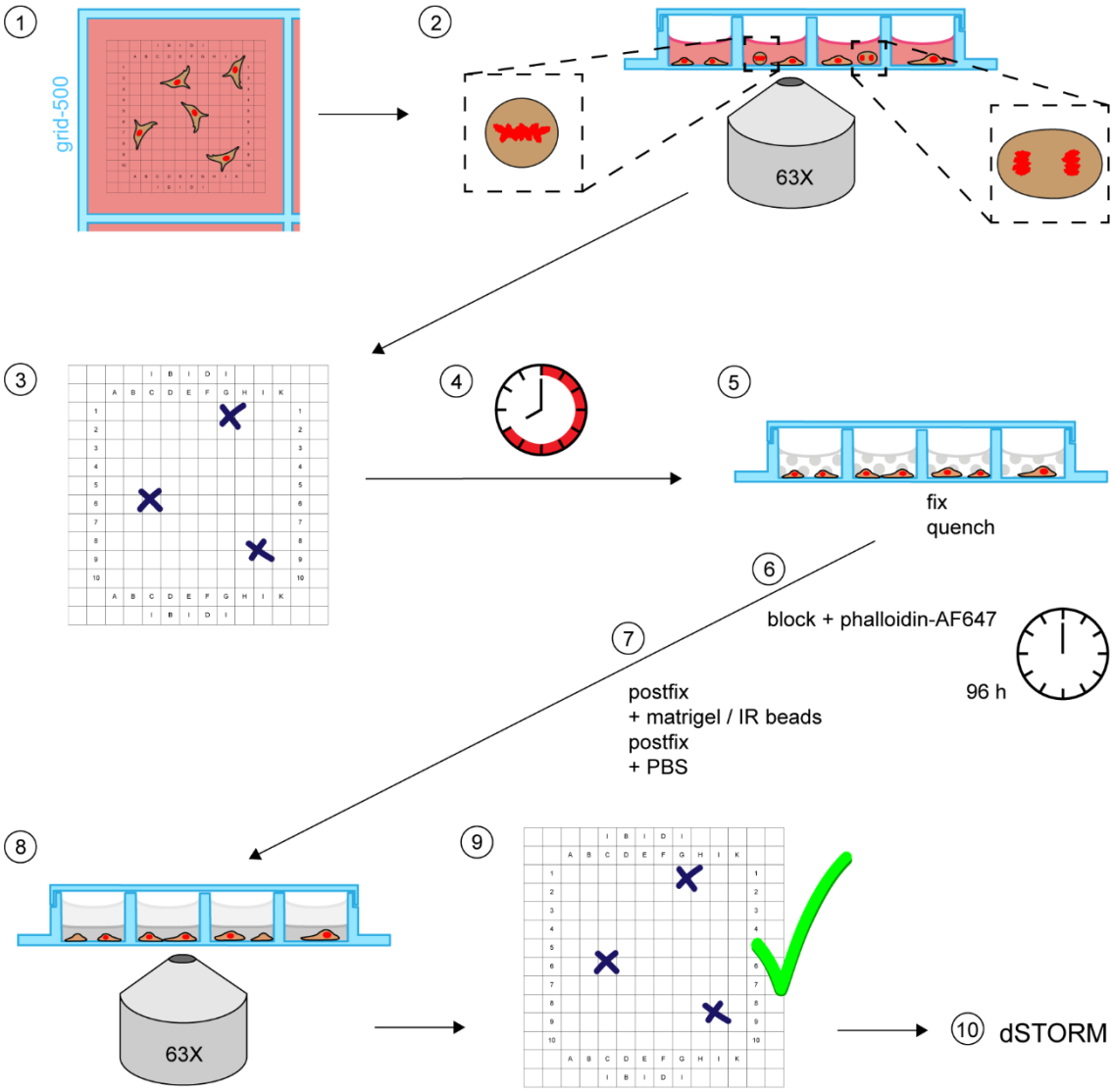

Figure 10. Workflow for dSTORM sample preparation.

Steps as indicated in the main text.

After staining, cells were postfixed with 4 % formaldehyde in PBS for 10 min. After washing twice for 5 min with 0.05 % Tween20 in PBS and once for 5 min with PBS, IR beads were diluted 1:50 in phenol red-free matrigel and added to the wells to cover the bottom (approximately 50 µl per well). Matrigel was solidified at 37 °C. After 1 h, matrigel

was postfixed with 4 % formaldehyde in PBS for 10 min at RT. After washing twice for 5 min with 0.05 % Tween20 in PBS and once for 5 min in PBS, 300 µl PBS was added to the wells to avoid drying (7). Imaging with the 63X objective (8) was performed to verify the marked positions (9), before dSTORM imaging (10).

SMLM experiments were conducted by Jannik Winkelmeier and David Virant (group of Ulrike Endesfelder, Max-Planck-Insitute for Terrestrial Microbiology, Marburg) on a customized automated inverted Ti-Eclipse microscope (Nikon). The imaging procedure was adapted from [183]. Briefly, the custom build microscope setup contained a CFI Apochromat TIRF 100X oil objective (NA 1.49, Nikon), appropriate dichroic and filters (ZET640/10 bandpass, ZET405/488/561/640 nm dichroic mirror, BrightLine HC 689/23 bandpass, all AHF Analysentechnik), 488 and 640 nm lasers (640 nm OBIS and 488 nm Sapphire, Coherent Inc.) and an emCCD camera iXON ULTRA 888 (Andor) with a pixel size of 129 nm for fluorescence detection. Both were modulated by an acousto optical tunable filter (AOTF, Gooch and Housego), Z-Focus was controlled by a commercial perfect focus system (Nikon). The setup was operated using a customized version of µManager [44]. Before each imaging experiment, the power of the 640 nm laser was adjusted to a final intensity of 1-2 kW^{-2} in the sample to ensure consistent conditions for different experimental days.

Before imaging, PBS was removed and dSTORM buffer was added: 100 mM mercaptoethylamine (MEA) with a glucose oxygen scavenger system [178]. The sample was illuminated in HILO (Highly Inclined and Laminated Optical sheet) [176] mode, specific cells were revisited from the marked positions on the ibidi grid and recorded at 20 Hz for 38,000-40,000 frames.

3.4.4 Analysis of dSTORM experiments

Fluorescent single molecule spots from the image acquisition were localized using ThunderSTORM [132]. The localization files were further processed using customized scripts written in Python programming language (Python Software Foundation, https://www.python.org) and were kindly provided by Dr. Bartosz Turkowyd (group of Ulrike Endesfelder) to correct for sample drift during image acquisition using the signals from the 100 nm diameter infrared beads in each sample and to filter out-of-focus signal (80 nm < PSF sigma < 200 nm, uncertainty < 35 nm). For each processed file, we measured the full width at half-maximum (FWHM) of infrared beads to ensure constant quality. Drift corrections with a resulting FWHM of 70 nm and larger were revisited.

Acquisitions that did not show improved correction, were excluded from further filament analyses. From the processed localization files, the final experimental localization precision was determined by calculating the NeNA precision value [12, 46]. Super resolution images were reconstructed with a pixel size of 10 nm using RapidSTORM 3.0 [156] and were processed with a Gaussian blur according to their individual NeNA localization precisions as indicated in the figure captions.

The number of localizations per nucleus was measured by selecting the nuclear region with the software swift (written in C++, Endesfelder group, unpublished) and normalized to the nuclear area. Filament widths were measured with a customized script for Fiji [156], where filaments were selected manually by a segmented line profile [12, 183].

To minimize errors due to selection and pixelation, selected areas were shifted 0.5 pixels (corresponding 5 nm) in all directions. From this, five measurements (ROIs) were attained which were further straightened to remove filament curvatures. After projection of the filament ROIs along their long axis, each profile was fitted by a Gaussian distribution. Resulting values show the full filament width at half-maximum value. Histogram bin size was obtained based on Freedman-Diaconis rule [54].

Number of filaments was determined with the script that has also been used for filament width measurements. The number of analyzed filaments was related to each daughter nucleus.

3.4.5 Live cell imaging and nuclear volume movies

Images were generated at LSM700 or LSM800, respectively, confocal microscopes (Zeiss), each equipped with a 63X, 1.4 NA oil objective and the ZEN black (for LSM700) or Zen blue (for LSM800) software (Zeiss).

Incubation chambers were heated to 37 °C and enriched with 5 % CO_2. Cells seeded into 8 well µ-slide ibidi chambers to a final confluency of about 30–40 % were imaged after having reached equilibrium.

To visualize nuclear actin, NIH3T3 cells expressing nAC mCherry were imaged with 10 Z stacks to perform maximum intensity projections. In general, cells were imaged every 30 s to every 5 min for an interval of 90 min from mitotic exit. For image processing, Zen blue software and FIJI were used.

For nuclear volume analysis, NIH3T3 cells stably expressing H2B mCherry were imaged every 5 min for 90 min, starting at mitotic exit. For each cell, 30 Z stacks were obtained to do an exact 3D reconstruction of the forming daughter nuclei.

3.4.6 Analysis of nuclear volume and chromatin densities

IMARIS software was used to generate 3D surfaces (from 30 Z stacks) based on nuclear-specific signal and to measure respective volumes over time.

Chromatin densities were calculated by dividing the sum of H2B mCherry fluorescence intensities by total nuclear volumes (intensity/µm^3) [12]. Each value was normalized to the value of corresponding timepoint 0.

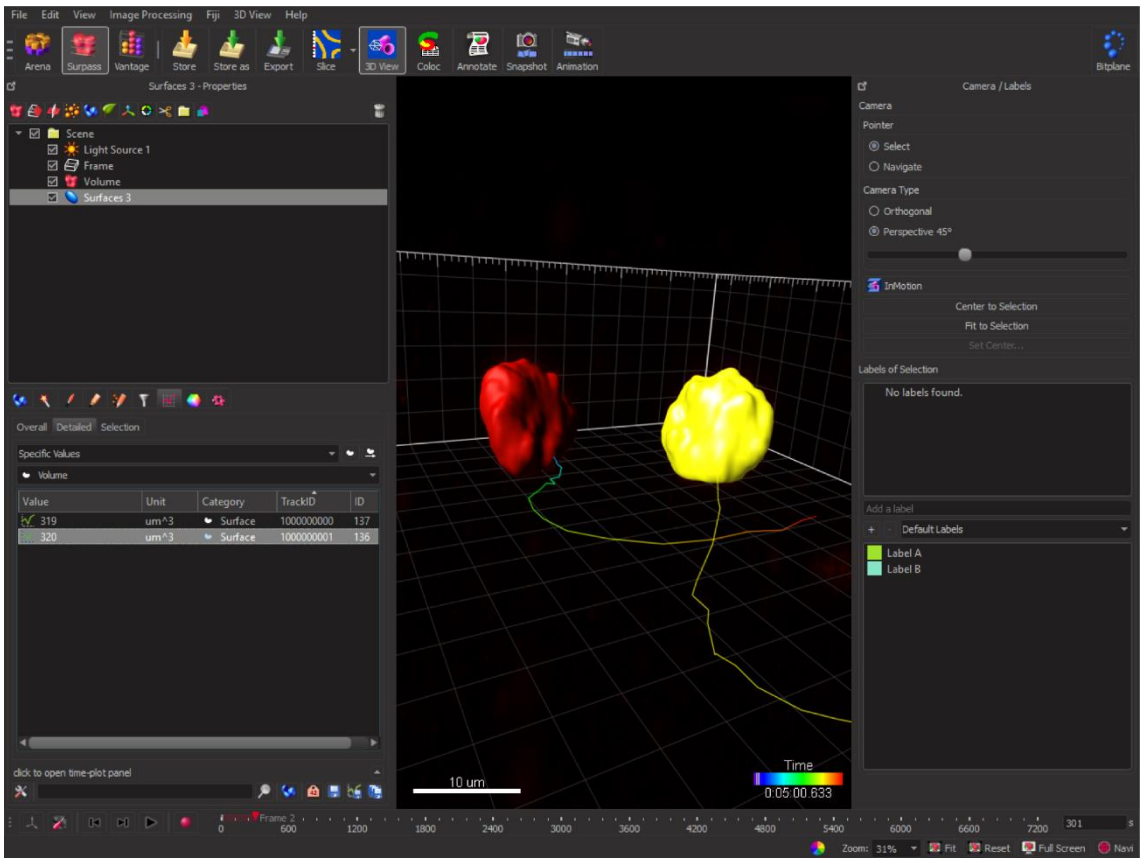

Figure 11. Screenshot of the Imaris software.

Creating surfaces from the H2B mCherry fluorescence signal enables measurement of parameters such as volume. Colored tracks indicate motion of the nuclei.

3.5 Biochemical methods

3.5.1 Determination of protein concentrations

Protein concentrations were obtained using the DC™ Protein Assay (Bio-Rad) following the manufacturer's instructions.

3.5.2 SDS-polyacrylamide electrophoresis (SDS-PAGE) and protein immunoblotting (Western Blot)

Depending on the assay, protein lysate was obtained either by scraping attached cells from 3.5 cm cell culture dishes with 200 µl 2X Laemmli sample buffer or by adding the appropriate amount of 4X Laemmli to protein samples lysed in P2, RIPA or actin-stabilization buffer (from preceding fractionation, Co-Immunoprecipitation or pulldown). Samples were boiled at 95 °C for 5 min and centrifuged for 1 min at maximum speed. Samples were stored at -20 °C or separated by SDS-PAGE using the Bio-Rad Mini-PROTEAN II Cell Gel System. If necessary, protein concentrations were determined with DC™ Protein Assay Kit to load equal amounts. Samples were loaded onto SDS-polyacrylamide gels with separating gels containing 8 %, 10 % or 15 % polyacrylamide, according to the size of the proteins. Proteins were separated using electrophoresis by applying a constant voltage of 80 V and 120 V, respectively.

After correct separation, proteins were transferred to 0.45 µm nitrocellulose membranes using the Bio-Rad Mini Trans-Blot® Electrophoretic Transfer Cell System. For transfer at 4 °C, constant 350 mA was applied for 30 or 90 min depending on protein size. After completed transfer, the membranes were blocked in blocking solution (5 % milk in TBST) for 1 h at RT. Membranes were washed once with TBST and supplied with antibody dilutions following instructions of the manufacturer (5 % milk in TBST or 5 % BSA in TBST). Primary antibodies were incubated o/n at 4 °C. After washing 3x with TBST, secondary antibodies conjugated with HRP (horseradish peroxidase) were diluted in 5 % milk in TBST and added to the membranes for 1 h at RT.

Membranes were washed 3x with TBST before detection. Self-made ECL reagent (equal volumes of S1 and S2) was applied to membranes and those were exposed to X-Ray films in the dark. Finally, films were developed using the X-Ray Processor.

3.5.3 Subcellular fractionation

The protocol for subcellular fractionations was adapted from Dr. Haicui Wang.

RPE-1 cells were grown in 10 cm (15 cm) cell culture plates to 50–90 % confluency and – if necessary – treated with doxycycline and RO3306. Cells were scraped on ice with 5 ml (10 ml) ice-cold PBS, following centrifugation at 800 g for 10 min. The supernatant was discarded. The pellet was resuspended in 1 ml Lysis buffer P1 and transferred to 1.5 ml tubes and kept on ice for 15 min. 50 µl of a 10 % solution of Triton X-100 in H_2O was added, followed by rigorous vortexing for 10 s. After centrifugation at 10,000 g for 10 min, the supernatant contained the cytoplasmic extract.

The pelleted nuclei were washed 3x with P1 and centrifuged at 4 °C and full speed for 5 min. The pellets were resuspended in 500–800 µl Extraction buffer P2 (800µl RIPA when proceeding with CoIP and 1 ml ASB when proceeding with phalloidin pulldown) and sonicated at medium rate for approximately 30 s. After tumbling for 1 h at 4 °C, samples were centrifuged for 10 min at maximum speed and 4 °C. The supernatant contained the nucleoplasmic fraction which could be used for further experiments.

Immunoblotting was performed with α-tubulin as cytoplasmic and histone H3 as nucleoplasmic marker to verify fractionation.

3.5.4 Co-Immunoprecipitation

This protocol was provided by Carsten Höß. 20 µl Flag M2 Affinity Gel (agarose beads conjugated with Flag M2 antibody) per reaction were diluted in and equilibrated with appropriate lysis buffer, in general RIPA.

75 µl of the nucleoplasmic fraction was stored at -20 °C to later serve as the input control. The rest (approximately 725 µl) was loaded onto the equilibrated beads and incubated for 90 min at 4 °C while tumbling. Following, samples were centrifuged for 30 s at 4 °C and maximum speed and washed 2x with ice-cold lysis buffer.

Finally, the beads were resuspended in 50 µl 2X Laemmli sample buffer, boiled at 95 °C for 5 min and conducted to Western Blot.

3.5.5 Phalloidin pulldown

Phalloidin pulldown was performed by Julian Knerr.

For every sample, 40 µl of Streptavidin magnetic Dynabeads were added to 1.5 ml tubes. After collecting the beads using the magnetic stand, the supernatant was removed, and beads were equilibrated with 1 ml Actin Stabilization Buffer (ASB). After gentle vortexing, beads were collected with the magnetic stand and ASB was removed. Beads were stored in ASB until usage to avoid drying. 10 µg Biotin-XX Phalloidin was added to 500 µl of the nuclear lysate and incubated for 2 h at 4 °C with constant rotation. The remaining 500 µl of the nuclear lysate were kept as negative control without adding Biotin-XX Phalloidin.

Right after removing ASB, nuclear lysates (with / without Biotin-XX Phalloidin) were added to the beads and incubated for 1 h at 4 °C while tumbling. Beads were collected using the magnetic stand. Supernatant was transferred to a new tube to later serve as input control (with / without Biotin-XX Phalloidin). After washing the beads 3x with 500 µl ASB, 100 µl 2X Laemmli was added. Beads were separated from the protein-containing supernatant which was boiled for 10 min at 95 °C and stored at -20 °C, following SDS-PAGE and immunoblotting.

3.5.6 WST-1 proliferation assay

NIH3T3 cells stably expressing pIND20 ACTN4 wt NLS SNAP Flag and pIND20 ACTN4 ΔCH1 NLS SNAP Flag, respectively were grown in 3.5 cm cell culture dishes. Expression was induced by adding 1 µg/ml doxycycline for 16 h and the SNAP tag was stained with SNAP-Cell 488 Oregon Green. After 24 h, cells were trypsinized and only well-expressing cells were sorted by FACS (Dr. Hartmann Raifer, group of Prof. Lohoff) to obtain 100 cells per well in a 96 well-plate.

At indicated timepoints (Fig 27), WST-1 reagent was diluted in growth medium and incubated for 1 h at 37 °C. Photometric analysis was performed at 450 nm at iMark Microplate Reader.

Values were normalized to timepoint 0 of the pIND20 ACTN4 wt NLS SNAP Flag cells.

3.5.7 MRTF/SRF luciferase reporter assay

MRTF/SRF luciferase reporter assays were performed by Dr. Dominique Brandt as described [27] using pGL3D.AFOS and pRL-TK reporter plasmids. MRTF/SRF activity experiments were conducted in HEK293T cells which were grown in 3.5 cm cell culture dishes. Cells were transfected with pGL3D.AFOS and pRL-TK reporter plasmids and with plasmids of interest. 4–5 h after transfection, cells were starved by replacing the growth medium by DMEM containing 0.25 % FCS 16–24 h prior analysis. 6 h before measurement, cells were stimulated with 20 % FCS in DMEM.

Dishes were briefly washed with PBS and 200 µl ice-cold passive lysis buffer was added to every 3.5 cm dish to lyse the cells, followed by scraping the cells off and transferring them into tubes. After incubation on ice for 20 min, samples were centrifuged at 20,000 g and 4 °C for 10 min. 5–20 µl of the supernatant was used to measure SRF luciferase activity. These assays were performed using the Dual-Luciferase® Reporter Assay System Kit according to the manufacturer's protocol.

The signal for the firefly and the renilla luciferases were measured sequentially by a Luminoskan™ Ascent Microplate Luminometer using the corresponding software.

For each sample, the firefly signal was normalized by the renilla values.

3.5.8 Flow Cytometry and synchronization procedure

Cells were grown in 3,5 cm cell culture dishes to 50 % confluency. Cell cycle was arrested by adding 10 µM of the CDK1 inhibitor RO3306 to the growth medium for 18 h. After synchronization was completed, RO3306 was washed out and cells released from cell cycle block: Cells were washed twice with PBS and once with growth medium. Growth medium was added, and cells were set to 37 °C and 5 % CO_2 for indicated timepoints. After appropriate trypsinization time, growth medium was added. After centrifuging at 1,000 g for 5 min at RT, supernatant was removed carefully. Cell pellet was resuspended in 100 µl PBS. 300 µl 100 % cold MeOH was added dropwise (to avoid clumping!) while vortexing the cell suspension at medium speed. Fixed cells were stored at -20 °C for at least 24 h before proceeding. Cells were pelleted by centrifuging for 10 min at 1,000 g and supernatant was discarded carefully. Cell pellets were washed twice with cold PBS and centrifuged at 1,000 g for 5 min. After removing the PBS, pellets were resuspended in 50 µl RNAse A (100 µg/ml in H_2O). 200 µl propidium iodide (50 µg/ml in H2O) were added and mixed. After staining overnight at 4 °C, the fixed and stained cells

were centrifuged for 10 min at 1,000 g. The supernatant was removed carefully and 150 µl PBS per sample was added. The mix was vortexed and measured at Guava EasyCyte flow cytometer. Data processing and analysis were done with corresponding software InCyte 2.7 using settings for cell cycle analysis based on published data [142].

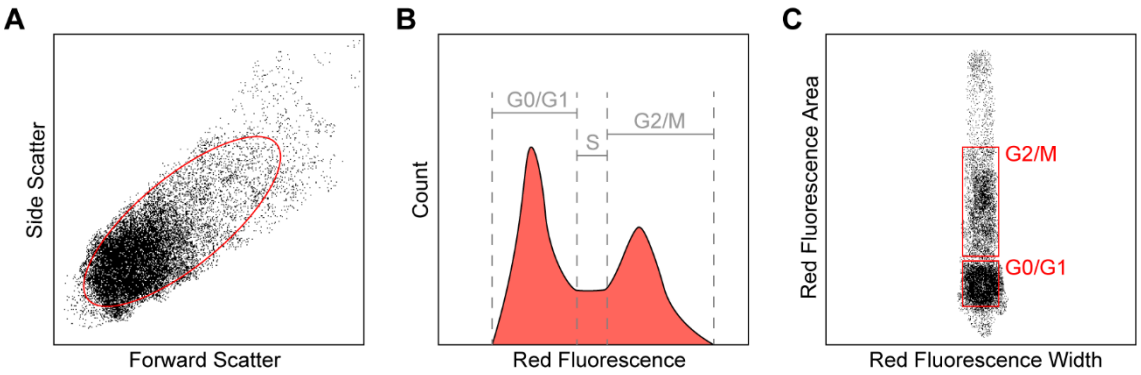

Figure 12. Analysis of the cell cycle with Flow Cytometry.

Schematic cell distribution and gating in InCyte software. ***(A)*** *shows Forward and Side Scatter in a cell-type specific pattern.* ***(B)*** *shows the red fluorescence intensity after PI staining correlated to the number of cells. The first peak with a low fluorescence intensity represents 2n chromosomal content (in G0/G1 phase), whereas the second peak includes 4n chromosomal content (in G2/M phase). The plateau between the peaks shows cells in S-phase.* ***(C)*** *shows the gating of the different cell populations. The upper represents cells with more fluorescence signal (G2/M phase) and the lower group contains cells with less fluorescence (G0/G1).*

CDK1 blockade was reported to arrest cells at the G2/M border [180, 181]. As previous experiments with other cell lines showed (HeLa, MCF10A; data not shown), the best timepoint to investigate early G1 cells is 2 h after a washout of the CDK1 inhibitor RO3306. In pilot experiments, this was confirmed for RPE-1 cells (Fig 13). 2 h after CDK1 block release, a high number of cells (approximately 40 %) is in G1 phase. This was also validated by imaging data (not shown).

In the following experiments with RPE-1 cells, this timepoint was used to get as many early G1 events as possible.

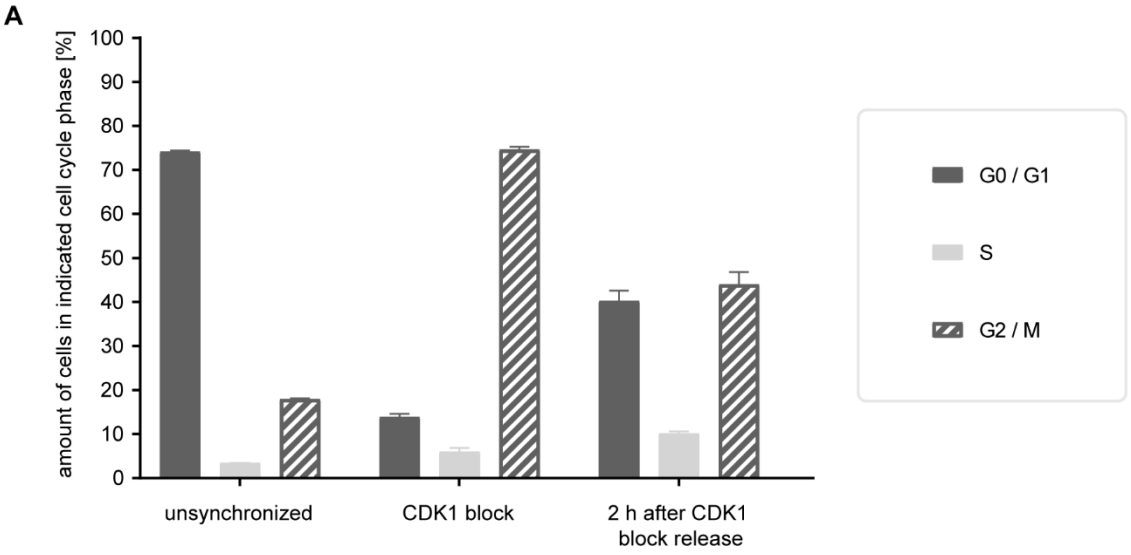

Figure 13. Synchronization conditions.

RPE-1 cells were synchronized with CDK1 inhibitor RO3306 (10 nM, 18 h) and compared to an unsynchronized cell population represented in the first 3 bars which show the normal distribution of cells in G0/G1, S or G2/M phase, respectively. The second condition shows an enrichment of cells in G2/M phase during CDK1 blockade. The last 3 bars represent cells 2h after washout of the CDK1 inhibitor.

3.6 Statistics

Statistical analysis was performed using GraphPad Prism 7. Data is presented as mean ± SEM. Statistical significance was evaluated with Two-Way ANOVA for multiple comparisons or unpaired two-tailed Student's *t* tests for comparison of two groups (as indicated in the figures).

Statistical significance is defined as $p \leq 0.05$: *, $p \leq 0.05$; **, $p \leq 0.01$; ***, $p \leq 0.001$; and ****, $p < 0.0001$.

4. Results

4.1 Localization of non-muscle ACTNs and interaction studies

4.1.1 Endogenous ACTN4 localizes at F-actin rich structures and to the nucleus

ACTN4 resides in actin-rich compartments, such as contractile stress fibers, cell-cell-contacts or adhesion complexes, and forms higher order structures by bundling actin filaments [66, 175]. However, its nuclear localization and function remain poorly understood [78, 105]. In a proteomic screen, ACTN4 was recently identified to interact with endogenous actin filaments extracted from early G1 cells using phalloidin as a bait [12]. We therefore investigated the role of ACTN4 in this cell cycle phase and initially immune-stained endogenous ACTN4 in mesenchymal and epithelial cells to determine its nucleocytoplasmic distribution.

Additional visualization of F-actin (phalloidin) revealed co-localization of ACTN4 with cytoplasmic stress fibers during interphase and displayed its existence in the cytokinetic ring or midbody in early G1 (Fig 14 A, B). Further immunofluorescence signals were detected in the cytoplasm and the nuclear compartment, as indicated by a DNA-specific counterstain (DAPI) (Fig. 14 A, B), thus evidencing nucleocytoplasmic shuttling of ACTN4.

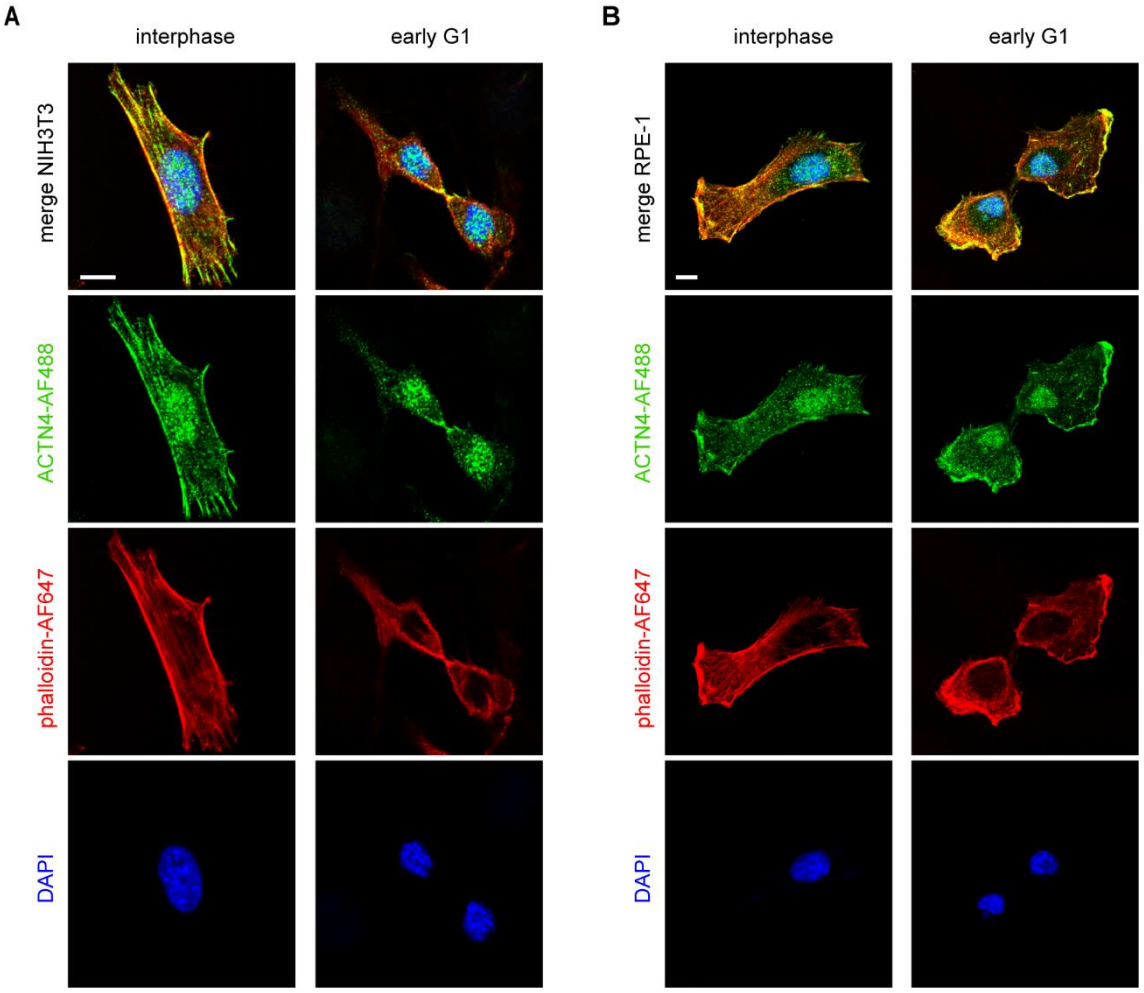

Figure 14. Endogenous localization of ACTN4 in NIH3T3 and RPE-1 cells.

Cells in either interphase or in early G1 were fixed and stained as indicated. ACTN4 was labelled by AF488 secondary antibody, F-actin was stained with Phalloidin-AF647 and DNA was stained with DAPI. Upper panel shows merge of all channels. ***(A)*** *Staining in NIH3T3 cells.* ***(B)*** *Staining in RPE-1 cells. Scale bars 10 µm.*

4.1.2 Flag-tagged ACTN1 and ACTN4 interact with endogenous actin

The other isoform ACTN1 is also present in non-muscle cells. Due to similarities in structure and actin-binding properties [52], we investigated a potential interaction of ACTN1 with nuclear actin. Co-Immunoprecipitations (CoIP's) were performed in HEK-293T cells transfected with Flag-tagged versions of either ACTN1 or ACTN4 (Fig 15 A). After subcellular fractionation (Fig 15 C), nuclear lysates served as inputs for CoIPs using anti-Flag beads. Precipitated samples were separated by SDS-PAGE, and subsequent immunoblotting with indicated antibodies identified that both, ACTN1 and ACTN4 interact with actin.

4.1.3 Endogenous ACTN4 interacts with endogenous nuclear F-actin

To confirm the physical interaction between nuclear ACTN4 and F-actin, we performed a phalloidin-based pulldown of nuclear F-actin at mitotic exit [12]. RPE-1 cells were synchronized with the Cdk1 inhibitor RO-3306 at the G2/M border [180, 181] and – 2 h after wash-out – subjected to subcellular fractionation (Fig 15 D). Nuclear lysates were incubated with biotinylated phalloidin following application of streptavidin-coated beads to facilitate enrichment of phalloidin-F-actin complexes. Omission of biotinylated phalloidin served as a specificity control. Samples were lysed and separated by SDS-PAGE. Immunoblotting against actin and endogenous ACTN4 validated the interaction (Fig 15 B).

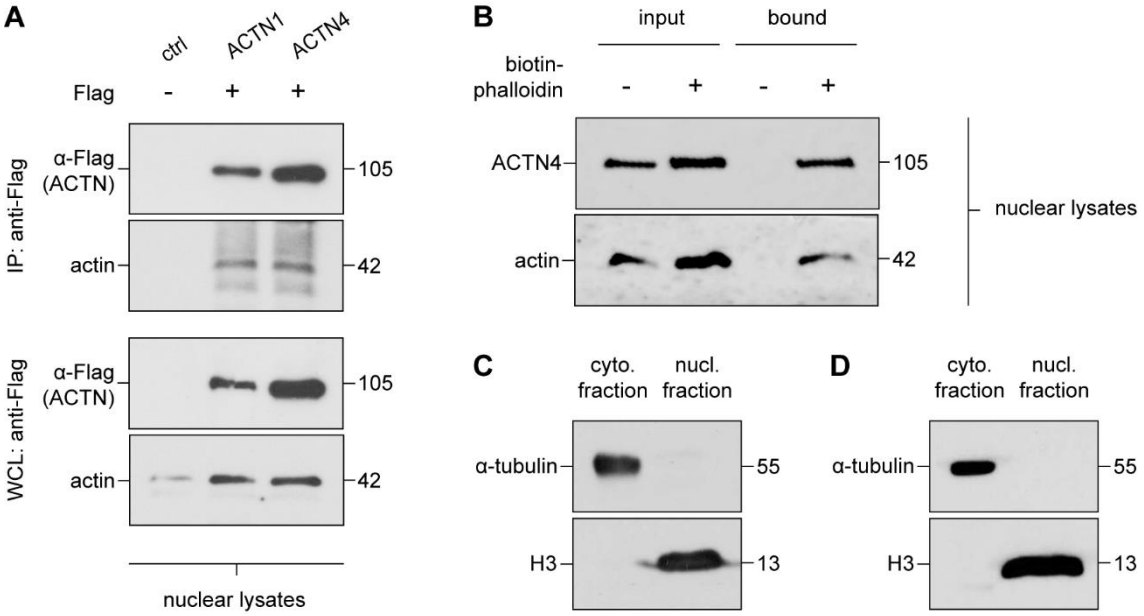

Figure 15. Interaction of ACTN4 with nuclear actin.

(A) *Co-Immunoprecipitation with either untransfected (ctrl) cells, ACTN1 Flag or ACTN4 Flag; detection of Flag (top) and actin (bottom) validate for Co-Immunoprecipitation of endogenous actin.* ***(B)*** *Phalloidin pulldown; detection of ACTN4 (upper part) and for actin (bottom part) validate F-actin pulldown and Co-Immunoprecipitation of ACTN4 from nuclear lysates.* ***(C)*** *Detection of histone H3 and α-tubulin confirm fractionation prior to CoIP.* ***(D)*** *Detection of histone H3 and α-tubulin confirm fractionation prior to F-actin pulldown.*

4.1.4 Overexpressed ACTN1 and ACTN4 show dynamic changes in subcellular localization

Next, live cell imaging of mouse fibroblasts co-expressing the F-actin probe F-Tractin mApple together with ACTN1 or ACTN4 constructs was used to analyze dynamic changes in subcellular localization of the actin-bundlers in postmitotic cells (Fig 16).

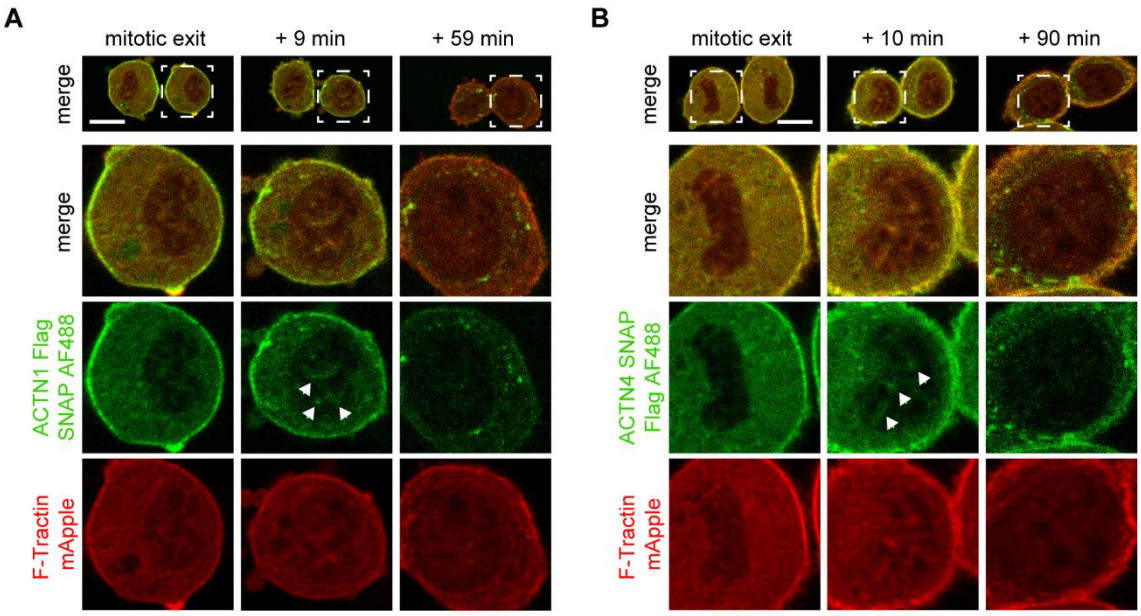

Figure 16. Live visualization of ACTN1 and ACTN4 overexpressing NIH3T3 cells.

Cells were co-transfected with F-Tractin mApple and indicated ACTN constructs and subjected to live cell imaging; upper panel shows stills of movies; lower panels are cropped images of indicated areas. Arrow heads indicate nuclear ACTN structures and propose co-localization of F-Tractin and ACTN. ***(A)*** *ACTN1 Flag SNAP.* ***(B)*** *ACTN4 SNAP Flag. Scale bar 10 µm.*

Consistent with recent observations [12], assembly of nuclear F-actin starts at mitotic exit. Filament structures are clearly visible in early G1 (9 or 10 min) and disappear with further cell cycle progression (59 or 90 min). Interestingly, both ACTN1 and ACTN4 concentrate in spots that overlap with F-Tractin structures, thus indicating that ACTN4 colocalizes with actin and suggesting F-actin bundling by ACTN1 and ACTN4 after mitotic exit.

4.2 Role of ACTNs in nuclear volume expansion after mitotic exit

4.2.1 Double knockdown of both ACTN isoforms results in decreased nuclear volume expansion

Nuclear F-actin assembly is required for correct nuclear volume expansion after mitotic exit. Since ACTNs bundle actin filaments, it was tempting to speculate that they might have impact on nuclear filament function [12]. As an initial loss of function approach, we performed double knockdown of both non-muscle isoforms using RNAi in NIH3T3 and RPE-1 cells expressing H2B mCherry to visualize nuclei (Fig 17). Full z-stacks of nuclei were imaged every 5 min for 90 min after mitotic exit. 3D reconstructed nuclear surfaces and corresponding volume measurements were obtained using Imaris.

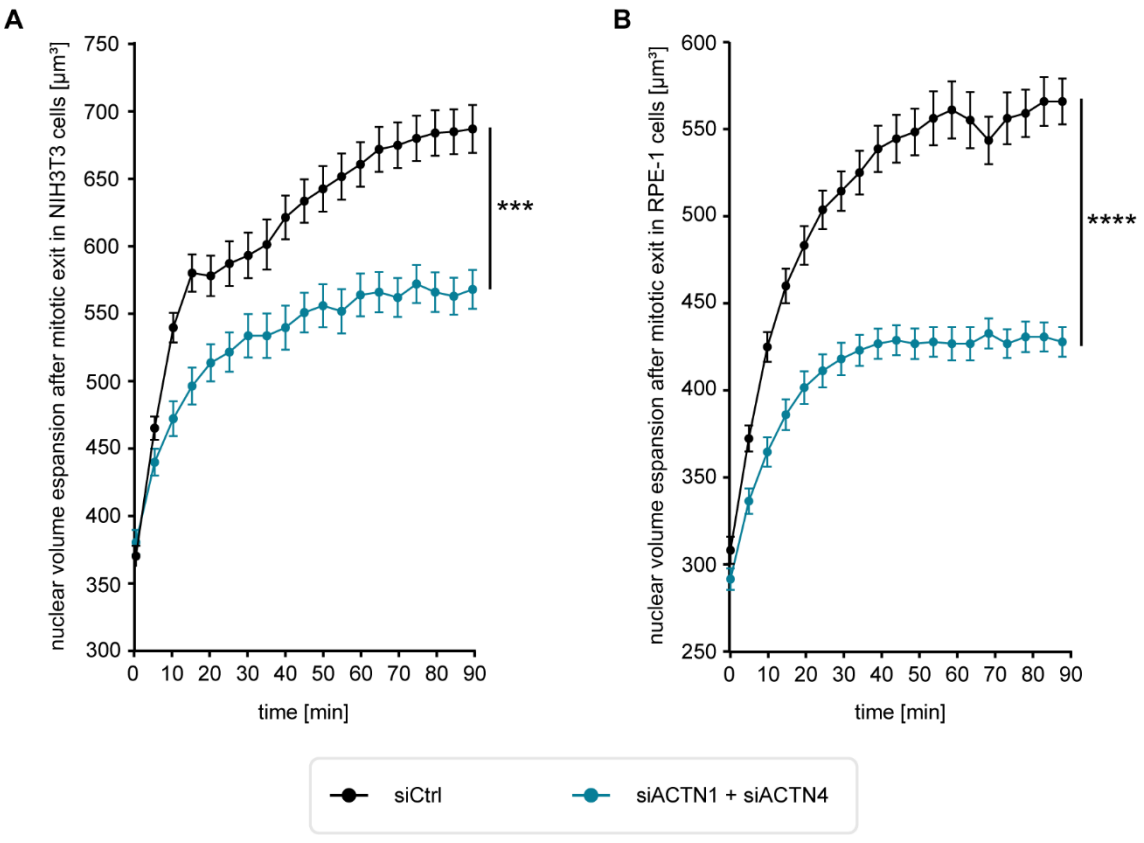

Figure 17. Loss of ACTNs impairs nuclear volume expansion after mitotic exit.

Cells stably expressing H2B mCherry were transfected with siCtrl or co-transfected with siACTN1 + siACTN4. H2B signal was imaged every 5 min for 90 min after mitotic exit. 30 Z-stacks were reconstructed to 3D images and corresponding volumes were calculated using Imaris software. ***(A)*** *NIH3T3; data shown*

as mean ± SEM: 22-27 nuclei(siCtrl) and 32-42 nuclei(siACTN1+4) from 3 independent experiments; p = 0.0007. ***(B)*** *RPE-1; data shown as mean ± SEM: 32-37 nuclei(siCtrl) and 31-39 nuclei(siACTN1+4) from 5 independent experiments; p < 0.0001. Statistics was done with unpaired two-tailed Student´s t-test.*

Interestingly, double knockdown of ACTN1 and ACTN4 in NIH3T3 resulted in an 18 % decrease in nuclear volume 90 min after mitotic exit (Fig 17 A) which was slightly more pronounced in RPE-1 cells showing a decrease of 25 % (Fig 17 B).

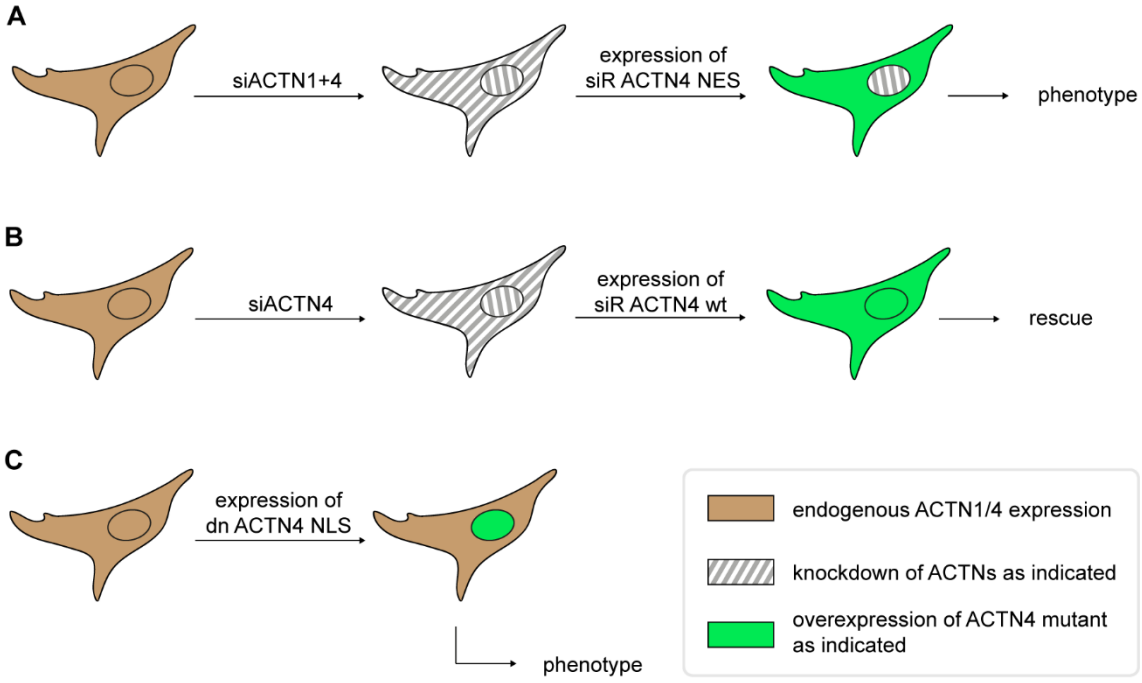

Figure 18. Design of experimental setups for detailed analysis of the phenotype.
ACTN mutants were cloned with SNAP-Flag to enable staining of live and fixed cells and to prevent altered kinetics due to fluorophore size. ***(A)*** *ACTN1 or ACTN4 were down regulated using RNAi. Overexpression of cytoplasmic ACTN4 NES with mutated siRNA recognition site (siR = siRNA-resistant ACTN4 NES) should result in cells lacking ACTNs in the nuclear compartment.* ***(B)*** *Cells were silenced for ACTN4 using RNAi. Reconstitution of ACTN4 wt (siR ACTN4 wt) should rescue bundling activity in the nucleus.* ***(C)*** *Cells with normal endogenous ACTN4 levels express dominant negative ACTN4 NLS to inhibit bundling specifically in the nucleus.*

4.2.2 Characterization of an siRNA-resistant cytoplasmic ACTN4 mutant

Knockdown of ACTNs could lead to strong cytoplasmic defects [53] that might conceal alterations in nuclear function of ACTNs. Our initial setup using RNAi (Fig 17) did not exclusively address functions of ACTNs exclusively in the nuclear compartment, therefore we decided to develop experimental setups that enabled to diminish potential effects arising from cytoplasmic depletion of ACTNs. These approaches further allowed identifying the isoform responsible for postmitotic nuclear volume expansion and specifying the requirement for its nuclear function (Fig 18). For this, we depleted ACTN1 or ACTN4 and expressed a mutant ACTN4 (siR ACTN4 NES) that is – by adding the NES from HIV-1 Rev [13, 50, 107] – exclusively located in the cytoplasm (Fig 19 A, B, C) and whose siRNA recognition site was mutated to obtain resistance towards siRNA (cf Table 11.5, Fig 19 D).

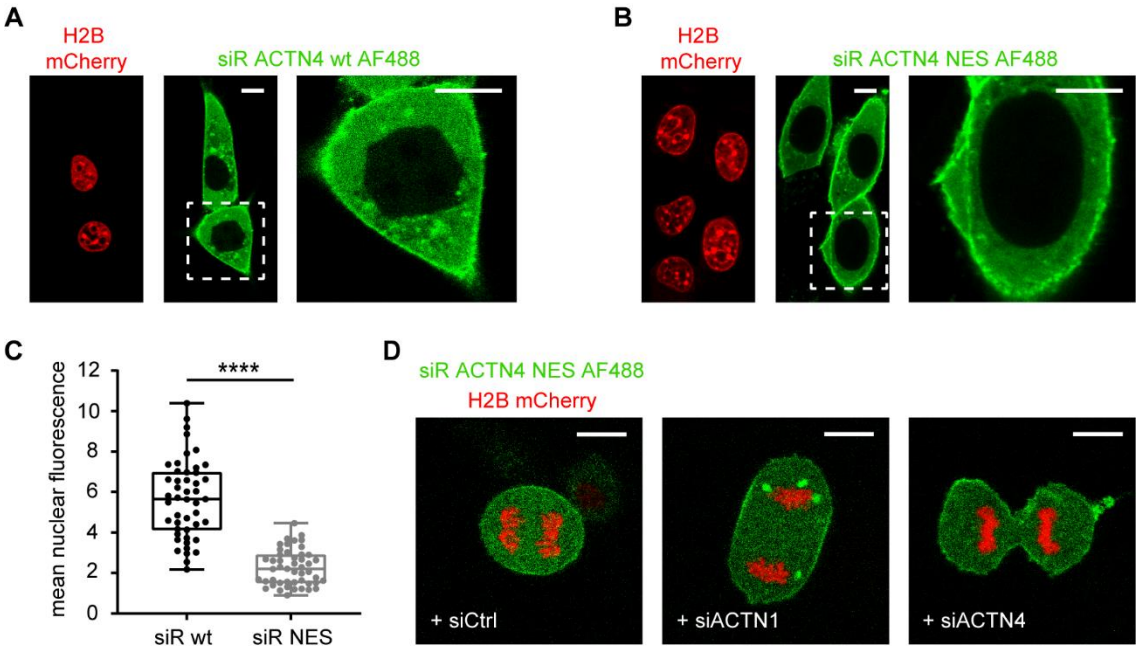

Figure 19. Characterization of the siRNA-resistant (siR) ACTN4 NES mutant.

NIH3T3 cells expressing H2B mCherry and indicated ACTN4 constructs stained with SNAP488 ***(A)*** *Localization of ACTN4 wt.* ***(B)*** *Localization of siR ACTN4 NES.* ***(C)*** *Quantification of mean fluorescence intensity of ACTN4 wt nuclei compared to siR ACTN4 NES nuclei; data shown as median ± 25-75 percentile: 47 nuclei(ACTN4 wt) and 48 nuclei(ACTN4 siR NES); $p < 0.0001$; statistics was done with unpaired two-tailed Student's t-test.* ***(D)*** *NIH3T3 cells stably expressing siR ACTN4 NES were transfected with either siCtrl, siACTN1 or siACTN4 and subjected imaging.*

Based on structural similarities between the ACTN isoforms [52], we assumed that re-expression of siR ACTN4 NES should rescue potential cytoplasmic defects due to a global ACTN1 knockdown. Accordingly, we transfected cells expressing siR ACTN4 NES with siACTN1 and siACTN4. We did not observe reduced expression of the mutant (Fig 19 D), thus confirming siRNA-resistance of siR ACTN4 NES.

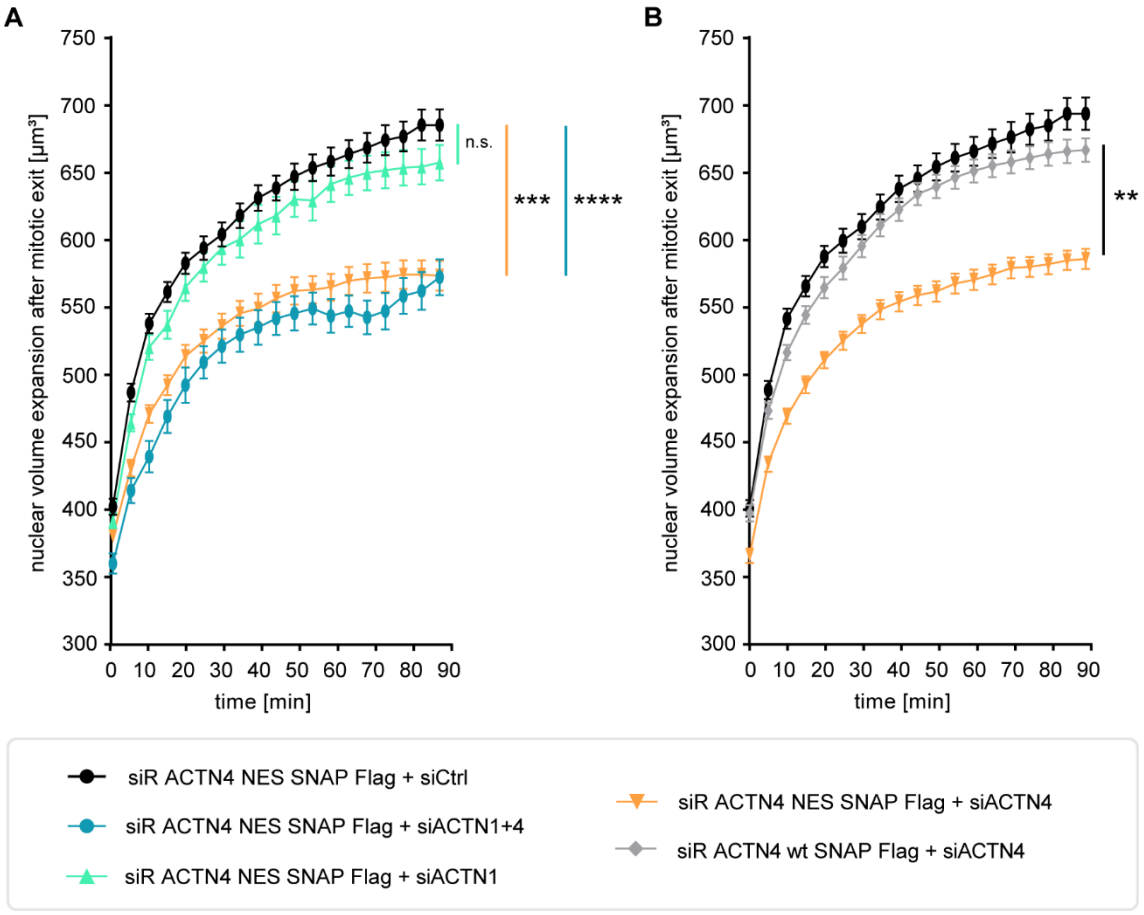

Figure 20. Nuclear volume expansion is impaired in ACTN4 knockdown cells expressing siR ACTN4 NES.

(A) *NIH3T3 cells stably expressing H2B mCherry and siR ACTN4 NES were transfected with indicated siRNAs; data shown as mean ± SEM: 63-71 nuclei(siCtrl), 37-41 nuclei(siACTN1+4), 52-58 nuclei(siACTN1) and 52-55 nuclei(siACTN4) from 5 independent experiments; statistics was done with Two Way ANOVA; p(siACTN4) = 0.0005**;** p(siACTN1+4) p < 0.0001.* ***(B)*** *NIH3T3 cells stably expressing H2B mCherry and indicated ACTN4 mutants were transfected with indicated siRNAs; data shown as mean ± SEM: 63-69 nuclei(ACTN4 wt + siACTN4), 63-71 nuclei(ACTN4 siR NES + siCtrl) and 54-58 nuclei(ACTN4 siR NES + siACTN4) from 3 independent experiments;; p = 0.0043. Statistics was done with unpaired two-tailed Student´s t-test.*

4.2.3 Nuclear ACTN4 is required for correct nuclear volume expansion after mitotic exit

Mouse fibroblasts expressing siR ACTN4 NES with ACTN4 knockdown as well as those with double knockdown for ACTN1 and ACTN4 displayed significantly reduced nuclear volume expansion after mitotic exit (Fig 20 A). Notably, knockdown of ACTN1 did not lead to significant reduction in nuclear volume expansion (Fig 20 A). From that, we can conclude that only nuclear ACTN4 but not ACTN1 is required for correct nuclear volume expansion after mitotic exit.

Furthermore, we reconstituted siR ACTN4 wt in ACTN4 knockdown cells and could observe that nuclear volume expansion was fully restored (Fig 20 B).

4.2.4 Characterization of a nuclear dominant negative ACTN4 mutant

To confirm our data from the knockdown and reconstitution experiments, we used an inhibitory approach by generating a dominant negative (dn) mutant of ACTN4 (lacking ability to bundle F-actin) fused to an NLS to inhibit F-actin bundling.

Since no previously characterized mutants were available, we considered creating a set ACTN4 deletion mutants that diminish F-actin bundling which either lack the ability to bind actin (ACTN4 ΔCH1 and ΔCH2) or to form functional dimers (ACTN4 ΔSR2 and ΔSR23). Calponin homology domains 1 and 2 (tandem) are responsible for actin-binding: CH1 alone can still bind actin, but attains lower affinity than the tandem CH domain, whereas CH2 alone was reported to be unable to bind actin [57, 164]. All four spectrin repeats (SR) are required to facilitate dimerization of two ACTN molecules [51].

In contrast to the other deletion mutants, ACTN4 ΔCH2 showed abnormal localization pattern and was therefore excluded from further investigation (Fig 21 B).

Since actin dynamics directly and efficiently promote SRF activity [13, 121], we used SRF reporter assay to assess the dominant negative properties of the generated deletion mutants. ACTN4 wt served as control, but showed no increased SRF activity compared to untransfected cells (Fig 21 C).

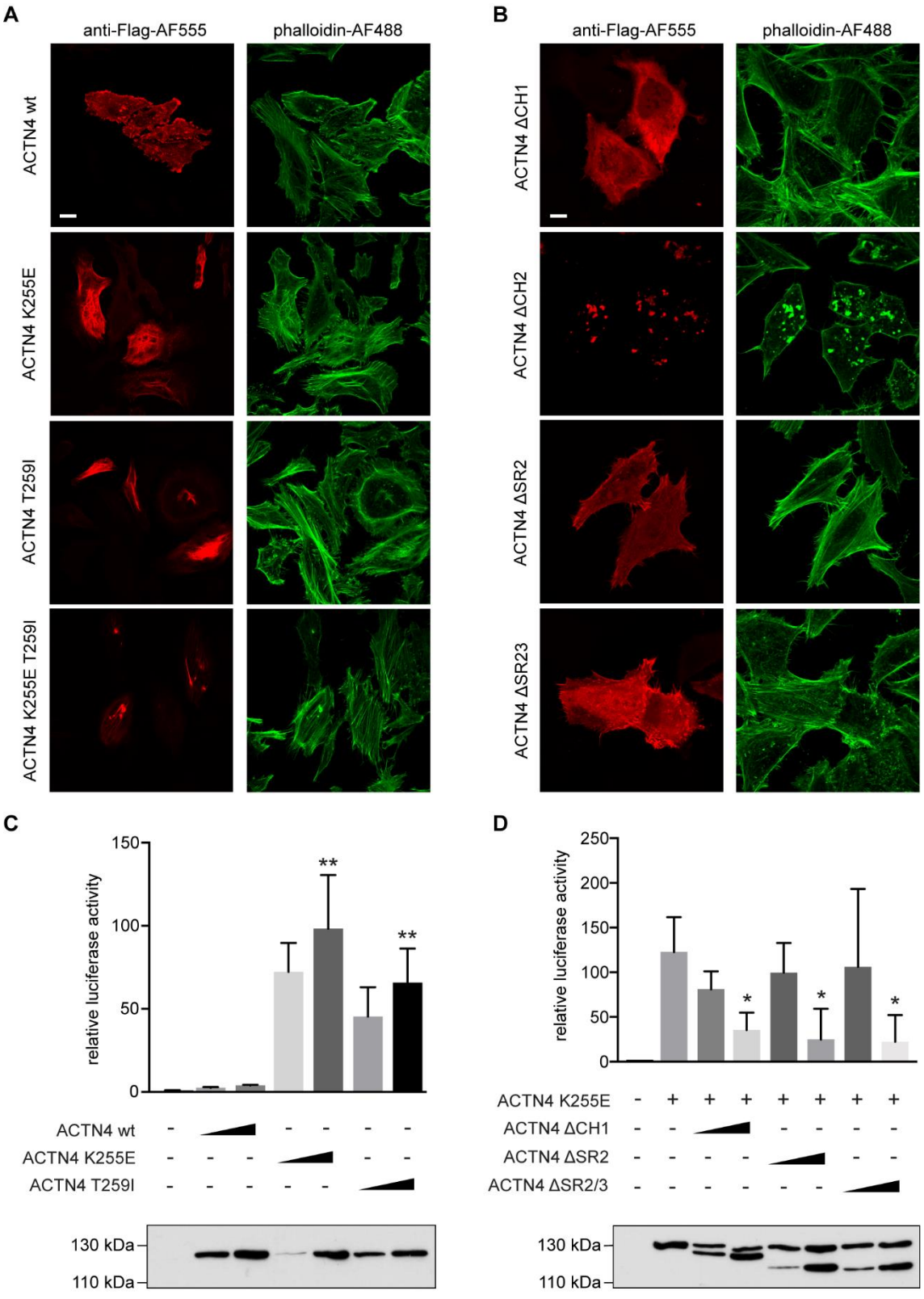

Figure 21. Characterization of constitutively active (ca) and dominant negative (dn) ACTN4 mutants. *NIH3T3 cells were fixed; ACTN4 constructs were stained with anti-Flag and F-actin with phalloidin**; s**cale bar 10 µm.* ***(A)***, ***(B)*** *Localization of indicated ACTN4 mutants.* ***(C)*** *SRF reporter gene assay for ACTN4 mutants with increased F-actin binding; concentrations(mutants) = 25 ng / 100 ng; data shown as mean ±*

SD; p(K255E) = 0.0072; p(T259I) = 0.0064; lower panel shows expression of transfected constructs, ***(D)*** *SRF reporter gene assay showed dominant negative effects of ACTN4 deletion mutants; indicated mutants were tested against constitutively active properties of ACTN4 K255E; concentration(K255E) = 100 ng; concentrations(dn mutants) = 100 ng / 300 ng; data shown as mean ± SD; p(ΔCH1) = 0.0252; p(ΔSR2) = 0.0307; p(ΔSR23) = 0.0237; bottom panel shows expression of transfected and double-transfected cells. Statistics was done with unpaired two-tailed Student's t-test.*

To increase SRF reporter activity, we cloned ACTN4 mutants with enhanced F-actin bundling that were reported to cause a subtype of the kidney disease focal segmental glomerulosclerosis (FSGS) [92, 192]. ACTN4 K255E and T259I resulted in increased luciferase activity (Fig 21 C), while the version containing both point mutations was excluded due to an altered localization pattern (Fig 21 A).

Based on the increased reporter activity by ACTN4 K255E, we proceeded with this mutant serving as a baseline control. Notably, co-transfection with ACTN4 ΔCH1, ΔSR2 or ΔSR23 revealed dominant negative characteristics for all three derivatives. However, we chose ACTN4 ΔCH1 for further experiments; besides better viability, this mutant retained the ability to dimerize via its spectrin-repeats and could potentially form dimers with endogenous ACTN1 and ACTN4 and thus, represented a promising candidate for a dominant negative ACTN4 (dn ACTN4).

4.2.5 Dominant negative ACTN4 NLS shows impaired nuclear volume expansion after mitotic exit

After modifying the dominant negative ACTN4 mutant by adding the SV40 large antigen nuclear localization sequence (NLS) [91, 139], it showed predominant nuclear localization (Fig 22 B).

Notably, NIH3T3 expressing dn ACTN4 NLS showed significantly reduced nuclear volume expansion after mitotic exit compared to ACTN4 wt cells (Fig 22 C) and to a similar extent as the double knockdown of ACTN1 and ACTN4, thus confirming our previous findings. In later stages of the cell cycle, we further found equal nuclear volumes 8 h after mitotic exit, suggesting an assimilation mechanism (Fig 22 D).

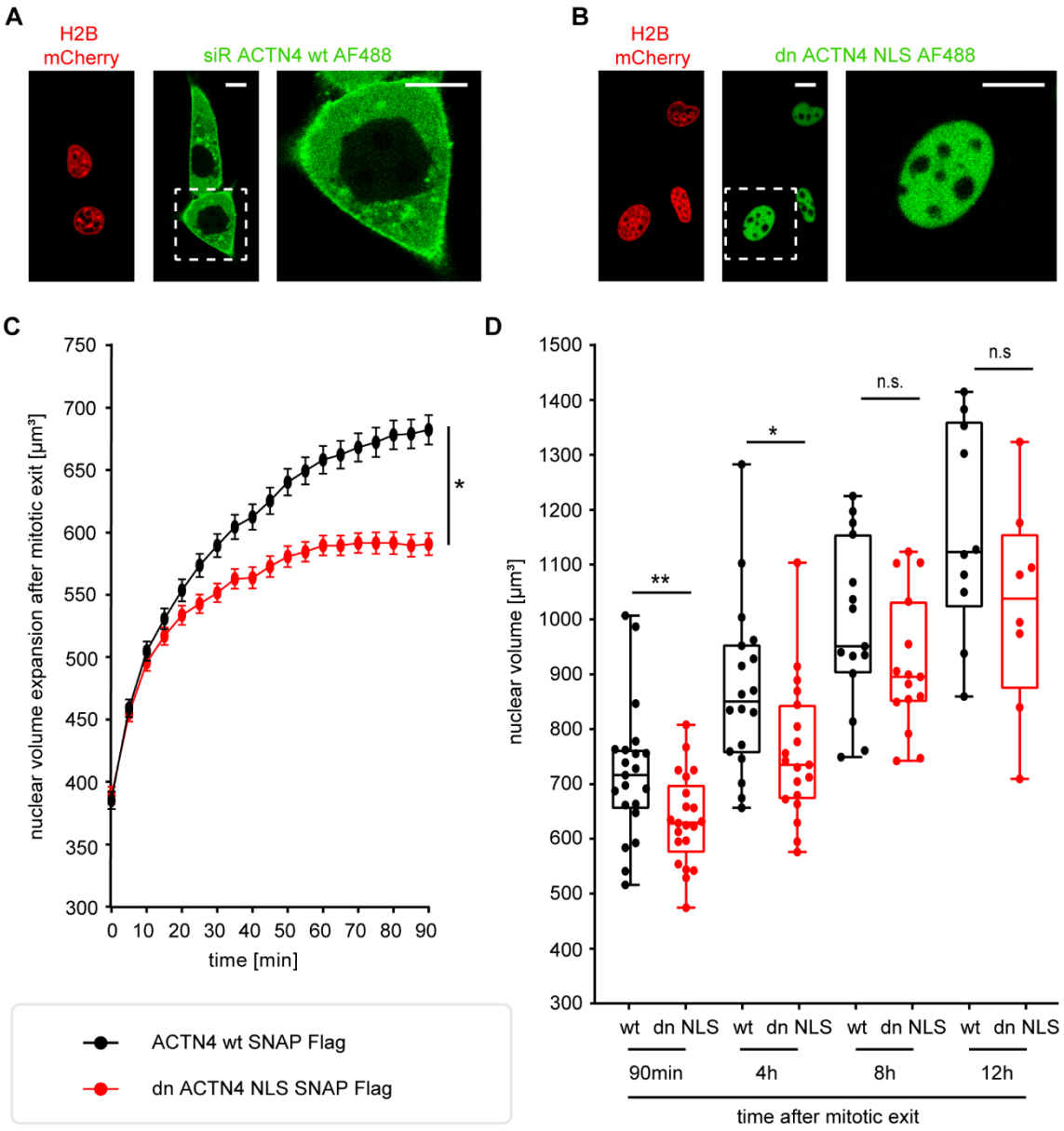

Figure 22. Nuclear volume expansion in dn ACTN4 NLS cells.

NIH3T3 cells expressing H2B mCherry and indicated ACTN4 mutant were staind with SNAP Oregon Green and subjected confocal imaging ***(A)*** *Localization of ACTN4 wt.* ***(B)*** *Localization of dominant negative (dn) ACTN4 NLS.* ***(C)*** *Nuclear volume expansion with dn ACTN4 NLS compared to ACTN4 wt construct; data shown as mean ± SEM: 56-62 nuclei(ACTN4 wt) and 51-57 nuclei(dn ACTN4 NLS) from 4 independent experiments; p = 0.0350.* ***(D)*** *Nuclear volume with dn ACTN4 NLS compared to ACTN4 wt construct; timepoints after mitotic exit: 90 min, 4 h, 8 h, 12 h; data shown as median ± 25-75 percentile: 10-21 nuclei(ACTN4 wt) and 8-21 nuclei(dn ACTN4 NLS) from 3 independent experiments; p(90min) = 0.0096; p(4h) = 0.0174. Statistics was done with unpaired two-tailed Student's t-test.*

4.3 F-actin bundling studies in postmitotic nuclei lacking functional ACTN4

4.3.1 Knockdown of ACTN4 results in lower number of bundled actin filaments in postmitotic daughter nuclei

Our research group previously showed that daughter nuclei form nuclear actin filament bundles in early G1 up to 90 min after mitotic exit [12]. We further demonstrated that correct nuclear volume expansion after mitotic exit requires F-actin and that this process is dependent on a polymerization-competent G-actin pool. Implicating a potential additional role for actin-bundling factors.

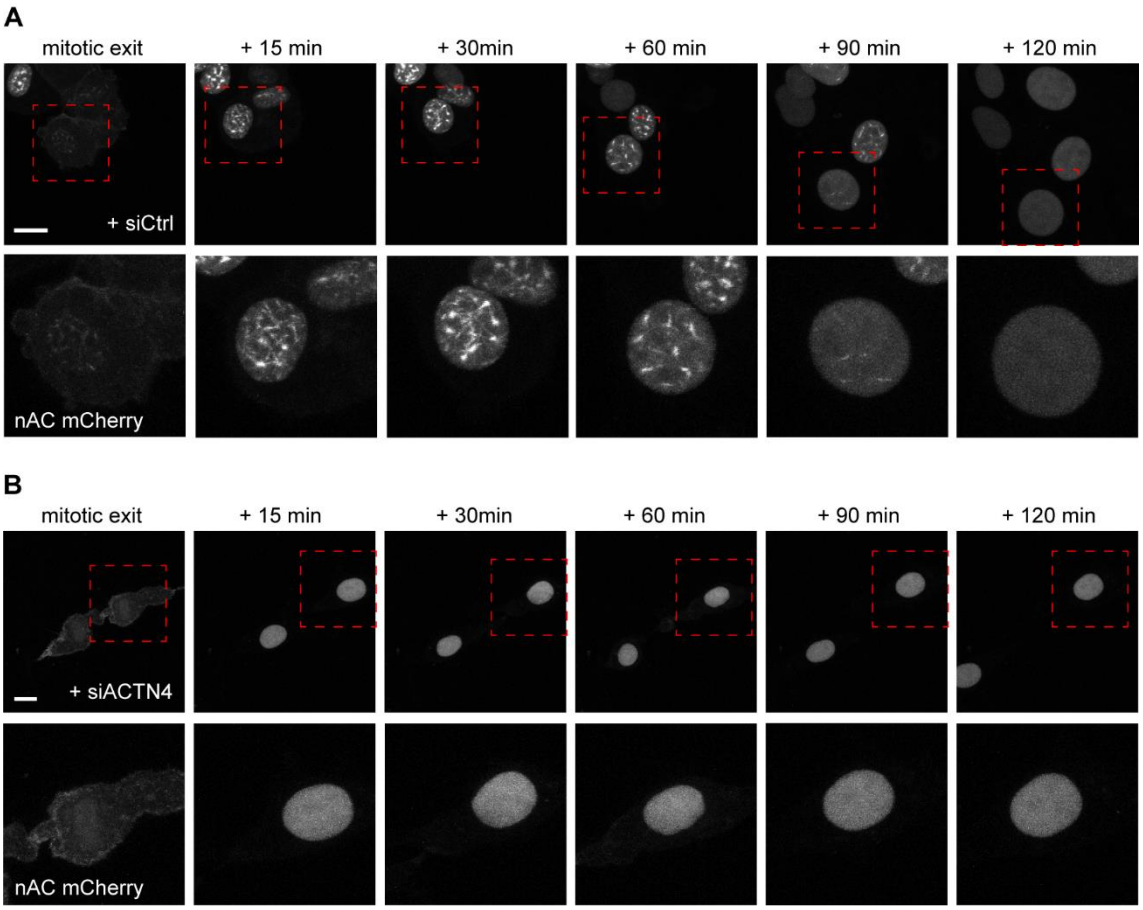

Figure 23. ACTN4 knockdown leads to decreased F-actin bundling after mitotic exit.
*NIH3T3 cells stably expressing nAC mCherry were transfected with indicated siRNAs and imaged for 120 min. Upper panel shows stills of a movie; maximum intensity projections of 30 Z-stacks**;** lower panel shows zoom images of indicated areas (red boxes); scale bars 10 µm.* ***(A)*** *siCtrl.* ***(B)*** *siACTN4.*

Initial tests in NIH3T3 expressing nAC mCherry revealed that knockdown of ACTN4 (Fig 23 B) abolished F-actin bundling, whereas control cells (Fig 23 A) exhibited clearly visible F-actin structures that disappeared 90 min after mitotic exit. Of note, unbundled (single) actin filaments cannot be resolved in our confocal microscope setup.

4.3.2 Super resolution microscopy (dSTORM) reveals impaired F-actin bundling in dominant negative ACTN4 NLS cells

Next, we aimed for a quantitative analysis that was challenging for two reasons: First, a single actin filament measures 5-7 nm in diameter [65]. According to the limited imaging resolution in fluorescence microscopy defined by the Abbe law and due to the diffraction of light, we cannot distinguish two points closer than 200 nm [83]. Second, accurate quantification of nAC mCherry signal is not possible because the actin chromobody is labelling both, G-actin und F-actin. Hence, the background signal was too high to analyze actual numbers of filament bundles.

Therefore, we performed phalloidin staining and subsequent super resolution imaging, thus detecting exclusively F-actin, disregarding existing monomers. We used NIH3T3 cells expressing dn ACTN4 NLS and performed SNAP staining prior to phalloidin staining to restrict analysis to successfully transduced cells. Nuclei of unstimulated interphase cells should not show any pronounced F-actin structures. Hence, we used ACTN4 wt SNAP Flag expressing NIH3T3 interphase cells to determine the background signal that could be caused either by non-specifically bound phalloidin-AF647 molecules or by short F-actin polymers. Early G1 nuclei of the same cell line served as positive control exhibiting postmitotic actin filaments (Fig 24).

Nuclei of ACTN4 wt interphase cells as well as those of dn ACTN4 NLS cells exhibited fewer phalloidin-AF647 localizations. Accordingly, they did not show any pronounced actin filament structures. In contrast, nuclei of ACTN4 wt cells fixed in early G1 displayed significantly more fluorophore (phalloidin-AF647) localizations per nuclear area and a significantly higher actin filament number (Fig 24, cf Appendix: Collection of dSTORM images).

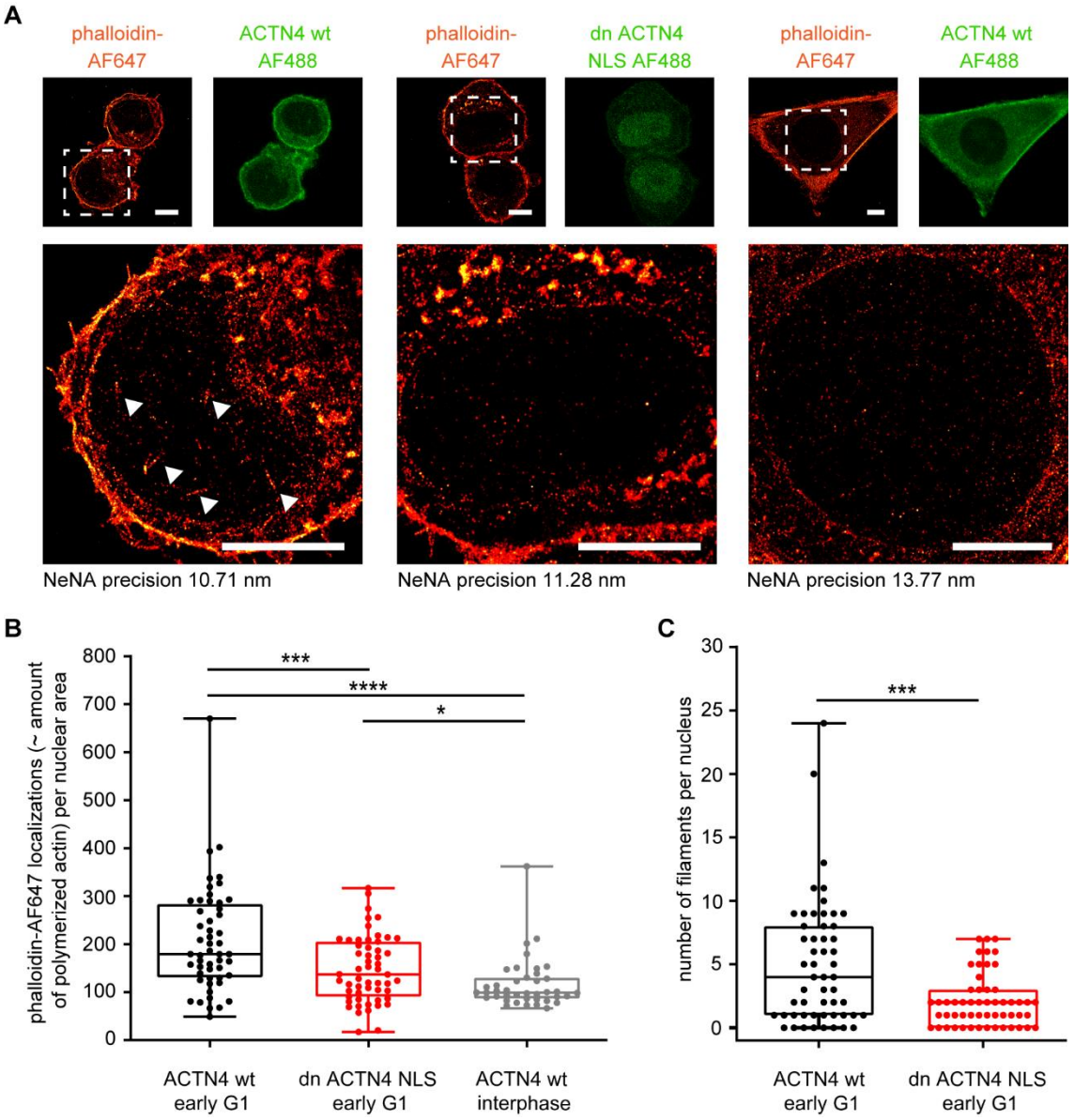

Figure 24. Dn ACTN4 NLS nuclei represent fewer Phallodin-AF647 localizations and actin filament numbers.

Live imaging in NIH3T3 cells expressing ACTN4 constructs as indicated were stained with SNAP Oregon Green and provided positions of mitotic cells. After fixation, cells were stained with phalloidin-AF647 (exact procedure cf 3.4.3 and 3.4.4). ***(A)*** *Upper panel shows expression of ACTN4 mutants (green, confocal image) and phalloidin-AF647 staining in the same cells (orange, dSTORM image); lower panel represents zoom of the indicated areas (white boxes); arrowheads indicate actin filaments; scale bars 5 µm.* ***(B)*** *Phalloidin-AF647 localizations in the same cells; data shown as median ± 25-75 percentile: 52 nuclei(ACTN4 wt early G1), 55 nuclei(dn ACTN4 NLS early G1) and 40 nuclei(ACTN4 wt interphase) from 5 independent experiments: *, p = 0.0196; ***, p = 0.0009; ****, p < 0.0001.* ***(C)*** *number of filaments in the same cells; data shown as median ± 25-75 percentile: 54 nuclei(ACTN4 wt early G1) and 55 nuclei(dn ACTN4 NLS early G1) from 5 independent experiments: p = 0.0001. Statistics was done with unpaired two-tailed Student's t-test.*

Notably, we could observe fewer filament structures in dn ACTN4 NLS nuclei, while those filaments displayed significantly decreased widths as compared to ACTN4 wt cells (Fig 25). We determined the resolution of our dSTORM images from measuring the experimental localization precision by NeNA [46] which ranged from 10-15 nm in all images. Therefore, our resolution was ca. 35 nm (2.35*NeNA). Adding the actual width of an actin filament of 5-7 nm [65] and the size of a phalloidin-AF647 molecule of about 2-3 nm [177], we expected single filaments to appear at widths of around 45 nm in our images. Hence, nuclei of dn ACTN4 NLS cells mainly exhibited single actin filaments, whereas the wt version also showed significant amounts of higher order bundles (Fig 25).

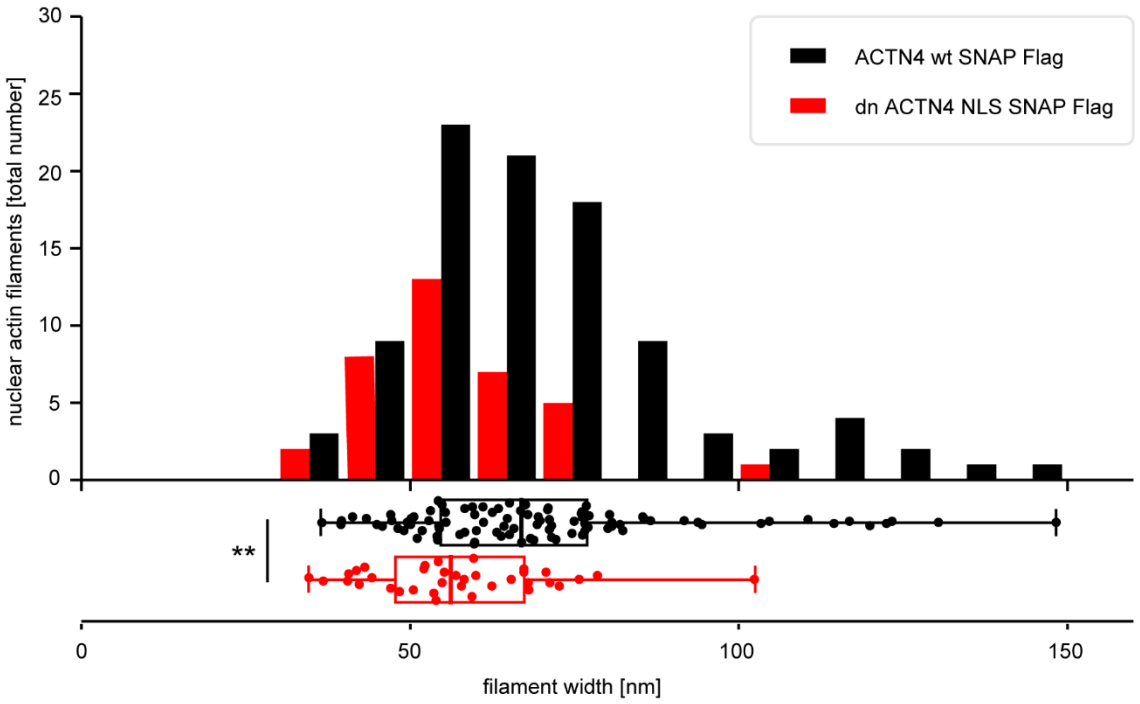

Figure 25. Dn ACTN4 NLS impacts on actin filament widths.

Live imaging in NIH3T3 cells expressing ACTN4 constructs as indicated were stained with SNAP Oregon Green and provided positions of mitotic cells. After fixation, cells were stained with phalloidin-AF647 (exact procedure cf 3.4.3 and 3.4.4). Filament widths were analyzed in drift-corrected images (cf 3.4.4); bar graphs represent fractions of filament sizes according to equal bin sizes for ACTN4 wt and dn ACTN4 NLS cells; lower panel displays all measured data and their distribution; data shown as median ± 25-75 percentile: 96 filaments(ACTN4 wt early G1) and 36 filaments(dn ACTN4 NLS early G1) from 5 independent experiments: p = 0.0013. Statistics was done with unpaired two-tailed Student's t-test.

4.4 Impact of impaired ACTN function on other cellular processes

4.4.1 ACTN4 is required for correct chromatin decondensation in early G1

When daughter nuclei re-assemble, chromatin structures change from condensed mitotic state to decondensed structures enabling transcription and other processes [168].

We could detect significantly higher chromatin densities after mittic exit in siR ACTN4 NES expressing NIH3T3 cells transfected with siACTN4 in comparison with siCtrl (Fig 26), indicating a requirement of ACTN4 in chromatin decompaction in early G1.

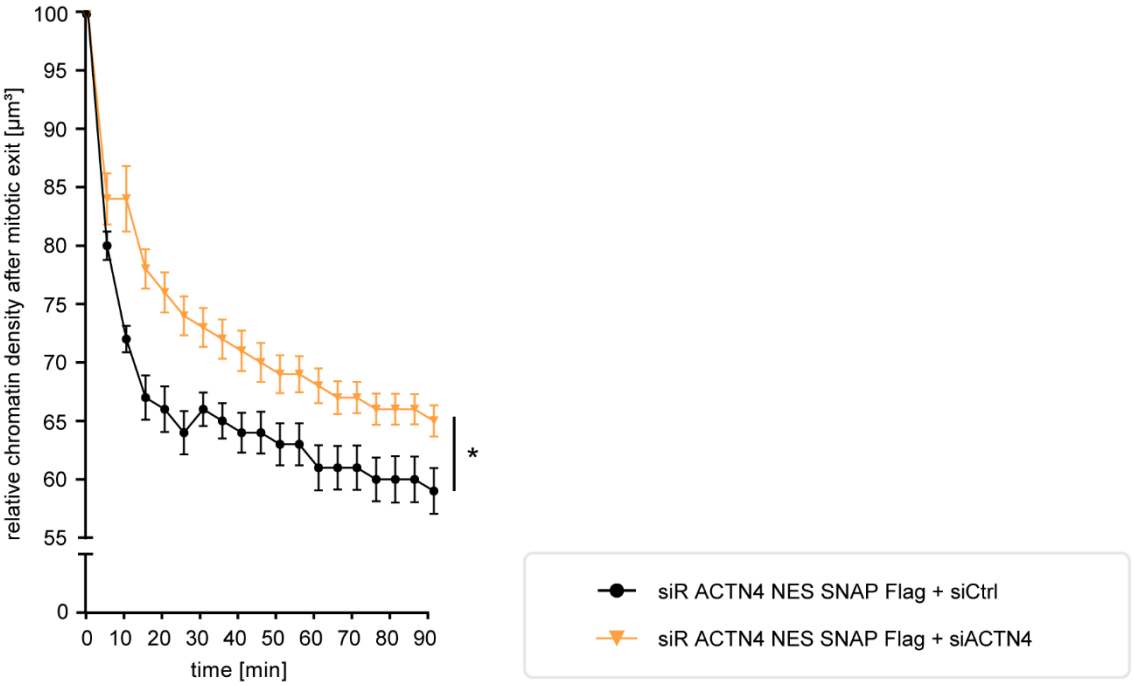

Figure 26. Chromatin densities are increased in ACTN4 depleted cells.

NIH3T3 cells expressing ACTN4 siR NES were transfected with either siCtrl or siACTN4; data shown as mean ± SEM: 44-48 nuclei(siCtrl) and 44-47 nuclei(siACTN4) from 5 independent experiments; p = 0.0281. Statistics was done with unpaired two-tailed Student's t-test.

4.4.2 Cells expressing dominant negative ACTN4 NLS exhibit defects in proliferation

We further assessed the relevance of inhibiting nuclear F-actin bundling for general cellular processes, i.e. proliferation.

To start from a homogenous cell population, NIH3T3 cells stably expressing dn ACTN4 NLS SNAP Flag and the ACTN4 wt version, respectively, were induced with doxycycline, following SNAP labelling. Subsequent FACS enabled sorting of 100 fluorescent cells per well prior to proliferation analysis.

WST-1 assays were performed every 24 h, starting after cells have attached – indicated as timepoint 0. Days 3, 4 and 5 after FACS displayed significantly altered proliferation rates for cells expressing the dn ACTN4 NLS mutant (Fig 27). These results point towards an important role of ACTN4 in nuclear actin bundling at mitotic exit.

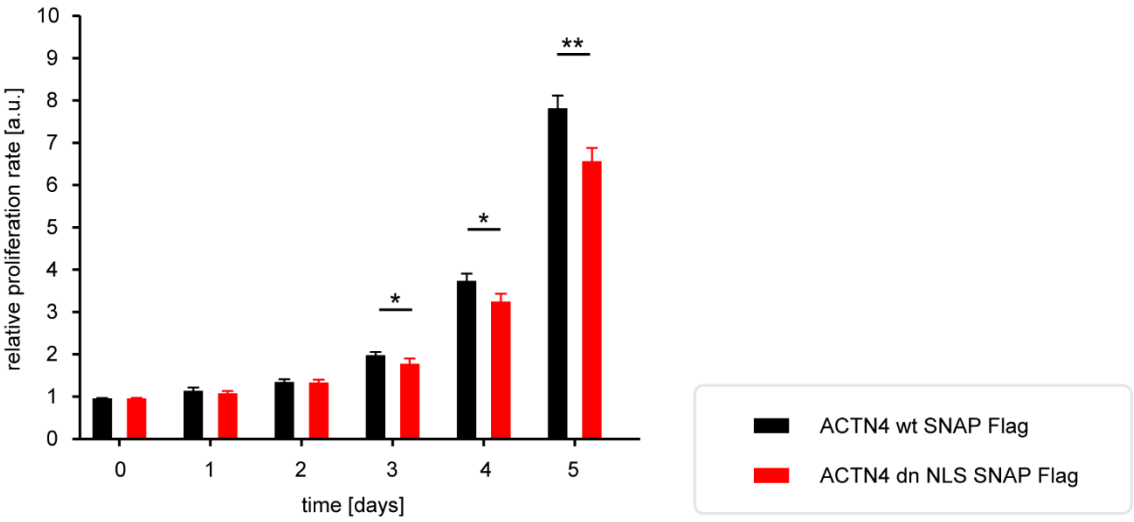

Figure 27. WST-1 assay reveals proliferation defects in dn ACTN4 NLS cells.

WST-1 Proliferation Assay. Values (at least triplicates) were normalized to timepoint 0 of control cells; data shown as mean ± SEM from 3 independent experiments; p(day3) = 0.0271; p(day4) = 0.0120; p(day5) = 0.0018; p(day6) = 0.0161. Statistics was done with unpaired two-tailed Student's t-test.

5. Discussion

The existence of spectrin repeat (SR) proteins including non-muscle ACTN's in the nuclei of mammalian cells was revealed by several research groups [196]. We confirmed that ACTN4 was present in the nuclear compartment in different stages of the cell cycle and its abundance in postmitotic nuclei suggested a function during nuclear F-actin assembly during the early G1 phase. Consistent with this, we found that ACTN4 depletion or expression of dominant negative ACTN4 resulted in reduced nuclear volume expansion after mitotic exit.

Changes in nuclear size or shape are associated with differentiation and disease [89], but definite consequences of an altered morphology are still not fully understood. It has been suggested that chromatin organization and gene expression is affected when nuclear morphology is altered in cancer cells [89]. Atypical nuclei which were identified in tumor cells are therefore characterized by their abnormal sizes, circularities and chromatin densities [129]. Adenocarcinomas expressing high levels of the tumor suppressor p53 displayed large nuclei with high chromatin densities and altered nuclear shapes [129]. ACTN4 was also reported to activate p53 via the nuclear protein cyclin-dependent kinase inhibitor 2A-interacting protein (CDKN2AIP) [52]. Hence, this interaction could potentially influence nuclear morphology and chromatin structure and thus play important roles in the development of cancer.

The nuclear envelope was initially found to promote nuclear expansion in yeast. According to this, decreased nuclear volume due to incomplete nuclear envelope expansion led to defects in chromosome segregation in fission yeast mitosis [170]. Reduced nuclear size during embryogenesis of *Caenorrhabditis elegans* (*C. elegans*) resulted in increased chromosome condensation [74]. Of note, we observed reduced nuclear volume expansion as well as increased chromatin densities in postmitotic nuclei of ACTN4 depleted or dn ACTN4 NLS expressing cells.

Interestingly, our data suggest an adaptation mechanism to control nuclear size while progressing the cell cycle (Fig 22 D). We could not observe alterations in cell size or shape in later stages of the cell cycle (8 h after mitotic exit) and therefore assumed an assimilation mechanism according to the cellular-nuclear scaling paradigm [115]. Future investigations will be necessary to elucidate the exact mechanisms.

From that, we proposed a requirement of ACTN4 for correct nuclear volume expansion in early G1 and a potential involvement of other factors as well in later stages. It is tempting to speculate that compensation of ACTN4 knockdown by other crosslinking proteins may play a role. For instance, spectrin is thought to accomplish nuclear functions similar to those provided by ACTN4 [196] and fimbrin can compensate ACTN4 knockdown (and vice versa) during cytokinetic ring assembly [125]. A potential compensatory mechanism could explain why NIH3T3 cells expressing actin^{R62D} – a non-polymerizable mutant of actin – obtained stronger reduction in nuclear volume expansion (approx. 40 % vs. 18 % reduction with siACTN4, Fig 20 A compared to [12] silencing of ACTN4 in our study. Moreover, actin^{R62D} expressing cells show a more significant reduction in proliferation (approx. 70 % vs. 19 % reduction with siACTN4 after 5 days, Fig 28 compared to [12]). Senescence and decreased proliferation might be due to failed double strand break repair that was shown to depend on polymerized actin [158]. Hence, we hypothesize that ACTN4 might not be involved in double strand break repair and therefore led to a less severe proliferation defect.

Furthermore, postmitotic and interphase nuclei could be exposed to different intracellular forces: Next to intranuclear force generated by F-actin [12], one might consider the existence of cytoplasmic proteins –attached to the nuclear envelope, possibly by the LINC complex – which could increase nuclear volume by pulling the lamina outwards. Those factors are mostly unknown, but microtubules were found to drive pulling forces in a dynein-dependent fashion to allow centrosome centration in C. elegans [98].

We confirmed that postmitotic nuclear volume expansion was further dependent on ACTN4 in mesenchymal and epithelial cell lines. The resulting space of 40 nm between the actin filaments bundled by ACTN4 dimers (Fig 7), could enable incorporation of myosin(II) and thus formation of contractile bundles [39]. Those could generate forces that allow expansion of the nuclear lamina and chromatin rearrangement. Nuclear F-actin assembly is supposedly not affected by ACTN4 (Fig 24), but unbundled (single) actin filaments in dn ACTN4 NLS (Fig 24) nuclei might be unable to create an array for myosin(II)-dependent contractile forces [53, 82]. Unpublished data from our group showed that myosin(II) inhibition by blebbistatin diminished nuclear volume expansion (Thesis M. Plessner) and we further found ACTN4's pivotal role in postmitotic F-actin bundling (Fig 25).

All in all, we speculate that postmitotic nuclear volume expansion required actomyosin-based intranuclear force depending on F-actin bundling by ACTN4 (Fig 28). Accordingly,

nuclei lacking ACTN4 could not expand to a normal extent and chromatin could not decondense completely (Fig 26, 27).

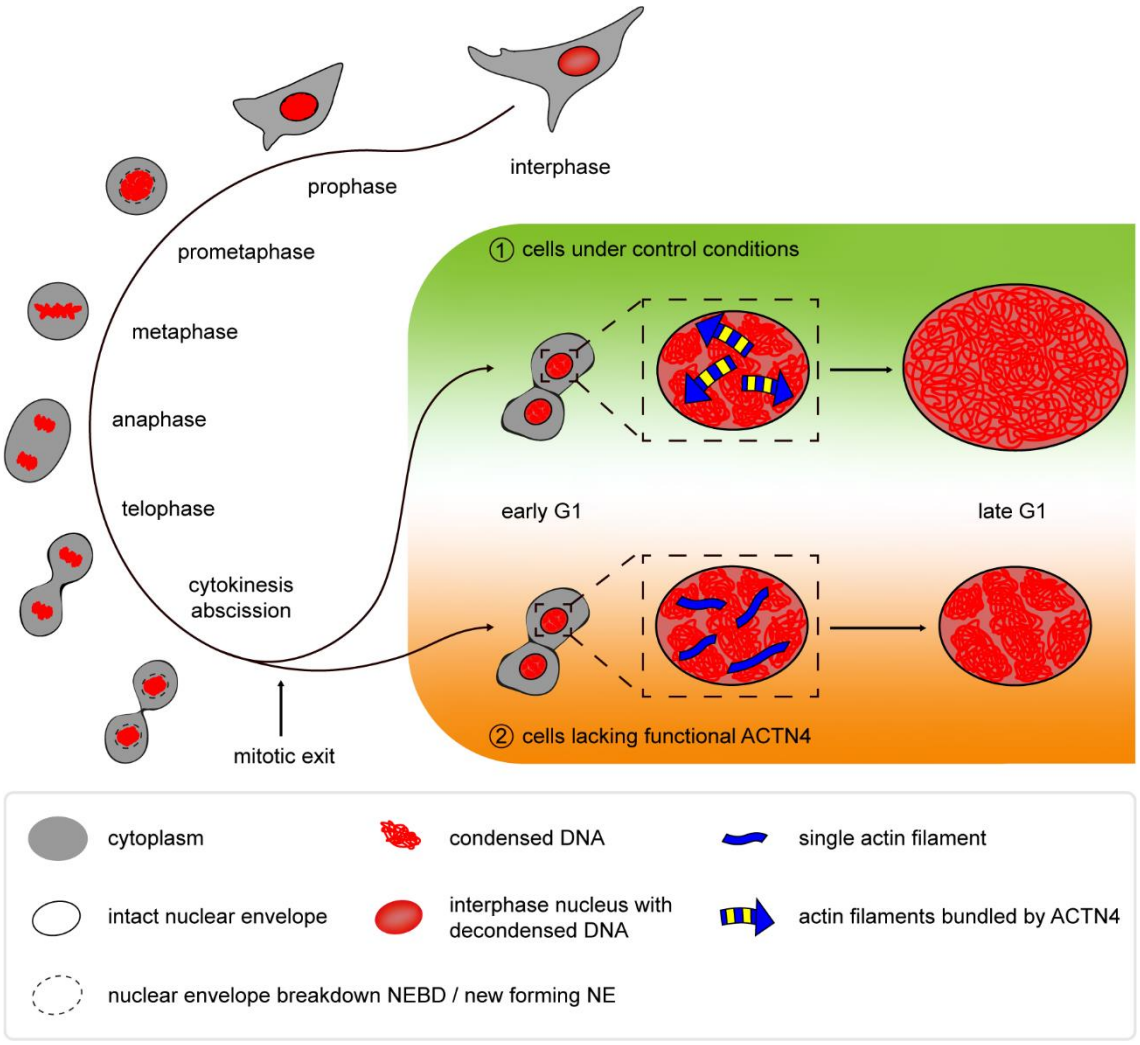

Figure 28. Proposed model for defects in nuclear volume expansion in ACTN4-lacking cells.
Explanation for M-phase in Fig 2. In early G1, control nuclei expand, and chromatin structure is decondensed. In nuclei silenced for ACTN4 or expressing the dn ACTN4 NLS, expansion is impaired, and chromatin reveals higher density and compaction.

The underlying mechanisms of nuclear actin-mediated chromatin decondensation are unidentified and thus need to be analyzed prospectively.

As described earlier in this work, ACTN1 and ACTN4 represent similar protein structures with 87 % identity in amino acid sequence and heterodimerization of these two isoforms is more abundant than homodimerization [53]. Besides the common expression patterns

in cytoplasmic and membrane-associated structures, we revealed nuclear localization of both isoforms. Surprisingly, only knockdown of ACTN4, but not ACTN1 led to impaired nuclear volume expansion in early G1. It is therefore tempting to speculate that the two non-muscle ACTN's have distinct functions and are regulated by different mechanisms; which is in line with previous observations from other groups. Back in the 1990's, researchers observed distinct localization of ACTN1 and ACTN4 in migrating cells [78]. Although both ACTN1 and ACTN4 were present in all kinds of stress fibers, their expression pattern differs in dorsal stress fibers, as ACTN1 showed abundant expression along these non-contractile fibers, while ACTN4 only localized to the origin of focal adhesions [102]. Hence, ACTN1 was reported to regulate the formation of focal adhesions, whereas ACTN4 induced their turnover which could be associated with cancer pathogenesis [56]. Moreover, ACTN4 showed distinct impact on actin dynamics involved in endocytic processes [7]. Despite pronounced structural similarities of ACTN1 and ACTN4, they seem to exert different functions in various cellular compartments.

Here, we identified ACTN4 as one regulator for nuclear volume expansion and F-actin bundling after mitotic exit. Of note, nuclear volumes assimilated in later stages, but the cells proliferated slower in 5 days after inducing the expression of the dominant negative mutant. In addition to its function in postmitotic daughter nuclei expansion, we suggest subsequent effects of nuclear-localized ACTN4 on cell cycle progression. Accordingly, we performed flow cytometry experiments (data not shown) in RPE-1 cells synchronized with the CDK1 inhibitor RO3306. Notably, cells silenced for ACTN4 resisted the inhibitory influence and did not synchronize at the G2/M border, suggesting defects in CDK1 regulation caused by ACTN4 knockdown prior to mitotic entry.

To expand our findings and results in the future, one could consider dual-color high resolution imaging to verify co-localization of F-actin with both ACTN4 and myosin(II), but this will require establishment of valid labeling procedures to visualize all at the same time: Using split GFP could be a plausible approach to not only show overlapping localizations, but also to verify the interactions. Only if ACTN4 labelled with one part of the split GFP has bound F-actin carrying the other part, the fluorescent protein can refold and GFP signal can be detected. We could further label F-actin and myosin(II) in a similar way to gain more detailed information about the nucleoskeletal structure.

CoIP or pulldown experiments are a good approach to identify potential interactions of ACTNs with actin and myosin. Atomic force microscopy enables the direct measurement of mechanical properties in cells, such as membrane rigidity or flexibility [6] and it

revealed flattened nuclei lacking protrusions in nuclei expressing polymerization-deficient actin^{R62D} [12]. Using this technique, one could be able to determine forces generated inside the nuclei of ACTN4 depleted compared to control cells, whereas analyzing cytoplasmic microtubules could help identifying a potential mechanism how the nuclear membrane is pulled to increase size. Of note, it is crucial to analyze the roles of other SR proteins during this dynamic process.

In addition to conventional CoIPs, chromatin Immunoprecipitation (ChIP) might be a good approach to analyze whether ACTN4 is directly interacting with chromatin or if changes in chromatin structure are due to indirect signaling pathways or mechanical stimuli. Hi-C analysis and subsequent next generation sequencing could help to map the general structure and to identify chromatin interaction sites as well as nuclear organization [22]. Furthermore, fluorescence lifetime imaging (FLIM) and Förster resonance energy transfer (FRET) could provide valuable information about dynamic protein-protein interactions in living cells (FLIM-FRET) [144].

To date, we do not know all details of how chromatin remodeling is regulated. Nevertheless, it is fundamental to analyze histone structures because these proteins act as the chromatin subunit essential for DNA packaging and compaction. Histone modifications are crucial for initiation and progression of mitosis. Specific acetylation patterns are important for their function, consequent gene transcription and cell proliferation, as many transcription factors bind to acetylated histones [153]. Differences in acetylation and deacetylation states can lead to malignancies such as cancer: Transcription of oncogenes could be activated, but on the other hand, tumor suppressors could be less transcribed [153]. Preliminary data (not shown) suggested a change in phosphorylation of histone H3 (H3S10ph) and corresponding acetylation in histone H4 (H4K16ac) in ACTN4 knockdown cells throughout the cell cycle. Histone H3 is phosphorylated at serine 10 during M-phase, while histone H4 occurs in the acetylated state during interphase [193]. Hence, screening for these modifications is a plausible tool to analyze the influence of ACTN4 knockdown on cell cycle progression.

Given that ACTN4 depletion impairs chromatin remodeling in early G1, consecutive S phase and cell cycle progression could also be altered. Therefore, general function of DNA replication needs to be investigated. Previous publications showed that actin dynamics and formins are required for this process [133].

It was previously shown that the CH1 domain of ACTN4 alone can bind actin, but the affinity is lower compared to the tandem CH domain and it was further reported that the

CH2 domain alone is unable to bind actin [164]. Surprisingly, preliminary CoIP experiments with dn ACTN4 NLS (data not shown) suggest that this mutant can still bind actin, but indeed exhibits dominant negative properties in SRF reporter gene assays (Fig 21). Consequently, structural und functional analyses should follow to advance our knowledge concerning the different domains in ACTN4.

A relevance for ACTN4 to induce tumor growth and metastasis has been reported that needs to be further investigated with regard to its role in nuclear actin dynamics in cancer cells using migration and invasion assays.

6. Summary

Nuclear actin and its biological relevance raised much interest in the past few years. Although its existence was initially discussed controversially, more recent data provided insights into its functions and address stimuli as well as dynamics of nuclear actin filaments. Hence, our group recently showed that nuclear volume expansion in early G1 of mammalian cells required a network of transient and dynamic F-actin inside the daughter nuclei.

However, only few regulatory pathways in nuclear F-actin formation were identified, while higher organization of actin filaments remained mostly uninvestigated. As such, the roles of actin crosslinking proteins were less well explored, but members of the spectrin repeat family were proposed to have nuclear functions. For instance, nucleocytoplasmic shuttling of the actin-bundling protein Alpha actinin-4 was associated with invasive cancer phenotypes. We therefore decided to investigate non-muscle Alpha actinins and their roles in early G1 nuclei.

We initially confirmed cytoplasmic and nuclear localization of Alpha actinin-4 in interphase and early G1 cells and its interaction with nuclear F-actin by immunostaining and phalloidin pulldown experiments. Subcellular fractionations and subsequent Co-immunoprecipitations revealed the presence of Alpha actinin-1 SNAP Flag in the nuclear compartment. Imaging of histone 2B mCherry expressing cells during early G1 and following 3D reconstructions allowed for nuclear volume analysis and revealed that Alpha actinin-4, but not Alpha actinin-1 was required for proper nuclear volume expansion. We further visualized nuclear F-actin (bundles) in fixed postmitotic cells by super-resolution microscopy. Expression of a nuclear targeted dominant negative mutant of Alpha actinin-4 exhibited a significant reduction of phalloidin-AlexaFluor647 localizations per nucleus compared to the wild-type construct. These nuclei further represented fewer actin filament bundles with reduced widths, suggesting that Alpha actinin-4 is a key regulator of nuclear F-actin bundling and proper nuclear volume expansion in early G1.

Further investigations revealed an additional involvement of nuclear Alpha actinin-4 in other cellular processes such as proliferation.

Together, this work provides information about crucial functions of Alpha actinin-4 in the nuclear compartment of postmitotic mammalian cells and might therefore aid future investigations into its role for tumorigenesis and metastasis.

7. Zusammenfassung

In den letzten Jahren haben nukleäres Aktin und seine biologische Relevanz an Bedeutung gewonnen. Obwohl seine Existenz zunächst kontrovers diskutiert wurde, liefern aktuelle Studien nun Einblicke in dessen Funktion und beschäftigen sich mit den Stimulanzien sowie der Dynamik nukleärer Aktinfilamente. Unsere Gruppe hat dahingehend erst kürzlich gezeigt, dass die postmitotische nukleäre Volumenexpansion in Säugerzellen ein transientes und dynamisches Netzwerk aus Aktinfilamenten in den Tochterkernen erfordert.

Für die Bildung nukleärer Aktinfilamente wurden nur wenige Regulationswege identifiziert, die Ausbildung höher organisierter Aktinfilamente bleibt sogar völlig unerforscht. Dementprechend ist nicht bekannt, welche Rolle jene Proteine spielen, die Aktinfilamente quervernetzen; Vertretern der Spectrin Repeat-Proteine werden jedoch Funktionen im Zellkern zugesprochen. Beispielsweise wurde gezeigt, dass Alpha Aktinin-4, durch die Fähigkeit vom Zytoplasma in den Kern zu pendeln und vice versa, mit invasiven Krebsphänotypen assoziiert ist. Daher entschieden wir uns, die nicht sarkomerischen Isoformen Alpha Aktinin-1 und Alpha Aktinin-4 und vor allem deren Funktionen in Zellkernen der frühen G1-Phase zu untersuchen.

Wir konnten mit Hilfe von Immunfärbungen und Phalloidin-Pulldowns bestätigen, dass Alpha Aktinin-4 in Interphasekernen und ebenso in Kernen von postmitotischen Zellen vorkommt und dass es mit Aktinfilamenten interagiert. Subzelluläre Fraktionierungen und nachfolgende Ko-Immunpräzipitationen erlaubten es uns, Alpha Aktinin-1 SNAP Flag im nukleären Kompartiment nachzuweisen. Visualisierung von Histon 2B mCherry-exprimierenden Zellen während der frühen G1-Phase und anschließende 3D-Rekonstruktion der Zellkerne ermöglichten nukleäre Volumenanalysen. Diese offenbarten, dass Alpha Aktinin-4, nicht aber Alpha Aktinin-1, für die korrekte nukleäre Volumenexpansion nach der Mitose erforderlich war.

Darüber hinaus visualisierten wir nukleäre Aktinfilamentbündel in fixierten postmitotischen Zellen mit Hilfe von hochauflösender Mikroskopie. Verglichen mit dem Alpha Aktinin-4 Wildtyp-Konstrukt, führte die Expression einer kernständigen dominant negativen Mutante des Alpha Aktinin-4 zu einer signifikanten Reduktion der Phalloidin-AlexaFluor647-Lokalisationen in den Tochterkernen. Außerdem wiesen diese Zellkerne

weniger Aktinfilamentbündel mit jeweils verringerter Breite auf, was darauf hindeutet, dass Alpha Aktinin-4 einen wichtigen Regulator für die Ausbildung postmitotischer Aktinfilamentbündel und korrekte nukleäre Volumenexpansion in der frühen G1-Phase darstellt.

Weitere Untersuchungen zeigten eine zusätzliche Beteiligung des Alpha Aktinin-4 an anderen zellulären Prozessen, wie etwa Proliferation.

Alles in allem liefert diese Arbeit Informationen zu wichtigen Funktionen des Alpha Aktinin-4 im nukleären Kompartiment postmitotischer Säugerzellen und könnte daher helfen, dessen Rolle in Prozessen wie Tumorgenese und Metastasierung zu untersuchen.

8. References

[1] Aberle, H. 2013. Redox switch for actin. *Nature cell biology* 15, 12, 1403–1404.

[2] Acevedo, A. and González-Billault, C. 2018. Crosstalk between Rac1-mediated actin regulation and ROS production. *Free radical biology & medicine* 116, 101–113.

[3] Aksenova, V., Turoverova, L., Khotin, M., Magnusson, K.-E., Tulchinsky, E., Melino, G., Pinaev, G. P., Barlev, N., and Tentler, D. 2013. Actin-binding protein alpha-actinin 4 (ACTN4) is a transcriptional co-activator of RelA/p65 sub-unit of NF-kB. *Oncotarget* 4, 2, 362–372.

[4] Alberts, B., Johnson, A., Lewis, J., Morgan, D., Raff, M., Roberts, K., Walter, P., Wilson, J., and Hunt, T. 2015. *Molecular biology of the cell*. Garland Science Taylor and Francis Group, New York, NY.

[5] Alberts, B., Johnson, A., Lewis, J., Raff, M., Roberts, K., and Walter, P. 2002. *Chromosomal DNA and Its Packaging in the Chromatin Fiber*. Garland Science.

[6] Alonso, J. L. and Goldmann, W. H. 2003. Feeling the forces: atomic force microscopy in cell biology. *Life Sciences* 72, 23, 2553–2560.

[7] Araki, N., Hatae, T., Yamada, T., and Hirohashi, S. 2000. Actinin-4 is preferentially involved in circular ruffling and macropinocytosis in mouse macrophages: analysis by fluorescence ratio imaging. *Journal of cell science* 113 (Pt 18), 3329–3340.

[8] Ashwell, M. A. and Jackson, R. F. W. 1988. A New Method for the Preparation of α-Nitroacetophenones. *Synthesis* 1988, 03, 229–231.

[9] Ayala, R., Willhoft, O., Aramayo, R. J., Wilkinson, M., McCormack, E. A., Ocloo, L., Wigley, D. B., and Zhang, X. 2018. Structure and regulation of the human INO80-nucleosome complex. *Nature* 556, 7701, 391–395.

[10] Baarlink, C., Brandt, D., and Grosse, R. 2010. SnapShot: Formins. *Cell* 142, 1, 172, 172.e1.

[11] Baarlink, C. and Grosse, R. 2014. Formin' actin in the nucleus. *Nucleus (Austin, Tex.)* 5, 1, 15–20.

[12] Baarlink, C., Plessner, M., Sherrard, A., Morita, K., Misu, S., Virant, D., Kleinschnitz, E.-M., Harniman, R., Alibhai, D., Baumeister, S., Miyamoto, K., Endesfelder, U., Kaidi, A., and Grosse, R. 2017. A transient pool of nuclear F-actin at mitotic exit controls chromatin organization. *Nature cell biology* 19, 12, 1389–1399.

[13] Baarlink, C., Wang, H., and Grosse, R. 2013. Nuclear actin network assembly by formins regulates the SRF coactivator MAL. *Science (New York, N.Y.)* 340, 6134, 864–867.

[14] Babakov, V. N., Petukhova, O. A., Turoverova, L. V., Kropacheva, I. V., Tentler, D. G., Bolshakova, A. V., Podolskaya, E. P., Magnusson, K.-E., and Pinaev, G. P. 2008. RelA/NF-kappaB transcription factor associates with alpha-actinin-4. *Experimental cell research* 314, 5, 1030–1038.

[15] Bamburg, J. R. 1999. Proteins of the ADF/cofilin family: essential regulators of actin dynamics. *Annual review of cell and developmental biology* 15, 185–230.

[16] Bamburg, J. R. and Bernstein, B. W. 2016. Actin dynamics and cofilin-actin rods in Alzheimer disease. *Cytoskeleton (Hoboken, N.J.)* 73, 9, 477–497.

[17] Bartram, M. P., Habbig, S., Pahmeyer, C., Höhne, M., Weber, L. T., Thiele, H., Altmüller, J., Kottoor, N., Wenzel, A., Krueger, M., Schermer, B., Benzing, T., Rinschen, M. M., and Beck, B. B. 2016. Three-layered proteomic characterization of a novel ACTN4 mutation unravels its pathogenic potential in FSGS. *Human molecular genetics* 25, 6, 1152–1164.

[18] Begg, D. A., Rodewald, R., and Rebhun, L. I. 1978. The visualization of actin filament polarity in thin sections. Evidence for the uniform polarity of membrane-associated filaments. *J Cell Biol* 79, 3, 846–852.

[19] Belin, B. J., Cimini Beth A., Blackburn Elizabeth H., and Mullins, R. D. 2013. Visualization of actin filaments and monomers in somatic cell nuclei. *Molecular biology of the cell* 24, 982-994.

[20] Belin, B. J., Lee, T., and Mullins, D. 2015. DNA damage induces nuclear actin filament assembly by Formin-2 and Spire1/2 that promotes efficient DNA repair. *elifesciences*.

[21] Belin, B. J. and Mullins, R. D. 2013. What we talk about when we talk about nuclear actin. *Nucleus (Austin, Tex.)* 4, 4, 291–297.

[22] Belton, J.-M., McCord, R. P., Gibcus, J. H., Naumova, N., Zhan, Y., and Dekker, J. 2012. Hi-C: a comprehensive technique to capture the conformation of genomes. *Methods (San Diego, Calif.)* 58, 3, 268–276.

[23] Blanchoin, L., Boujemaa-Paterski, R., Sykes, C., and Plastino, J. 2014. Actin dynamics, architecture, and mechanics in cell motility. *Physiological reviews* 94, 1, 235–263.

[24] Blanchoin, L. and Pollard, T. D. 2002. Hydrolysis of ATP by polymerized actin depends on the bound divalent cation but not profilin. *Biochemistry* 41, 2, 597–602.

[25] Boldogh, I. R., Yang, H. C., Nowakowski, W. D., Karmon, S. L., Hays, L. G., Yates, J. R., and Pon, L. A. 2001. Arp2/3 complex and actin dynamics are required for actin-based mitochondrial motility in yeast. *Proceedings of the National Academy of Sciences of the United States of America* 98, 6, 3162–3167.

[26] Bonello, T. T., Janco, M., Hook, J., Byun, A., Appaduray, M., Dedova, I., Hitchcock-DeGregori, S., Hardeman, E. C., Stehn, J. R., Böcking, T., and Gunning, P. W. 2016. A small molecule inhibitor of tropomyosin dissociates actin binding from tropomyosin-directed regulation of actin dynamics. *Scientific reports* 6.

[27] Brandt, D. T., Baarlink, C., Kitzing, T. M., Kremmer, E., Ivaska, J., Nollau, P., and Grosse, R. 2009. SCAI acts as a suppressor of cancer cell invasion through the transcriptional control of beta1-integrin. *Nature cell biology* 11, 5, 557–568.

[28] Bravo-Cordero, J. J., Magalhaes, M. A. O., Eddy, R. J., Hodgson, L., and Condeelis, J. 2013. Functions of cofilin in cell locomotion and invasion. *Nature reviews. Molecular cell biology* 14, 7.

[29] Burdyniuk, M., Callegari, A., Mori, M., Nédélec, F., and Lénárt, P. 2018. F-Actin nucleated on chromosomes coordinates their capture by microtubules in oocyte meiosis. *The Journal of cell biology* 217, 8, 2661–2674.

[30] Burridge, K. and Wittchen, E. S. 2013. The tension mounts: stress fibers as force-generating mechanotransducers. *The Journal of cell biology* 200, 1, 9–19.

[31] Campellone, K. G. and Welch, M. D. 2010. A Nucleator Arms Race: Cellular Control of Actin Assembly. *Nature reviews. Molecular cell biology* 11, 4, 237–251.

[32] Caridi, C. P., Plessner, M., Grosse, R., and Chiolo, I. 2019. Nuclear actin filaments in DNA repair dynamics. *Nature cell biology* 21, 9, 1068–1077.

[33] Carpenter, C. L. 2000. Actin cytoskeleton and cell signaling. *Critical care medicine* 28, 4 Suppl, N94-9.

[34] Chakrabarti, R., Ji, W.-K., Stan, R. V., Juan Sanz, J. de, Ryan, T. A., and Higgs, H. N. 2018. INF2-mediated actin polymerization at the ER stimulates mitochondrial calcium uptake, inner membrane constriction, and division. *The Journal of cell biology* 217, 1, 251–268.

[35] Chesarone, M. A., DuPage, A. G., and Goode, B. L. 2010. Unleashing formins to remodel the actin and microtubule cytoskeletons. *Nature reviews. Molecular cell biology* 11, 1, 62–74.

[36] Chhabra, E. S. and Higgs, H. N. 2007. The many faces of actin: matching assembly factors with cellular structures. *Nature cell biology* 9, 10, 1110–1121.

[37] Cibulka, J., Fraiberk, M., and Forstova, J. 2012. Nuclear actin and lamins in viral infections. *Viruses* 4, 3, 325–347.

[38] Clark, T. G. and Rosenbaum, J. L. 1979. An actin filament matrix in hand-isolated nuclei of X. laevis oocytes. *Cell* 18, 4, 1101–1108.

[39] Cooper, G. M. 2000. *The cell*. *A molecular approach*. ASM Press, Washington, DC.

[40] Cramer, L. P., Siebert, M., and Mitchison, T. J. 1997. Identification of novel graded polarity actin filament bundles in locomoting heart fibroblasts: implications for the generation of motile force. *J Cell Biol* 136, 6, 1287–1305.

[41] Di Feng, Notbohm, J., Benjamin, A., He, S., Wang, M., Ang, L.-H., Bantawa, M., Bouzid, M., Del Gado, E., Krishnan, R., and Pollak, M. R. 2018. Disease-causing mutation in α-actinin-4 promotes podocyte detachment through maladaptation to periodic stretch. *Proceedings of the National Academy of Sciences of the United States of America* 115, 7, 1517–1522.

[42] Dimchev, G., Steffen, A., Kage, F., Dimchev, V., Pernier, J., Carlier, M.-F., and Rottner, K. 2017. Efficiency of lamellipodia protrusion is determined by the extent of cytosolic actin assembly. *Molecular biology of the cell* 28, 10, 1311–1325.

[43] Dopie, J., Skarp, K.-P., Rajakylä, E. K., Tanhuanpää, K., and Vartiainen, M. K. 2012. Active maintenance of nuclear actin by importin 9 supports transcription. *Proceedings of the National Academy of Sciences of the United States of America* 109, 9, E544-52.

[44] Edelstein, A. D., Tsuchida, M. A., Amodaj, N., Pinkard, H., Vale, R. D., and Stuurman, N. 2014. Advanced methods of microscope control using μManager software. *Journal of biological methods* 1, 2.

[45] Edlund, M., Lotano, M. A., and Otey, C. A. 2001. Dynamics of ?-actinin in focal adhesions and stress fibers visualized with ?-actinin-green fluorescent protein. *Cell Motility and the Cytoskeleton* 48, 3, 190–200.

[46] Endesfelder, U., Malkusch, S., Fricke, F., and Heilemann, M. 2014. A simple method to estimate the average localization precision of a single-molecule localization microscopy experiment. *Histochemistry and cell biology* 141, 6, 629–638.

[47] Feierbach, B., Piccinotti, S., Bisher, M., Denk, W., and Enquist, L. W. 2006. Alpha-herpesvirus infection induces the formation of nuclear actin filaments. *PLoS pathogens* 2, 8, e85.

[48] Feng, Y., Ngu, H., Alford, S. K., Ward, M., Yin, F., and Longmore, G. D. 2013. α-actinin1 and 4 tyrosine phosphorylation is critical for stress fiber establishment, maintenance and focal adhesion maturation. *Experimental cell research* 319, 8, 1124–1135.

[49] Feric, M. and Brangwynne, C. P. 2013. A nuclear F-actin scaffold stabilizes ribonucleoprotein droplets against gravity in large cells. *Nature cell biology* 15, 10, 1253–1259.

[50] Fischer, U., Huber, J., Boelens, W. C., Mattaj, I. W., and Lührmann, R. 1995. The HIV-1 Rev activation domain is a nuclear export signal that accesses an export pathway used by specific cellular RNAs. *Cell* 82, 3, 475–483.

[51] Flood, G., Rowe, A. J., Critchley, D. R., and Gratzer, W. B. 1997. Further analysis of the role of spectrin repeat motifs in alpha-actinin dimer formation. *European biophysics journal : EBJ* 25, 5-6, 431–435.

[52] Foley, K. S. and Young, P. W. 2013. An analysis of splicing, actin-binding properties, heterodimerization and molecular interactions of the non-muscle α-actinins. *The Biochemical journal* 452, 3, 477–488.

[53] Foley, K. S. and Young, P. W. 2014. The non-muscle functions of actinins: an update. *The Biochemical journal* 459, 1, 1–13.

[54] Freedman, D. and Diaconis, P. 1981. On the histogram as a density estimator:L 2 theory. *Z. Wahrscheinlichkeitstheorie verw Gebiete* 57, 4, 453–476.

[55] Fritz-Laylin, L. K., Riel-Mehan, M., Chen, B.-C., Lord, S. J., Goddard, T. D., Ferrin, T. E., Nicholson-Dykstra, S. M., Higgs, H., Johnson, G. T., Betzig, E., and Mullins, R. D. 2017. Actin-based protrusions of migrating neutrophils are intrinsically lamellar and facilitate direction changes. *eLife* 6.

[56] Fukumoto, M., Kurisu, S., Yamada, T., and Takenawa, T. 2015. α-Actinin-4 enhances colorectal cancer cell invasion by suppressing focal adhesion maturation. *PloS one* 10, 4, e0120616.

[57] Galkin, V. E., Orlova, A., Salmazo, A., Djinovic-Carugo, K., and Egelman, E. H. 2010. Opening of tandem calponin homology domains regulates their affinity for F-actin. *Nature structural & molecular biology* 17, 5, 614–616.

[58] Gao, Q. Q. and McNally, E. M. 2015. The Dystrophin Complex: Structure, Function, and Implications for Therapy. *Comprehensive Physiology* 5, 3, 1223–1239.

[59] Gateva, G., Kremneva, E., Reindl, T., Kotila, T., Kogan, K., Gressin, L., Gunning, P. W., Manstein, D. J., Michelot, A., and Lappalainen, P. 2017. Tropomyosin Isoforms Specify Functionally Distinct Actin Filament Populations In Vitro. *Current Biology* 27, 5, 705–713.

[60] Goins, L. M. and Mullins, R. D. 2015. A novel tropomyosin isoform functions at the mitotic spindle and Golgi in Drosophila. *Molecular biology of the cell* 26, 13, 2491–2504.

[61] Goldschmidt-Clermont, P. J., Furman, M. I., Wachsstock, D., Safer, D., Nachmias, V. T., and Pollard, T. D. 1992. The control of actin nucleotide exchange by thymosin beta 4 and profilin. A potential regulatory mechanism for actin polymerization in cells. *Molecular biology of the cell* 3, 9, 1015–1024.

[62] Goley, E. D. and Welch, M. D. 2006. The ARP2/3 complex: an actin nucleator comes of age. *Nature reviews. Molecular cell biology* 7, 10, 713–726.

[63] Gounon, P. and Karsenti, E. 1981. Involvement of contractile proteins in the changes in consistency of oocyte nucleoplasm of the newt Pleurodeles waltlii. *J Cell Biol* 88, 2, 410–421.

[64] Graceffa, P. and Dominguez, R. 2003. Crystal structure of monomeric actin in the ATP state. Structural basis of nucleotide-dependent actin dynamics. *J. Biol. Chem.* 278, 36, 34172–34180.

[65] Grazi, E. 1997. What is the diameter of the actin filament? *FEBS letters* 405, 3, 249–252.

[66] Grikscheit, K. and Grosse, R. 2016. Formins at the Junction. *Trends in biochemical sciences* 41, 2, 148–159.

[67] Grobe, H., Wüstenhagen, A., Baarlink, C., Grosse, R., and Grikscheit, K. 2018. A Rac1-FMNL2 signaling module affects cell-cell contact formation independent of Cdc42 and membrane protrusions. *PloS one* 13, 3.

[68] Grosse, R., Copeland, J. W., Newsome, T. P., Way, M., and Treisman, R. 2003. A role for VASP in RhoA-Diaphanous signalling to actin dynamics and SRF activity. *The EMBO Journal* 22, 12, 3050–3061.

[69] Grosse, R. and Vartiainen, M. K. 2013. To be or not to be assembled: progressing into nuclear actin filaments. *Nature reviews. Molecular cell biology* 14, 11, 693–697.

[70] Guha, M., Zhou, M., and Wang, Y.-L. 2005. Cortical actin turnover during cytokinesis requires myosin II. *Current biology : CB* 15, 8, 732–736.

[71] Gunning, P. W., Ghoshdastider, U., Whitaker, S., Popp, D., and Robinson, R. C. 2015. The evolution of compositionally and functionally distinct actin filaments. *Journal of cell science* 128, 11, 2009–2019.

[72] Hampton, C. M., Taylor, D. W., and Taylor, K. A. 2007. Novel structures for alpha-actinin:F-actin interactions and their implications for actin-membrane attachment and tension sensing in the cytoskeleton. *Journal of molecular biology* 368, 1, 92–104.

[73] Hara, T., Honda, K., Shitashige, M., Ono, M., Matsuyama, H., Naito, K., Hirohashi, S., and Yamada, T. 2007. Mass spectrometry analysis of the native protein complex containing actinin-4 in prostate cancer cells. *Molecular & cellular proteomics : MCP* 6, 3, 479–491.

[74] Hara, Y., Iwabuchi, M., Ohsumi, K., and Kimura, A. 2013. Intranuclear DNA density affects chromosome condensation in metazoans. *Molecular biology of the cell* 24, 15, 2442–2453.

[75] Hinojosa, L. S., Holst, M., Baarlink, C., and Grosse, R. 2017. MRTF transcription and Ezrin-dependent plasma membrane blebbing are required for entotic invasion. *The Journal of cell biology* 216, 10, 3087–3095.

[76] Hofmann, W. A., Arduini, A., Nicol, S. M., Camacho, C. J., Lessard, J. L., Fuller-Pace, F. V., and Lanerolle, P. de. 2009. SUMOylation of nuclear actin. *The Journal of cell biology* 186, 2, 193–200.

[77] Holmes, K. C., Popp, David, Gebhard, Werner, and Kabsch, W. 1990. Atomic model of the actin filament. *Nature* 347, 44–49.

[78] Honda, K., Yamada, T., Endo, R., Ino, Y., Gotoh, M., Tsuda, H., Yamada, Y., Chiba, H., and Hirohashi, S. 1998. Actinin-4, a Novel Actin-bundling Prtein Associated with Cell Motility and Cancer Invasion. *The Journal of cell biology* 140, 6, 1383–1393.

[79] Honda, K., Yamada, T., Seike, M., Hayashida, Y., Idogawa, M., Kondo, T., Ino, Y., and Hirohashi, S. 2004. Alternative splice variant of actinin-4 in small cell lung cancer. *Oncogene* 23, 30, 5257–5262.

[80] Hotulainen, P. and Lappalainen, P. 2006. Stress fibers are generated by two distinct actin assembly mechanisms in motile cells. *J Cell Biol* 173, 3, 383–394.

[81] Hsu, K.-S. and Kao, H.-Y. 2013. Alpha-actinin 4 and tumorigenesis of breast cancer. *Vitamins and hormones* 93, 323–351.

[82] Hu, S., Dasbiswas, K., Guo, Z., Tee, Y.-H., Thiagarajan, V., Hersen, P., Chew, T.-L., Safran, S. A., Zaidel-Bar, R., and Bershadsky, A. D. 2017. Long-range self-organization of cytoskeletal myosin II filament stacks. *Nature cell biology* 19, 2, 133–141.

[83] Huang, B., Bates, M., and Zhuang, X. 2009. Super-resolution fluorescence microscopy. *Annual review of biochemistry* 78, 993–1016.

[84] Hundt, N., Preller, M., Swolski, O., Ang, A. M., Mannherz, H. G., Manstein, D. J., and Müller, M. 2014. Molecular mechanisms of disease-related human β-actin mutations p.R183W and p.E364K. *The FEBS journal* 281, 23, 5279–5291.

[85] Hung, R.-J., Pak, C. W., and Terman, J. R. 2011. Direct redox regulation of F-actin assembly and disassembly by Mical. *Science (New York, N.Y.)* 334, 6063, 1710–1713.

[86] Huxley, H. E. 1957. THE DOUBLE ARRAY OF FILAMENTS IN CROSS-STRIATED MUSCLE. *The Journal of Biophysical and Biochemical Cytology* 3, 5, 631–648.

[87] Huxley, H. E. 2004. Fifty years of muscle and the sliding filament hypothesis. *European journal of biochemistry* 271, 8, 1403–1415.

[88] Ito, W., Ishiguro, H., and Kurosawa, Y. 1991. A general method for introducing a series of mutations into cloned DNA using the polymerase chain reaction. *Gene* 102, 1, 67–70.

[89] Jevtić, P., Edens, L. J., Vuković, L. D., and Levy, D. L. 2014. Sizing and shaping the nucleus: mechanisms and significance. *Current opinion in cell biology* 28, 16–27.

[90] Kabsch, W., Mannherz, H. G., Suck, D., Pai, E. F., and Holmes, K. C. 1990. Atomic structure of the actin: DNase I complex. *Nature* 347, 6288, 37–44.

[91] Kalderon, D., Roberts, B. L., Richardson, W. D., and Smith, A. E. 1984. A short amino acid sequence able to specify nuclear location. *Cell* 39, 3 Pt 2, 499–509.

[92] Kaplan, J. M., Kim, S. H., North, K. N., Rennke, H., Correia, L. A., Tong, H.-Q., Mathis, B. J., Rodríguez-Pérez, J.-C., Allen, P. G., Beggs, A. H., and Pollak, M. R. 2000. Mutations in ACTN4 , encoding α-actinin-4, cause familial focal segmental glomerulosclerosis. *Nat Genet* 24, 3, 251–256.

[93] Kapoor, P., Chen, M., Winkler, D. D., Luger, K., and Shen, X. 2013. Evidence for monomeric actin function in INO80 chromatin remodeling. *Nature structural & molecular biology* 20, 4, 426–432.

[94] Kemp, J. P. and Brieher, W. M. 2018. The actin filament bundling protein α-actinin-4 actually suppresses actin stress fibers by permitting actin turnover. *The Journal of biological chemistry* 293, 37, 14520–14533.

[95] Khaitlina, S. Y. 2014. Intracellular transport based on actin polymerization. *Biochemistry. Biokhimiia* 79, 9, 917–927.

[96] Khurana, S., Chakraborty, S., Zhao, X., Liu, Y., Guan, D., Lam, M., Huang, W., Yang, S., and Kao, H.-Y. 2012. Identification of a novel LXXLL motif in α-actinin 4-spliced isoform that is critical for its interaction with estrogen receptor α and co-activators. *The Journal of biological chemistry* 287, 42, 35418–35429.

[97] Khurana, S. and George, S. P. 2011. The role of actin bundling proteins in the assembly of filopodia in epithelial cells. *Cell adhesion & migration* 5, 5, 409–420.

[98] Kimura, K. and Kimura, A. 2010. Intracellular organelles mediate cytoplasmic pulling force for centrosome centration in the Caenorhabditis elegans early embryo. *Proceedings of the National Academy of Sciences of the United States of America* 108, 1, 137–142.

[99] Kirschner, M. W. 1980. Implications of Treadmilling for the Stability and Polarity of Actin and Tubulin Polymers in Vivo. *J Cell Biol* 86, 330–334.

[100] Kiseleva, E., Drummond, S. P., Goldberg, M. W., Rutherford, S. A., Allen, T. D., and Wilson, K. L. 2004. Actin- and protein-4.1-containing filaments link nuclear pore complexes to subnuclear organelles in Xenopus oocyte nuclei. *Journal of cell science* 117, Pt 12, 2481–2490.

[101] Kotila, T., Kogan, K., Enkavi, G., Guo, S., Vattulainen, I., Goode, B. L., and Lappalainen, P. 2018. Structural basis of actin monomer re-charging by cyclase-associated protein. *Nature communications* 9, 1, 1892.

[102] Kovac, B., Teo, J. L., Mäkelä, T. P., and Vallenius, T. 2013. Assembly of non-contractile dorsal stress fibers requires α-actinin-1 and Rac1 in migrating and spreading cells. *Journal of cell science* 126, Pt 1, 263–273.

[103] Kristó, I., Bajusz, I., Bajusz, C., Borkúti, P., and Vilmos, P. 2016. Actin, actin-binding proteins, and actin-related proteins in the nucleus. *Histochemistry and cell biology* 145, 4, 373–388.

[104] Kume, K., Cantwell, H., Neumann, F. R., Jones, A. W., Snijders, A. P., and Nurse, P. 2017. A systematic genomic screen implicates nucleocytoplasmic transport and membrane growth in nuclear size control. *PLoS genetics* 13, 5, e1006767.

[105] Kumeta, M., Yoshimura, S. H., Harata, M., and Takeyasu, K. 2010. Molecular mechanisms underlying nucleocytoplasmic shuttling of actinin-4. *Journal of cell science* 123, Pt 7, 1020–1030.

[106] Kunishima, S., Okuno, Y., Yoshida, K., Shiraishi, Y., Sanada, M., Muramatsu, H., Chiba, K., Tanaka, H., Miyazaki, K., Sakai, M., Ohtake, M., Kobayashi, R., Iguchi, A., Niimi, G., Otsu, M., Takahashi, Y., Miyano, S., Saito, H., Kojima, S., and Ogawa, S. 2013. ACTN1 mutations cause congenital macrothrombocytopenia. *American journal of human genetics* 92, 3, 431–438.

[107] La Cour, T., Gupta, R., Rapacki, K., Skriver, K., Poulsen, F. M., and Brunak, S. 2003. NESbase version 1.0: a database of nuclear export signals. *Nucleic acids research* 31, 1, 393–396.

[108] Lans, H. and Hoeijmakers, J. H. J. 2006. Cell biology: ageing nucleus gets out of shape. *Nature* 440, 7080, 32–34.

[109] Laporte, D., Ojkic, N., Vavylonis, D., and Wu, J.-Q. 2012. α-Actinin and fimbrin cooperate with myosin II to organize actomyosin bundles during contractile-ring assembly. *Molecular biology of the cell* 23, 16, 3094–3110.

[110] Lehtimäki, J., Hakala, M., and Lappalainen, P. 2017. Actin Filament Structures in Migrating Cells. *Handbook of experimental pharmacology* 235, 123–152.

[111] Lénárt, P., Bacher, C. P., Daigle, N., Hand, A. R., Eils, R., Terasaki, M., and Ellenberg, J. 2005. A contractile nuclear actin network drives chromosome congression in oocytes. *Nature* 436, 7052, 812–818.

[112] Liu, J., Taylor, D. W., and Taylor, K. A. 2004. A 3-D reconstruction of smooth muscle alpha-actinin by CryoEm reveals two different conformations at the actin-binding region. *Journal of molecular biology* 338, 1, 115–125.

[113] Lodish, H. F. 2008. *Molecular cell biology*. W.H. Freeman, New York.

[114] Machnicka, B., Czogalla, A., Hryniewicz-Jankowska, A., Bogusławska, D. M., Grochowalska, R., Heger, E., and Sikorski, A. F. 2014. Spectrins: a structural platform for stabilization and activation of membrane channels, receptors and transporters. *Biochimica et biophysica acta* 1838, 2, 620–634.

[115] Marshall, W. F. 2004. Cellular length control systems. *Annual review of cell and developmental biology* 20, 677–693.

[116] Marston, S. 2018. The Molecular Mechanisms of Mutations in Actin and Myosin that Cause Inherited Myopathy. *International Journal of Molecular Sciences* 19, 7.

[117] McDonald, D., Carrero, G., Andrin, C., Vries, G. de, and Hendzel, M. J. 2006. Nucleoplasmic beta-actin exists in a dynamic equilibrium between low-mobility polymeric species and rapidly diffusing populations. *The Journal of cell biology* 172, 4, 541–552.

[118] Melak, M., Plessner, M., and Grosse, R. 2017. Correction: Actin visualization at a glance. *Journal of cell science* 130, 9, 1688.

[119] Miller, A. L. 2011. The contractile ring. *Current biology : CB* 21, 24, R976-8.

[120] Minamide, L. S., Striegl, A. M., Boyle, J. A., Meberg, P. J., and Bamburg, J. R. 2000. Neurodegenerative stimuli induce persistent ADF/cofilin-actin rods that disrupt distal neurite function. *Nature cell biology* 2, 9, 628–636.

[121] Miralles, F., Posern, G., Zaromytidou, A.-I., and Treisman, R. 2003. Actin dynamics control SRF activity by regulation of its coactivator MAL. *Cell* 113, 3, 329–342.

[122] Mori, M., Somogyi, K., Kondo, H., Monnier, N., Falk, H. J., Machado, P., Bathe, M., Nédélec, F., and Lénárt, P. 2014. An Arp2/3 nucleated F-actin shell fragments nuclear membranes at nuclear envelope breakdown in starfish oocytes. *Current biology : CB* 24, 12, 1421–1428.

[123] Morley, S. C. 2012. The actin-bundling protein L-plastin: a critical regulator of immune cell function. *International journal of cell biology* 2012, 935173.

[124] Mullins, R. D., Heuser, J. A., and Pollard, T. D. 1998. The interaction of Arp2/3 complex with actin: nucleation, high affinity pointed end capping, and formation of branching networks of filaments. *Proceedings of the National Academy of Sciences of the United States of America* 95, 11, 6181–6186.

[125] Murphy, A. C.H. and Young, P. W. 2015. The actinin family of actin cross-linking proteins – a genetic perspective. *Cell & Bioscience* 5, 1, 49.

[126] Nürnberg, A., Kitzing, T., and Grosse, R. 2011. Nucleating actin for invasion. *Nature reviews. Cancer* 11, 3, 177–187.

[127] Ochala, J., Ravenscroft, G., McNamara, E., Nowak, K. J., and Iwamoto, H. 2015. X-ray recordings reveal how a human disease-linked skeletal muscle α-actin mutation leads to contractile dysfunction. *Journal of structural biology* 192, 3, 331–335.

[128] Oda, H., Shirai, N., Ura, N., Ohsumi, K., and Iwabuchi, M. 2017. Chromatin tethering to the nuclear envelope by nuclear actin filaments: a novel role of the actin cytoskeleton in the Xenopus blastula. *Genes to cells : devoted to molecular & cellular mechanisms* 22, 4, 376–391.

[129] Okudela, K. 2014. An association between nuclear morphology and immunohistochemical expression of p53 and p16INK4A in lung cancer cells. *Medical Molecular Morphology* 47, 3, 130–136.

[130] Orlova, D. Y., Stixová, L., Kozubek, S., Gierman, H. J., Šustáčková, G., Chernyshev, A. V., Medvedev, R. N., Legartová, S., Versteeg, R., Matula, P., Stoklasa, R., and Bártová, E. 2012. Arrangement of nuclear structures is not transmitted through mitosis but is identical in sister cells. *Journal of cellular biochemistry* 113, 11, 3313–3329.

[131] Otey, C. A. and Carpen, O. 2004. Alpha-Actinin revisited: A fresh look at an old player. *Cell Motility and the Cytoskeleton* 58, 104–111.

[132] Ovesný, M., Křížek, P., Borkovec, J., Svindrych, Z., and Hagen, G. M. 2014. ThunderSTORM: a comprehensive ImageJ plug-in for PALM and STORM data analysis and super-resolution imaging. *Bioinformatics (Oxford, England)* 30, 16, 2389–2390.

[133] Parisis, N., Krasinska, L., Harker, B., Urbach, S., Rossignol, M., Camasses, A., Dewar, J., Morin, N., and Fisher, D. 2017. Initiation of DNA replication requires actin dynamics and formin activity. *The EMBO Journal* 36, 21, 3212–3231.

[134] Parisis, N. e. a. *Initiation of DNA replication requires actin dynamics and formin activity*.

[135] Pierce, B. A. 2017. *Genetics*. *A conceptual approach*. Macmillan Education, New York, NY.

[136] Plessner, M. and Grosse, R. 2015. Extracellular signaling cues for nuclear actin polymerization. *European journal of cell biology* 94, 7-9, 359–362.

[137] Plessner, M. and Grosse, R. 2019. Dynamizing nuclear actin filaments. *Current opinion in cell biology* 56, 1–6.

[138] Plessner, M., Knerr, J., and Grosse, R. 2019. Centrosomal Actin Assembly Is Required for Proper Mitotic Spindle Formation and Chromosome Congression. *iScience* 15, 274–281.

[139] Plessner, M., Melak, M., Chinchilla, P., Baarlink, C., and Grosse, R. 2015. Nuclear F-actin formation and reorganization upon cell spreading. *The Journal of biological chemistry* 290, 18, 11209–11216.

[140] Pollard, T. D. 1986. Rate constants for the reactions of ATP- and ADP-actin with the ends of actin filaments. *J Cell Biol* 103, 6 Pt 2, 2747–2754.

[141] Pollard, T. D. and Cooper, J. A. 2009. Actin, a central player in cell shape and movement. *Science (New York, N.Y.)* 326, 5957, 1208–1212.

[142] Pozarowski, P. and Darzynkiewicz, Z. 2004. Analysis of cell cycle by flow cytometry. *Methods in molecular biology (Clifton, N.J.)* 281, 301–311.

[143] Pruyne, D., Evangelista, M., Yang, C., Bi, E., Zigmond, S., Bretscher, A., and Boone, C. 2002. Role of formins in actin assembly: nucleation and barbed-end association. *Science (New York, N.Y.)* 297, 5581, 612–615.

[144] Rajoria, S., Zhao, L., Intes, X., and Barroso, M. 2014. FLIM-FRET for Cancer Applications. *Current molecular imaging* 3, 2, 144–161.

[145] Rao, X., Huang, X., Zhou, Z., and Lin, X. 2013. An improvement of the 2ˆ(–delta delta CT) method for quantitative real-time polymerase chain reaction data analysis. *Biostatistics, bioinformatics and biomathematics* 3, 3, 71–85.

[146] Roberts, T. M. and Stewart, M. 1997. Nematode sperm: amoeboid movement without actin. *Trends in cell biology* 7, 9, 368–373.

[147] Robinson, D. N., Ocon, S. S., Rock, R. S., and Spudich, J. A. 2002. Dynacortin is a novel actin bundling protein that localizes to dynamic actin structures. *J. Biol. Chem.* 277, 11, 9088–9095.

[148] Rocchetti, A., Hawes, C., and Kriechbaumer, V. 2014. Fluorescent labelling of the actin cytoskeleton in plants using a cameloid antibody. *Plant Methods* 10, 12.

[149] Rottner, K., Faix, J., Bogdan, S., Linder, S., and Kerkhoff, E. 2017. Actin assembly mechanisms at a glance. *Journal of cell science* 130, 20, 3427–3435.

[150] Rottner, K. and Kage, F. 2017. Actin Networks: Adapting to Load through Geometry. *Current biology : CB* 27, 23, R1274-R1277.

[151] Rottner, K. and Stradal, T. E. B. 2016. How distinct Arp2/3 complex variants regulate actin filament assembly. *Nature cell biology* 18, 1, 1–3.

[152] Sahai, E. 2005. Mechanisms of cancer cell invasion. *Current opinion in genetics & development* 15, 1, 87–96.

[153] Santos-Rosa, H. and Caldas, C. 2005. Chromatin modifier enzymes, the histone code and cancer. *European journal of cancer (Oxford, England : 1990)* 41, 16, 2381–2402.

[154] Schafer, K. A. 1998. The cell cycle: a review. *Veterinary pathology* 35, 6, 461–478.

[155] Scheer, U., Hinssen, H., Franke, W. W., and Jockusch, B. M. 1984. Microinjection of actin-binding proteins and actin antibodies demonstrates involvement of nuclear actin in transcription of lampbrush chromosomes. *Cell* 39, 1, 111–122.

[156] Schindelin, J., Arganda-Carreras, I., Frise, E., Kaynig, V., Longair, M., Pietzsch, T., Preibisch, S., Rueden, C., Saalfeld, S., Schmid, B., Tinevez, J.-Y., White, D. J., Hartenstein, V., Eliceiri, K., Tomancak, P., and Cardona, A. 2012. Fiji - an Open Source platform for biological image analysis. *Nature methods* 9, 7.

[157] Schooley, A., Vollmer, B., and Antonin, W. 2012. Building a nuclear envelope at the end of mitosis: coordinating membrane reorganization, nuclear pore complex assembly, and chromatin de-condensation. *Chromosoma* 121, 6, 539–554.

[158] Schrank, B. R., Aparicio, T., Li, Y., Chang, W., Chait, B. T., Gundersen, G. G., Gottesman, M. E., and Gautier, J. 2018. Nuclear ARP2/3 drives DNA break clustering for homology-directed repair. *Nature* 559, 7712, 61–66.

[159] Schubert, H. L., Wittmeyer, J., Kasten, M. M., Hinata, K., Rawling, D. C., Héroux, A., Cairns, B. R., and Hill, C. P. 2013. Structure of an actin-related subcomplex of the SWI/SNF chromatin remodeler. *Proceedings of the National Academy of Sciences of the United States of America* 110, 9, 3345–3350.

[160] Serebryannyy, L. A., Cruz, C. M., and Lanerolle, P. de. 2016. A Role for Nuclear Actin in HDAC 1 and 2 Regulation. *Scientific reports* 6, 28460.

[161] Shao, X., li, Q., Mogilner, A., Bershadsky, A., and Shivashankar, G. V. 2015. Mechanical stimulation induces formin-dependent assembly of a perinuclear actin rim. *Proceedings of the National Academy of Sciences* 112, 201504837.

[162] Shinomiya, H. 2012. Plastin family of actin-bundling proteins: its functions in leukocytes, neurons, intestines, and cancer. *International journal of cell biology* 2012, 213492.

[163] Short, B. 2013. Formin' the cytokinetic ring. *J Cell Biol* 203, 1, 3.

[164] Sjöblom, B., Salmazo, A., and Djinović-Carugo, K. 2008. Alpha-actinin structure and regulation. *Cellular and molecular life sciences : CMLS* 65, 17, 2688–2701.

[165] Stark, G. R. and Taylor, W. R. 2004. Analyzing the G2/M checkpoint. *Methods in molecular biology (Clifton, N.J.)* 280, 51–82.

[166] Stevenson, R. P., Veltman, D., and Machesky, L. M. 2012. Actin-bundling proteins in cancer progression at a glance. *Journal of cell science* 125, Pt 5, 1073–1079.

[167] Straub, F. B. and Feuer, G. 1989. Adenosinetriphosphate. The functional group of actin. 1950. *Biochimica et biophysica acta* 1000, 180–195.

[168] Strzelecka, M. and Heald, R. 2014. RUVs drive chromosome decondensation after mitosis. *Developmental cell* 31, 3, 259–260.

[169] Stüven, T., Hartmann, E., and Görlich, D. 2003. Exportin 6: a novel nuclear export receptor that is specific for profilin.actin complexes. *The EMBO Journal* 22, 21, 5928–5940.

[170] Takemoto, A., Kawashima, S. A., Li, J.-J., Jeffery, L., Yamatsugu, K., Elemento, O., and Nurse, P. 2016. Nuclear envelope expansion is crucial for proper chromosomal segregation during a closed mitosis. *Journal of cell science* 129, 6, 1250–1259.

[171] Tamaru, H. 2010. Confining euchromatin/heterochromatin territory: jumonji crosses the line. *Genes & development* 24, 14, 1465–1478.

[172] Taylor, K. A., Taylor, D. W., and Schachat, F. 2000. Isoforms of alpha-actinin from cardiac, smooth, and skeletal muscle form polar arrays of actin filaments. *J Cell Biol* 149, 3, 635–646.

[173] Terry, S. J., Donà, F., Osenberg, P., Carlton, J. G., and Eggert, U. S. 2018. Capping protein regulates actin dynamics during cytokinetic midbody maturation. *Proceedings of the National Academy of Sciences of the United States of America* 115, 9, 2138–2143.

[174] Titus, M. A. 2018. Myosin-Driven Intracellular Transport. *Cold Spring Harbor perspectives in biology* 10, 3.

[175] Tojkander, S., Gateva, G., and Lappalainen, P. 2012. Actin stress fibers--assembly, dynamics and biological roles. *Journal of cell science* 125, Pt 8, 1855–1864.

[176] Tokunaga, M., Imamoto, N., and Sakata-Sogawa, K. 2008. Highly inclined thin illumination enables clear single-molecule imaging in cells. *Nature methods* 5, 2, 159–161.

[177] Turkowyd, B., Virant, D., and Endesfelder, U. 2016. From single molecules to life: microscopy at the nanoscale. *Analytical and bioanalytical chemistry* 408, 25, 6885–6911.

[178] van de Linde, S., Löschberger, A., Klein, T., Heidbreder, M., Wolter, S., Heilemann, M., and Sauer, M. 2011. Direct stochastic optical reconstruction microscopy with standard fluorescent probes. *Nature protocols* 6, 7, 991–1009.

[179] Vartiainen, M. K., Guettler, S., Larijani, B., and Treisman, R. 2007. Nuclear actin regulates dynamic subcellular localization and activity of the SRF cofactor MAL. *Science (New York, N.Y.)* 316, 5832, 1749–1752.

[180] Vassilev, L. T. 2006. Cell cycle synchronization at the G2/M phase border by reversible inhibition of CDK1. *Cell cycle (Georgetown, Tex.)* 5, 22, 2555–2556.

[181] Vassilev, L. T., Tovar, C., Chen, S., Knezevic, D., Zhao, X., Sun, H., Heimbrook, D. C., and Chen, L. 2006. Selective small-molecule inhibitor reveals critical mitotic functions of human CDK1. *Proceedings of the National Academy of Sciences of the United States of America* 103, 28, 10660–10665.

[182] Vilmos, P., Kristó, I., Szikora, S., Jankovics, F., Lukácsovich, T., Kari, B., and Erdélyi, M. 2016. The actin-binding ERM protein Moesin directly regulates spindle assembly and function during mitosis. *Cell biology international* 40, 6, 696–707.

[183] Virant, D., Traenkle, B., Maier, J., Kaiser, P. D., Bodenhöfer, M., Schmees, C., Vojnovic, I., Pisak-Lukáts, B., Endesfelder, U., and Rothbauer, U. 2018. A peptide tag-specific nanobody enables high-quality labeling for dSTORM imaging. *Nature communications* 9, 1, 930.

[184] Virtanen, J. A. and Vartiainen, M. K. 2017. Diverse functions for different forms of nuclear actin. *Current opinion in cell biology* 46, 33–38.

[185] Viswanathan, M. C., Schmidt, W., Rynkiewicz, M. J., Agarwal, K., Gao, J., Katz, J., Lehman, W., and Cammarato, A. 2017. Distortion of the Actin A-Triad Results in Contractile Disinhibition and Cardiomyopathy. *Cell reports* 20, 11, 2612–2625.

[186] Vizcarra, C. L., Kreutz, B., Rodal, A. A., Toms, A. V., Lu, J., Zheng, W., Quinlan, M. E., and Eck, M. J. 2011. Structure and function of the interacting domains of Spire and Fmn-family formins. *Proceedings of the National Academy of Sciences of the United States of America* 108, 29, 11884–11889.

[187] Wang, Y., Sherrard, A., Zhao, B., Melak, M., Trautwein, J., Kleinschnitz, E.-M., Tsopoulidis, N., Fackler, O. T., Schwan, C., and Grosse, R. 2019. GPCR-induced calcium transients trigger nuclear actin assembly for chromatin dynamics. *Nature communications* 10, 1, 5271.

[188] Watanabe, S., Ando, Y., Yasuda, S., Hosoya, H., Watanabe, N., Ishizaki, T., and Narumiya, S. 2008. mDia2 Induces the Actin Scaffold for the Contractile Ring and Stabilizes Its Position during Cytokinesis in NIH 3T3 Cells. *Molecular biology of the cell* 19, 5, 2328–2338.

[189] Weber, A., Pennise, Cynthia R., Babcock, G. G., and Fowler, V. M. 1994. Tropomodulin caps the pointed ends of actin filaments. *J Cell Biol* 127, 1627–1635.

[190] Webster, M., Witkin, K. L., and Cohen-Fix, O. 2009. Sizing up the nucleus: nuclear shape, size and nuclear-envelope assembly. *Journal of cell science* 122, Pt 10, 1477–1486.

[191] Weed, S. A., Karginov, A. V., Schafer, D. A., Weaver, A. M., Kinley, A. W., Cooper, J. A., and Parsons, J. T. 2000. Cortactin localization to sites of actin assembly in lamellipodia requires interactions with F-actin and the Arp2/3 complex. *J Cell Biol* 151, 1, 29–40.

[192] Weins, A., Kenlan, P., Herbert, S., Le, T. C., Villegas, I., Kaplan, B. S., Appel, G. B., and Pollak, M. R. 2005. Mutational and Biological Analysis of alpha-actinin-4 in focal segmental glomerulosclerosis. *Journal of the American Society of Nephrology : JASN* 16, 12, 3694–3701.

[193] Wilkins, B. J., Rall, N. A., Ostwal, Y., Kruitwagen, T., Hiragami-Hamada, K., Winkler, M., Barral, Y., Fischle, W., and Neumann, H. 2014. A cascade of histone modifications induces chromatin condensation in mitosis. *Science (New York, N.Y.)* 343, 6166, 77–80.

[194] Yamada, S., Yanamoto, S., Yoshida, H., Yoshitomi, I., Kawasaki, G., Mizuno, A., and Nemoto, T. K. 2010. RNAi-mediated down-regulation of alpha-actinin-4 decreases invasion potential in oral squamous cell carcinoma. *International journal of oral and maxillofacial surgery* 39, 1, 61–67.

[195] Yang, X. and Lin, Y. 2018. Functions of nuclear actin-binding proteins in human cancer. *Oncology letters* 15, 3, 2743–2748.

[196] Young, K. G. and Kothary, R. 2005. Spectrin repeat proteins in the nucleus. *BioEssays : news and reviews in molecular, cellular and developmental biology* 27, 2, 144–152.

[197] Zhang, Y. Y., Tabataba, H., Liu, X. Y., Wang, J. Y., Yan, X. G., Farrelly, M., Jiang, C. C., Guo, S. T., Liu, T., Kao, H.-Y., Thorne, R. F., Zhang, X. D., and Jin, L. 2018. ACTN4 regulates the stability of RIPK1 in melanoma. *Oncogene* 37, 29, 4033–4045.

[198] Zhao, X., Khurana, S., Charkraborty, S., Tian, Y., Sedor, J. R., Bruggman, L. A., and Kao, H.-Y. 2017. α Actinin 4 (ACTN4) Regulates Glucocorticoid Receptor-mediated Transactivation and Transrepression in Podocytes. *The Journal of biological chemistry* 292, 5, 1637–1647.

[199] Zlatanova, J., Leuba, S. H., and van Holde, K. 1998. Chromatin fiber structure: morphology, molecular determinants, structural transitions. *Proceedings of the National Academy of Sciences* 74, 5, 2554–2566.

[200] Zuchero, J. B., Coutts, A. S., Quinlan, M. E., La Thangue, N. B., and Mullins, R. D. 2009. p53-cofactor JMY is a Multifunctional Actin Nucleation Factor. *Nature cell biology* 11, 4, 451–459.

Appendix

Collection of dSTORM images

List of academic teachers

Collection of dSTORM images

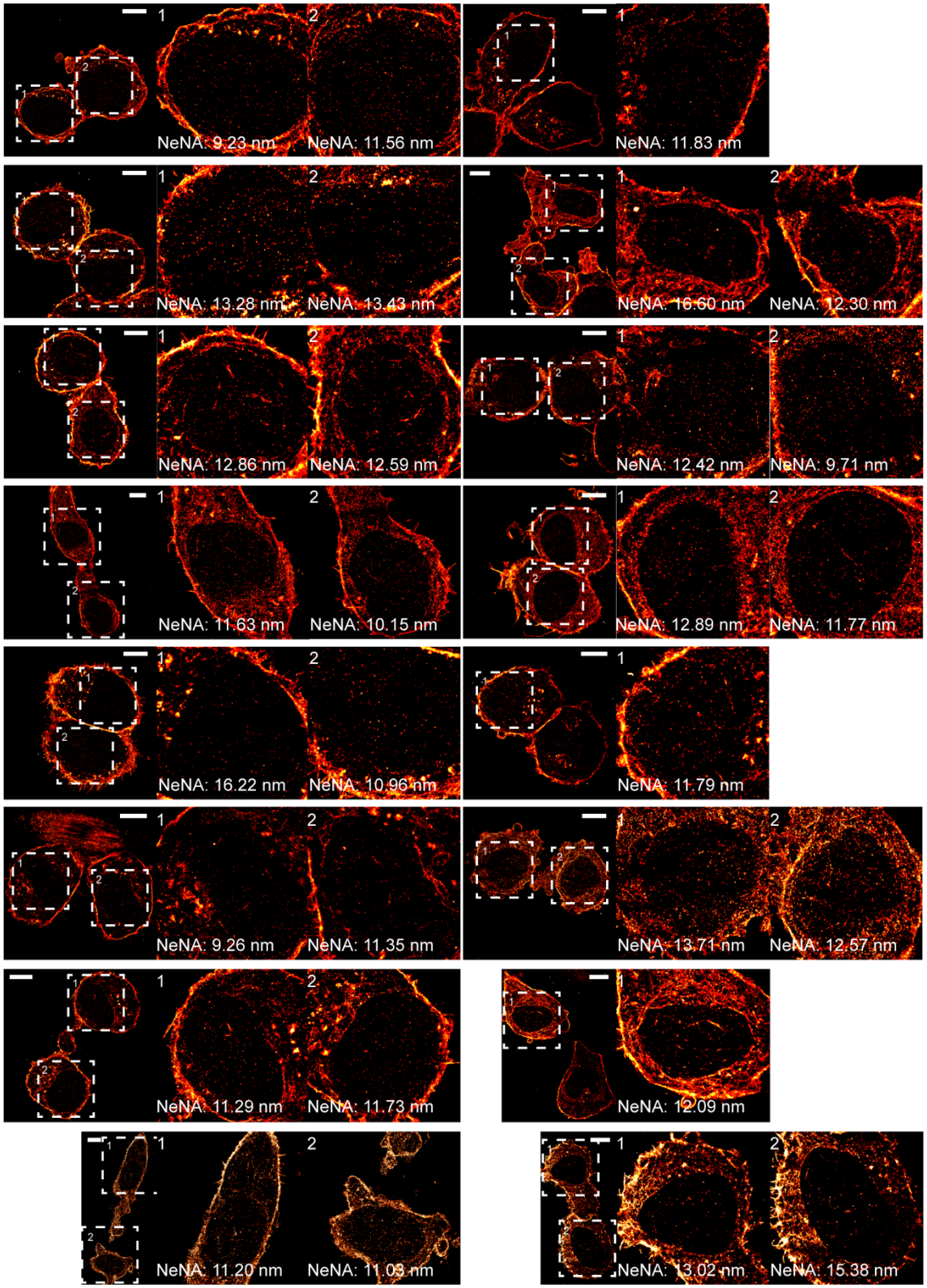

Image collection: ACTN4 wt.

NIH3T3 cells expressing ACTN4 wt SNAP were stained with phalloidin-AF647 after fixation (exact procedure cf 3.4.3 and 3.4.4). Collection contains only images that were drift corrected based on IR beads. Panels with scale bars show postmitotic cells; panels to their right represent zoom images of the indicated nuclei (white boxes); cells and nuclei with irregular illumination were excluded from analysis; scale bars 5 µm.

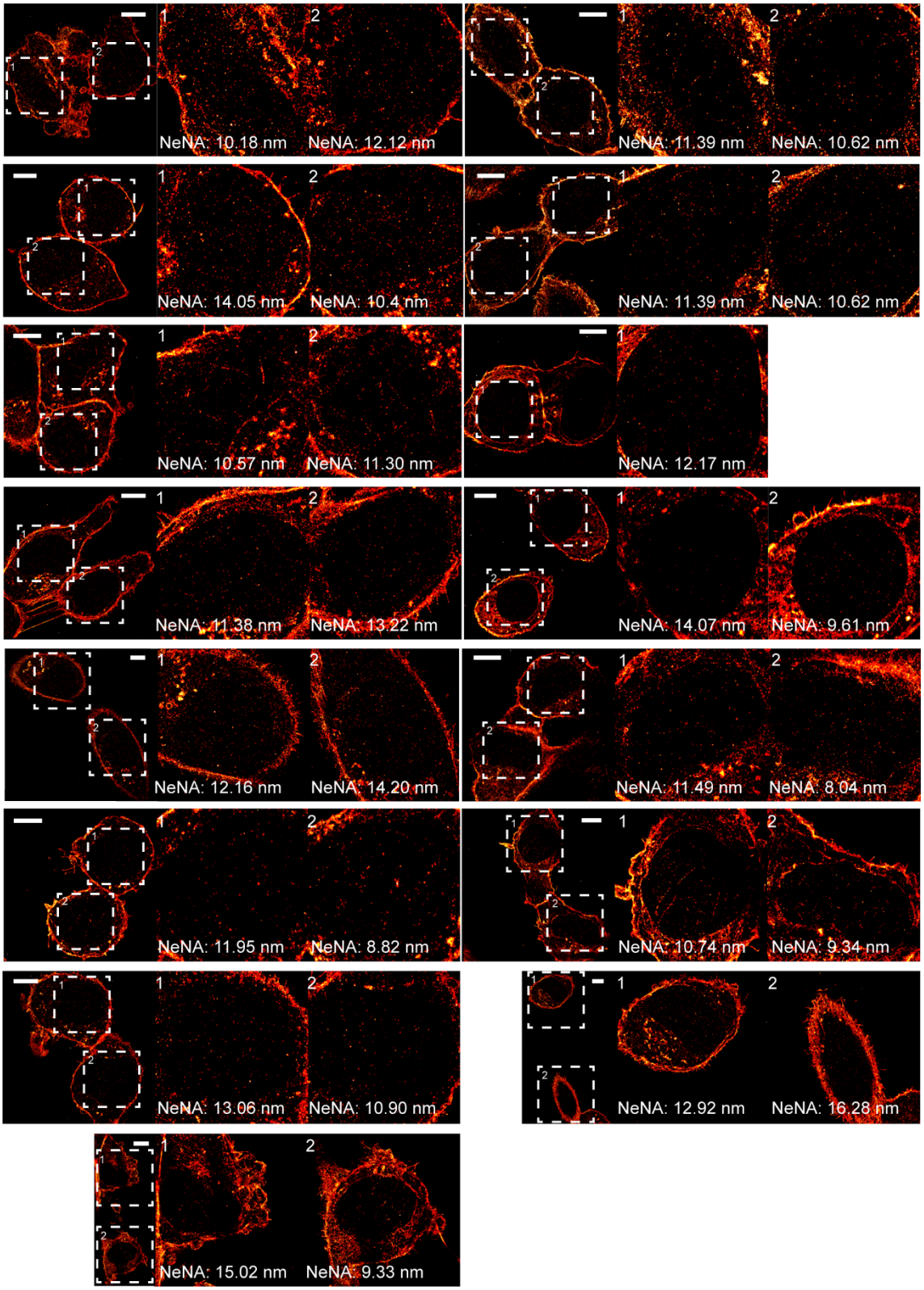

Image collection: dn ACTN4 NLS.
NIH3T3 cells expressing dn ACTN4 NLS SNAP were stained with phalloidin-AF647 after fixation (exact procedure cf 3.4.3 and 3.4.4). Collection contains only images that were drift corrected based on IR beads. Panels with scale bars show postmitotic cells; panels to their right represent zoom images of the indicated nuclei (white boxes); cells and nuclei with irregular illumination were excluded from analysis; scale bars 5 µm.

List of academic teachers

At the Philipps-University Marburg, I was taught by following academic teachers:

PD Dr. Anagnostou
Prof. Dr. Bakowsky
Prof. Dr. Bünemann
Prof. Dr. Culmsee
Prof. Dr. Diederich
Dr. Feuser
Dr. Freidank
Prof. Dr. Friedrich
Prof. Dr. Grünweller
Prof. Dr. Hartmann
PD Dr. Hohmann
Prof. Dr. Keusgen
Prof. Dr. Klebe
Prof. Dr. Kockskämper
Prof. Dr. Kolb
Prof. Dr. Krasel
Dr. Kreusch
Prof. Dr. Li
Prof. Dr. Petersen
Prof. Dr. Radziwill
Prof. Dr. Reuther
Dr. Schäfer
Prof. Dr. Schlitzer
Prof. Dr. Schneider
Prof. Dr. Steinmetzer
Prof. Dr. Strauer
Dr. Streubel